Effect of multi-frequency parametric excitations on the dynamics of on-board rotor-bearing systems

Yvon Briend, Mzaki Dakel, E. Chatelet, Marie-Ange Andrianoely, Régis Dufour, Sophie Baudin

Version of Record: https://www.sciencedirect.com/science/article/pii/S0094114X19316295
Manuscript_ba7b23e8e146f2c0ec5bfe24d12a53d3

Effect of multi-frequency parametric excitations on the dynamics of on-board rotor-bearing systems

Yvon Briend [a], Mzaki Dakel [a,*], Eric Chatelet [a], Marie-Ange Andrianoely [a], Régis Dufour [a], Sophie Baudin [b]

[a] Univ Lyon, INSA-Lyon, CNRS UMR5259, LaMCoS, F-69621, France

[b] AVNIR Engineering, 62 Boulevard Niels Bohr, 69603 Villeurbanne Cedex, France

Abstract

In the transportation domain such as automotive turbochargers and aircraft turbines, the vibrations of on-board rotors are induced not only by the mass unbalance excitation but also by various movements of their support. The dynamics of an on-board rotor mounted on hydrodynamic finite-length bearings is investigated in the presence of support motions which create multi-frequency parametric excitations. The developed on-board rotor model is based on the gyroscopic Timoshenko beam finite element with two nodes and six degrees of freedom per node for 3D motions (transverse and axial displacements as well as rotations due to the bending and to the torsion). The equations of motion highlight time-varying parametric terms due to the mass unbalance, the support rotations, the coupling between both phenomena and the combination of mass unbalance and support translations. These parametric terms can yield a dynamic instability because they contribute as generators of internal excitation. In the presented applications, single-frequency and multi-frequency parametric excitations are used. Namely, the rotor is excited either by simple and combined sinusoidal support rotations or by a rotating mass unbalance combined with sinusoidal support translations to examine the stability of the static equilibrium point through the Floquet theory.

Keywords: Rotordynamics, on-board rotor, finite element method, hydrodynamic journal bearing, support motions, parametric excitation, dynamic instability.

1. Introduction

In numerous modern industrial applications, the rotating machines possess a major role. Indeed, most of them can be considered as on-board machines subject to both mass unbalance and several excitations of the support. The following examples are considered as on-board rotating machines (rotors with a mobile support): a naval ship turbine subject to the roll or pitch motions due to the sea waves, an automotive turbocharger excited by the road imperfections, an aircraft turbine engine excited by the wing vibration, etc. The undesirable and unavoidable mass unbalance is created due to the eccentricity of the mass center all along the rotor axis. It is conventionally caused by the geometry of the rotating parts (manufacturing defaults), the material non-homogeneities, the assembly of the rotating parts and the service conditions. The aim of the rotor balancing is to minimize the mass unbalance but the balancing generally is not able to implement a whole elimination (for example, see Kang et al. [1] and Levecque et al. [2]). The support movements can increase the vibrations of the rotor and lead to phenomena of dynamic instability. Therefore the prediction of dynamic behavior of the rotors must be carried out more and more carefully at the design stage which has to take into account multi-source excitations in order to fabricate rotating machines as reliable as possible and to avert a disastrous failure during the operation phase.

Rotordynamics has been extensively treated in the case of a fixed support. In this context, the literature involves several books studying a large assortment of phenomena linked with the dynamic behavior of symmetric/asymmetric rigid/elastic rotor systems supported by rigid bearings or linear/nonlinear flexible ones. Only few of them can be cited in the current paper (see Lalanne and Ferraris [3], Genta [4]). Numerous studies contributed to the finite element

* Corresponding author. fax: +33 4 72 43 89 30.
E-mail addresses: yvon.briend@insa-lyon.fr (Y. Briend), mzaki.dakel@gmail.com (M. Dakel).

method and applied it to the rotor modeling. Nelson and McVaugh [5] developed the major breakthrough in the finite element modeling of a rotor and concentrated on a model called "Rayleigh beam", which takes into consideration the gyroscopic effects depending on the speed of rotation of the rotor and the rotatory inertia of the shaft. Some works were interested by the instability of parametrically excited systems. Dufour and Berlioz [6] established the time-varying parametric equations of motion of the system and evaluated the stability of pinned-pinned, clamped-pinned and clamped-clamped beams excited by periodic axial forces and torques by employing the Rayleigh-Ritz formulation, the Floquet theory and the Friedmann approach [7]. As shown in their paper, the dynamic behavior instability could occur if the excitation frequency was close to a combination of two natural frequencies of the system, already formulated by Hsu [8].

Owing to the diverse exploitations of rotors in the daily industries since the past century, on-board rotordynamics was an attractive scientific subject for a lot of authors and researchers in the last decade. The article of Lin and Meng [9] is considered as one of the first studies concerning the on-board rotor systems in aircrafts. In their work, they predicted the influence of the translational motions with a constant speed as well as a constant acceleration and of the sinusoidal translation of the support on the time history responses of a Jeffcott rotor in the presence of a mass unbalance excitation. Lee et al. [10] proposed a finite element rotor model based on the Timoshenko beam theory and subject to a shock excitation of the support and discussed the experimental behavior of a rotor under this excitation. Duchemin et al. [11] investigated analytically the motion stability of a rotor excited by a periodic rotational motion of the rigid support using the Rayleigh-Ritz and multiple scales methods. In order to validate the theoretical results, they provided also experimental tests. Depending on the model presented in [11], the work of Driot et al. [12] highlighted numerical orbits of the rotor and compared them with an experimental study. El-Saeidy and Sticher [13] derived the equations of vibratory motion of a rigid rotor-linear/nonlinear bearing system in the presence of a mass unbalance and harmonic movements of the support around or along transverse directions. They calculated analytical frequency responses of the rotor mounted on linear bearings, while they interpreted numerical results regarding the time domain, the fast Fourier transform and the Poincaré map in the presence of a bearing cubic nonlinearity. Using an electromagnetic actuator, Das et al. [14,15] proposed an active vibration control strategy for a flexible rotor-bearing system modeled with Rayleigh beam finite elements and subject to a mass unbalance as well as to a sinusoidal rotation of the support.

In this decade, the utilization of advanced computer softwares and more robust techniques opened effectively the possibility for more accurate developments to be applied to on-board rotor systems and numerous studies contributed to this topic. Dakel et al. examined the influence of the rotational and translational motions of the support on the lateral dynamic behavior of a finite element rotor model based on the Timoshenko beam theory and mounted either on rigid ones [16] or on linearized/nonlinear hydrodynamic journal ones [17]. In addition, these authors observed instability regions due to parametric excitations associated with the geometric asymmetry of the rotor [16] and with the support rotations [17]. On the other hand, they obtained sub-harmonic, quasi-periodic and chaotic responses of the on-board rotor because of the hydrodynamic bearing nonlinearity [17]. Recently, Han and Chu published some papers on the support-excited rotor systems. First, the authors studied a finite element cracked rotor model founded on the Euler beam theory and excited by sinusoidal rotations of the support and introduced an improved harmonic balance method to obtain the linear stabilized responses and to discuss the influence of the amplitude and the frequency of the support excitations as well as that of the crack depth [18]. In the second paper [19], they predicted the dynamics of spur gear-rotor systems subject to sinusoidal rotations of the support around one of the transverse directions and showed that the corresponding response amplitudes were slightly affected even if the excitation frequencies and their multiples were found in the responses. Later, Han and Chu [20] applied the discrete state transition matrix method (Floquet theory) for an on-board rotor system modeled in the same way as in [18] to attain the parametric instability regions induced by the periodic rotations of the support. Sousa et al. introduced a finite element rotor model depending on the theoretical approach proposed by Duchemin et al. [11] to discuss some numerical results regarding rotational and translational excitations of the support [21] and to emphasize an experimental validation of this model regarding the impact and sinusoidal translations of the support [22].

Very recently, some works were interested by the nonlinear dynamics of on-board rotors mounted on hydrodynamic journal bearings after the appearance of the study of Dakel et al. [17]. In the case of sinusoidal translations of the support, time history responses, spectral analysis, Poincaré maps and bifurcation diagrams were the analysis tools to observe nonlinear phenomena (such as quasi-periodic and chaotic motions) for a centrifugal pump [23], a turbocharger rotor system [24], a rigid rotor [25], a flexible rotor modeled by Euler beam finite elements [26]. On the other hand, researchers concentrated on the dynamic behavior of the on-board rotor in the presence of nonlinearities which were caused by the support rotations [27] or by the highly flexible shaft [28]. On-board rotordynamics under support excitations was exploited by some works to investigate the vibrations of rotors with fibre reinforced blades (composite material) [29], to study the transient regime in the presence of a non-stationary speed of rotation [30], to deal with the geometric asymmetry of disk and shaft [31] and to examine a new control law using active magnetic bearings [32].

Although most of the researches stated previously deal with support-harmonically excited rotor systems, few articles focus on the stability analysis of the parametrically excited on-board rotors especially in the case of multi-frequency parametric excitations. Moreover, these researches focus either on constructing simplified models or on

predicting only the dynamics of on-board rotors in bending. Even if the adoption of simplified models facilitates the investigation and the understanding of the dynamic behavior of such mechanical systems, it remains restricted in the practical applications and weakens the ability to produce the desirable accuracy between the theoretical and realistic rotor models under the operating conditions. Indeed, the most common restrictions and simplifications are relevant either to the geometric characteristics of the rotor (for example, rigid rotor [13,25]), to the use of the Rayleigh-Ritz approach (for example, see [11,12]) as well as the finite element method based on four flexural degrees of freedom (for example, see [16–18,20,21,26]) for the spatial discretization of the rotor model, to the constant damping and stiffness coefficients of flexible bearings supporting the rotor (for example, see [13,15]) or to the type of rotor support excitation (single translation or rotation).

In order to enhance the ability of an on-board rotor model, an original contribution is proposed in the current paper. Namely, a flexible rotor running at a time-varying speed of rotation is discretized using the finite element method based on the Timoshenko beam theory as well as on six degrees of freedom per node (flexural, axial and torsional ones), mounted on hydrodynamic finite-length bearings (for which the external forces are computed using the Reynolds equation [33]), and excited by combined deterministic movements (three rotations and three translations) of the rigid support. Eulerian angles are utilized to describe the orientation of the disk and the shaft with respect to the moving support in the case of bending and torsion of the flexible rotor. The kinetic and strain energies as well as the virtual work of the rotating rotor components are calculated. Timoshenko beam finite elements containing the effects of the rotatory inertia, the gyroscopic inertia and the shear deformation of shaft due to the bending are considered for the dynamic modeling of the on-board rotor. Using the finite difference method to treat the Reynolds equation, a linearized model with damping and stiffness coefficients is considered for the hydrodynamic journal bearings. The linear second-order differential equations of vibratory motion of the rotor with respect to the rigid support (which constitutes a non-inertial frame of reference) are established by applying Lagrange's equations. They include time-varying parametric coefficients corresponding to the mass unbalance inclination, to the support rotations, to the coupling between both phenomena and to the combination of mass unbalance and support translations. These time-varying coefficients are a source of dynamic instability because they create single-frequency and multi-frequency parametric excitations during sinusoidal movements of the support. In the proposed numerical examples, a symmetric rotor-hydrodynamic journal bearing system is subject either to simple and combined sinusoidal rotations of the support or to rotating mass unbalance correlated with sinusoidal translations of the support. Its dynamic behavior is investigated by discussing mainly the influence of the support motions on the stability charts.

2. Problem formulation and assumptions adopted for the on-board rotor

The basic mechanical components of the on-board rotor are sketched in Fig. 1. The distribution of the mass unbalance is continuous and arbitrary all along the rotor. Therefore the mass unbalance cannot perfectly be eliminated. The residual mass unbalance and the different imposed motions of the support represent the excitations taken into account. The transverse deflections, the axial displacement and the torsional rotation of the shaft are studied and evaluated here to understand the dynamic behavior of the rotor.

The following assumptions are retained in the current investigation: the symmetric disk is infinitely rigid, the symmetric shaft is deformable and modeled with elastic isotropic homogeneous Timoshenko beam elements of constant cross-section, the mass unbalance is modeled as lumped masses, the hydrodynamic journal bearings supporting the shaft are of finite-length type, the support is absolutely rigid and mobile, the rotor runs at a time-varying speed of rotation $\dot{\phi}(t)$. The latter brings additional stiffness matrices in the equations of motion compared to those obtained

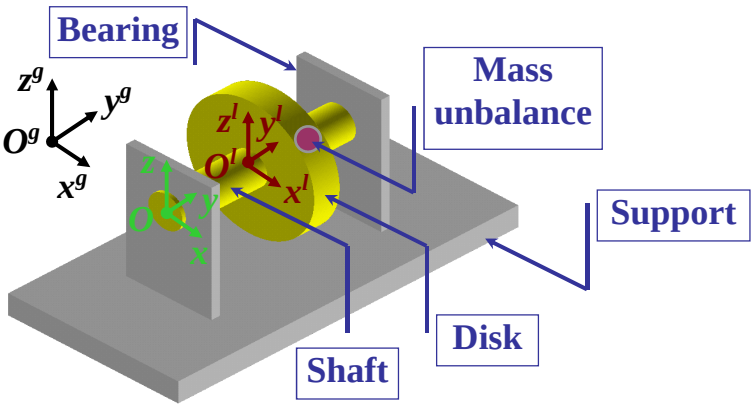

Fig. 1. Basic mechanical components and coordinate systems of the on-board rotor model.

with a constant speed of rotation.

Taking into account the support movement modifies the equations of motion of a rotor when compared to those produced in the case of a fixed support. The approach proposed by Duchemin et al. [11] is adopted in order to ensure a straightforward modeling. Three coordinate systems are employed to consider the motion of the support with respect to the ground and that of the rotor with respect to the support.

The derivation of the equations of motion is inspired from the theory described by Lalanne and Ferraris [3] as well as Dakel et al. [16]. First of all, the frames of reference necessary to characterize the movement of an on-board rotor are defined and the vectors expressing the rotations between them are computed. Then, the kinetic energies for the disk, the shaft element and the concentrated mass unbalance, the strain energy for the shaft element and the virtual works for the gravity loads due to the disk and to the shaft as well as the hydrodynamic bearing forces are calculated. Moreover, the rotating flexible rotor is discretized by means of the Timoshenko beam finite elements for which each node is built with six degrees of freedom (transverse and axial translations as well as rotations due to the bending and to the torsion). Finally, the differential equations of motion of an on-board rotor-hydrodynamic bearing system are deduced from Lagrange's equations applied with respect to the generalized coordinates q_i by the following form:

$$\frac{\mathrm{d}}{\mathrm{d}t}\left(\frac{\partial T}{\partial \dot{q}_i}\right) - \frac{\partial T}{\partial q_i} + \frac{\partial U}{\partial q_i} = F_{q_i}, \tag{1}$$

with n_{dof} $(1 \leq i \leq n_{dof})$ the number of degrees of freedom, T and U the kinetic and strain energies respectively and F_{q_i} the external forces corresponding to q_i. The symbol "$\bullet$" refers to the differentiation with respect to time t.

3. Basic calculations of the kinematics

The utilization of more than one frame of reference requires establishing carefully the relationships between the different defined coordinate systems. Fig. 1 shows three principal Cartesian frames of reference introduced to take into account the mobility of the rotor support: $R^g\,(x^g, y^g, z^g)$ is the Galilean frame of reference fixed to the ground, $R\,(x, y, z)$ is the non-inertial frame of reference connected to the moving rigid support, $R^l\,(x^l, y^l, z^l)$ is the non-inertial local frame of reference (moving with the rotor during its operation) attached to the center of mass of the rigid disk or to the geometric center of a section of the deformable shaft. Let O^g, O and O^l be the origins of the frames of reference R^g, R and R^l respectively. The origin O^g of the frame R^g represents the center of rotation of the support R with respect to the ground.

The elastic line of the undeformed shaft is along the Oy axis on which the disk mass center is located. Moreover, xOy and yOz are both planes of symmetry for the disk and the undeformed shaft. Thus Ox, Oy and Oz are principal axes of inertia.

Let us consider an arbitrary point C^{init} along the elastic line, i.e., it represents the geometric center of the undeformed shaft. Its coordinates in the frame R are $(0, y, 0)$. Let its time-dependent dynamic lateral displacements along the Ox and Oz axes be $u\,(y,t)$ and $w\,(y,t)$, see Fig. 2(a). On the other hand, its coordinate along the Oy longitudinal axis is not a constant with respect to the rotor support R. Thus the axial displacement $v\,(y,t)$ along Oy is taken into account.

According to the classical rotordynamics theory, the transformation between the frames R and R^l presented in Fig. 2(a) and (b) is carried out by the Euler angles $\psi\,(y,t)$, $\theta\,(y,t)$, $\varphi\,(y,t) = \phi\,(t) + \lambda\,(y,t)$ (where ψ, θ, φ, λ are respectively the precession, nutation, spinning as well as torsional angles, while ϕ is the nominal rotation of the shaft without deformation) and two intermediate frames of reference $R^{i_1}\left(x^{i_1}, y^{i_1}, z^{i_1}\right)$ and $R^{i_2}\left(x^{i_2}, y^{i_2}, z^{i_2}\right)$. The relationship between the components of any vector $\mathbf{V}$ projected in R and those projected in R^l is expressed as follows [16]:

$$\mathbf{V}|_{R^l} = \mathbf{R}^R_{R^l}\mathbf{V}|_R \quad \text{with} \quad \mathbf{R}^R_{R^l} = \begin{bmatrix} \cos\psi\cos\varphi - \sin\psi\sin\theta\sin\varphi & \sin\psi\cos\varphi + \cos\psi\sin\theta\sin\varphi & -\cos\theta\sin\varphi \\ -\sin\psi\cos\theta & \cos\psi\cos\theta & \sin\theta \\ \cos\psi\sin\varphi + \sin\psi\sin\theta\cos\varphi & \sin\psi\sin\varphi - \cos\psi\sin\theta\cos\varphi & \cos\theta\cos\varphi \end{bmatrix}, \tag{2}$$

where $\mathbf{R}^R_{R^l}$ is the rotation matrix of the rotor R^l with respect to its support R.

Introducing the intermediate reference frames $R^{i_3}\left(x^{i_3}, y^{i_3}, z^{i_3}\right)$ and $R^{i_4}\left(x^{i_4}, y^{i_4}, z^{i_4}\right)$ as well as the Euler angles $\alpha\,(t)$, $\beta\,(t)$ and $\gamma\,(t)$, see Fig. 3, the relationship between the components of any vector $\mathbf{V}$ expressed in R^g and those expressed in R is described by the following [16]:

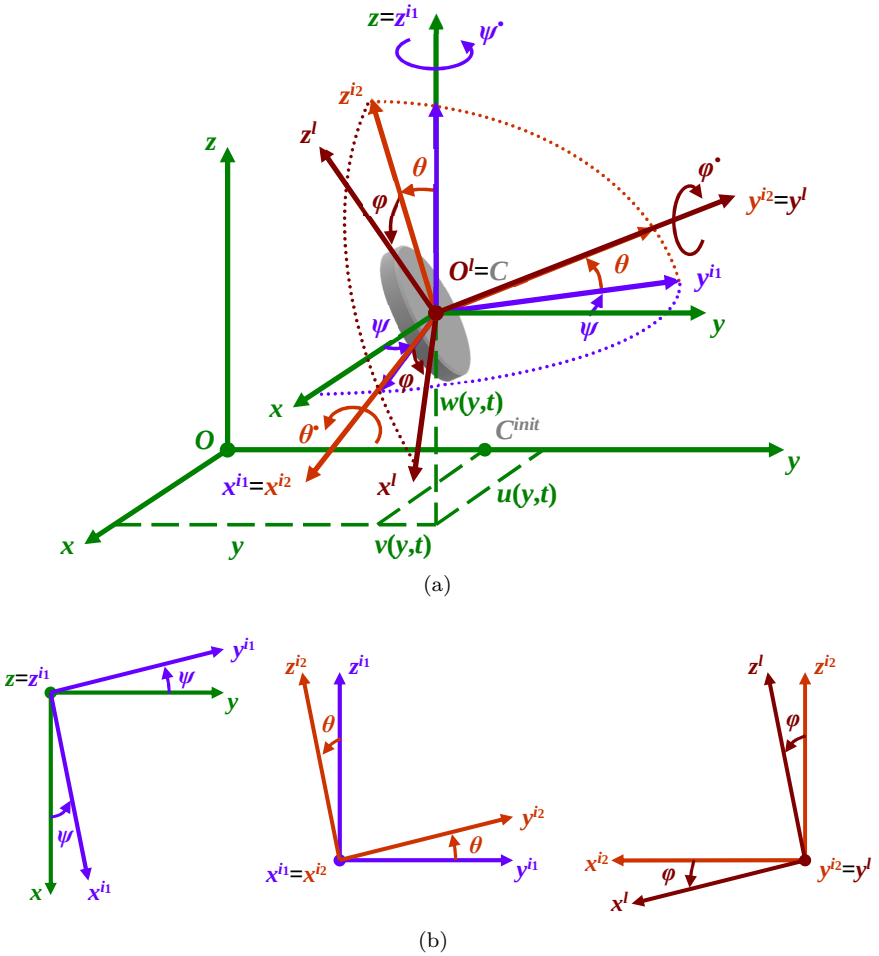

Fig. 2. (a) Transformation between the coordinate system linked with the rotor support R and the local coordinate system R^l. (b) Euler angles for the change of basis.

$$\mathbf{V}|_R = \mathbf{R}_R^{R^g}\mathbf{V}|_{R^g} \quad \text{with} \quad \mathbf{R}_R^{R^g} = \begin{bmatrix} \cos\alpha\cos\gamma - \sin\alpha\sin\beta\sin\gamma & \sin\alpha\cos\gamma + \cos\alpha\sin\beta\sin\gamma & -\cos\beta\sin\gamma \\ -\sin\alpha\cos\beta & \cos\alpha\cos\beta & \sin\beta \\ \cos\alpha\sin\gamma + \sin\alpha\sin\beta\cos\gamma & \sin\alpha\sin\gamma - \cos\alpha\sin\beta\cos\gamma & \cos\beta\cos\gamma \end{bmatrix}, \tag{3}$$

where $\mathbf{R}_R^{R^g}$ is the rotation matrix of the rotor support R with respect to the ground R^g.

The calculation of the energies of the rotor components necessitates establishing the angular velocity vectors of the frames of reference R as well as R^l and the position vector for the origin O of R. The instantaneous angular velocity vector $\boldsymbol{\omega}_{R^l}^R$ of the coordinate system R^l with respect to R is defined by

$$\boldsymbol{\omega}_{R^l}^R = \dot{\theta}\mathbf{x^{i_1}} + \dot{\varphi}\mathbf{y^l} + \dot{\psi}\mathbf{z}, \tag{4}$$

where $\mathbf{x^{i_1}}$, $\mathbf{y^l}$ and $\mathbf{z}$ represent unit vectors along the $O^l x^{i_1}$, $O^l y^l$ and $O^l z$ axes. Let the components of the angular velocity vector $\boldsymbol{\omega}_{R^l}^R$ projected in the local frame R^l be $\omega_1^{x^l}$, $\omega_1^{y^l}$ and $\omega_1^{z^l}$. Their expression is written in the following form [3,16]:

$$\boldsymbol{\omega}_{R^l}^R = \begin{Bmatrix} \omega_1^{x^l} \\ \omega_1^{y^l} \\ \omega_1^{z^l} \end{Bmatrix}_{R^l} = \begin{Bmatrix} -\dot{\psi}\cos\theta\sin\varphi + \dot{\theta}\cos\varphi \\ \dot{\psi}\sin\theta + \dot{\varphi} \\ \dot{\psi}\cos\theta\cos\varphi + \dot{\theta}\sin\varphi \end{Bmatrix}_{R^l}. \tag{5}$$

In the same way as previously, the instantaneous angular velocity vector $\boldsymbol{\omega}_R^{R^g}$, which achieves the orientation of the frame linked with the rotor support R with respect to the Galilean frame R^g, is described in the frame R by

$$\boldsymbol{\omega}_R^{R^g} = \begin{Bmatrix} \omega^x \\ \omega^y \\ \omega^z \end{Bmatrix}_R = \begin{Bmatrix} -\dot{\alpha}\cos\beta\sin\gamma + \dot{\beta}\cos\gamma \\ \dot{\alpha}\sin\beta + \dot{\gamma} \\ \dot{\alpha}\cos\beta\cos\gamma + \dot{\beta}\sin\gamma \end{Bmatrix}_R, \tag{6}$$

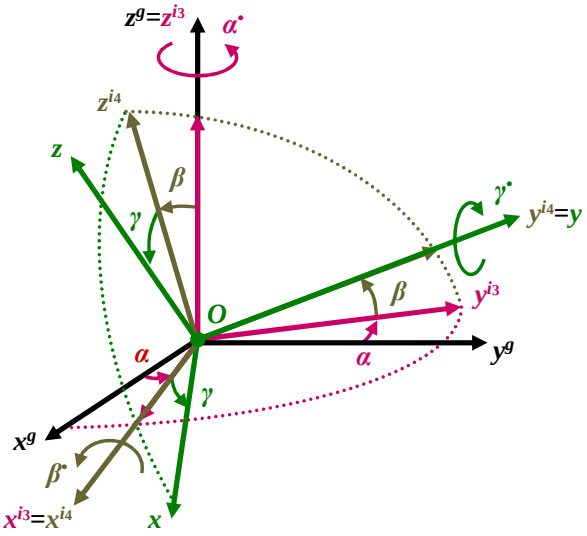

Fig. 3. Transformation between the Galilean coordinate system R^g and the coordinate system attached to the rotor support R.

where ω^x, ω^y and ω^z are defined as the components of the angular velocity vector $\boldsymbol{\omega}_R^{R^g}$ projected in the coordinate system fixed to the support R. Let the components of the angular velocity vector $\boldsymbol{\omega}_R^{R^g}$ of the rigid support R with respect to the ground R^g expressed in the local frame R^l be $\omega_2^{x^l}$, $\omega_2^{y^l}$ and $\omega_2^{z^l}$. Their expressions are obtained by Eq. (2) defining the relationship between the reference frames R and R^l, i.e.,

$$\boldsymbol{\omega}_R^{R^g} = \begin{Bmatrix} \omega_2^{x^l} \\ \omega_2^{y^l} \\ \omega_2^{z^l} \end{Bmatrix}_{R^l} = \mathbf{R}_{R^l}^{R} \begin{Bmatrix} \omega^x \\ \omega^y \\ \omega^z \end{Bmatrix}_{R} = \begin{Bmatrix} (\omega^x \cos\psi + \omega^y \sin\psi)\cos\varphi - ((\omega^x \sin\psi - \omega^y \cos\psi)\sin\theta + \omega^z \cos\theta)\sin\varphi \\ -(\omega^x \sin\psi - \omega^y \cos\psi)\cos\theta + \omega^z \sin\theta \\ ((\omega^x \sin\psi - \omega^y \cos\psi)\sin\theta + \omega^z \cos\theta)\cos\varphi + (\omega^x \cos\psi + \omega^y \sin\psi)\sin\varphi \end{Bmatrix}_{R^l} . \tag{7}$$

Finally, the instantaneous angular velocity vector $\boldsymbol{\omega}_{R^l}^{R^g}$ of the rotor R^l with respect to the ground R^g projected in the local frame of reference R^l represents the sum of the vectors $\boldsymbol{\omega}_{R^l}^{R}$ and $\boldsymbol{\omega}_R^{R^g}$ defined in Eqs. (5) and (7), then

$$\boldsymbol{\omega}_{R^l}^{R^g} = \boldsymbol{\omega}_{R^l}^{R} + \boldsymbol{\omega}_R^{R^g} = \begin{Bmatrix} \omega_1^{x^l} \\ \omega_1^{y^l} \\ \omega_1^{z^l} \end{Bmatrix}_{R^l} + \begin{Bmatrix} \omega_2^{x^l} \\ \omega_2^{y^l} \\ \omega_2^{z^l} \end{Bmatrix}_{R^l} = \begin{Bmatrix} \omega^{x^l} \\ \omega^{y^l} \\ \omega^{z^l} \end{Bmatrix}_{R^l} . \tag{8}$$

The absolute position vector $\mathbf{O^gO}$ of the origin O of the coordinate system attached to the support R projected in the Galilean coordinate system R^g is given as follows:

$$\mathbf{O^gO} = \begin{Bmatrix} x_O^g \\ y_O^g \\ z_O^g \end{Bmatrix}_{R^g} . \tag{9}$$

Inserting Eq. (3) defining the relationship between the frames R^g and R, the position vector $\mathbf{O^gO}$ expressed in the frame R becomes

$$\mathbf{O^gO} = \begin{Bmatrix} x_O \\ y_O \\ z_O \end{Bmatrix}_{R} = \mathbf{R}_R^{R^g} \begin{Bmatrix} x_O^g \\ y_O^g \\ z_O^g \end{Bmatrix}_{R^g} = \begin{Bmatrix} (x_O^g \cos\alpha + y_O^g \sin\alpha)\cos\gamma - ((x_O^g \sin\alpha - y_O^g \cos\alpha)\sin\beta + z_O^g \cos\beta)\sin\gamma \\ -(x_O^g \sin\alpha - y_O^g \cos\alpha)\cos\beta + z_O^g \sin\beta \\ ((x_O^g \sin\alpha - y_O^g \cos\alpha)\sin\beta + z_O^g \cos\beta)\cos\gamma + (x_O^g \cos\alpha + y_O^g \sin\alpha)\sin\gamma \end{Bmatrix}_{R} . \tag{10}$$

Subsequently, the computations are accomplished by employing the rotational $\omega^x(t)$, $\omega^y(t)$, $\omega^z(t)$ and translational $x_O(t)$, $y_O(t)$, $z_O(t)$ components of the support motions (see Fig. 4) as well as their derivatives with respect to time t.

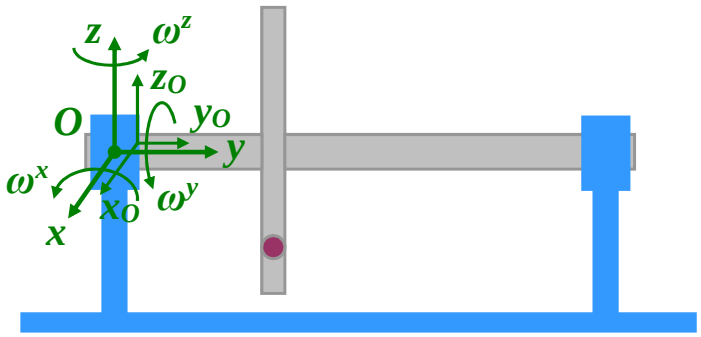

Fig. 4. Rotational and translational motions of the rotor support.

4. Finite element modeling of the on-board rotor-bearing system

In this section, mechanical formulations for the disk, the shaft, the mass unbalance and the hydrodynamic journal bearings are proposed. The kinetic and strain energies of the rotor components are measured by an observer positioned at the ground R^g and their terms are written with respect to the coordinate system connected to the mobile rigid support R. In order to model the on-board rotor, the finite element method based on six degrees of freedom containing the flexural, axial and torsional motions is chosen.

4.1. Disk

The disk is assumed to be rigid according to the assumptions presented in Section 2. As a consequence, only its kinetic energy and the virtual work of its weight are computed. The kinetic energy T_d is composed of the scalar sum of the absolute translational kinetic energy and the absolute rotational kinetic energy about the disk mass center situated at the arbitrary abscissa y_d along the Oy axis [10,11,16,17,20], i.e.,

$$T_d = \frac{m_d}{2}\left(\mathbf{v}_{O_d^l}^{R^g}\right)^T \mathbf{v}_{O_d^l}^{R^g} + \frac{1}{2}\left(\boldsymbol{\omega}_{R^l}^{R^g}\right)^T \mathbf{I}_{m_d}\,\boldsymbol{\omega}_{R^l}^{R^g}; \qquad \text{with} \qquad \mathbf{I}_{m_d} = \operatorname{diag}\left[I_{m_d}^x \quad I_{m_d}^y \quad I_{m_d}^z\right], \tag{11}$$

where the superscript T is the matrix transposition symbol, m_d is the mass of the disk, $\mathbf{v}_{O_d^l}^{R^g}$ is the translational velocity vector of its center O_d^l and $\mathbf{I}_{m_d}$ is its principal inertia tensor. $I_{m_d}^x$, $I_{m_d}^y$ and $I_{m_d}^z$ are the principal moments of inertia of the disk mass about the Ox, Oy and Oz axes respectively. In addition, $I_{m_d}^{mo}$ is utilized to define the mean moment of inertia of the disk mass. Since the disk is symmetric according to the assumptions highlighted in Section 2, $I_{m_d}^x$ and $I_{m_d}^z$ are equal to the mean moment of inertia $I_{m_d}^{mo}$.

The translational velocity vector $\mathbf{v}_{O_d^l}^{R^g}$ is determined by means of the absolute position vector $\mathbf{O^g O_d^l}$ of the disk mass center situated at the arbitrary abscissa y_d related to the frame R. The latter is observed from the ground and expressed in the coordinate system attached to the rotor support R by

$$\mathbf{O^g O_d^l} = \mathbf{O^g O} + \mathbf{O O_d^l} = \begin{Bmatrix} x_O \\ y_O \\ z_O \end{Bmatrix}_R + \begin{Bmatrix} u_d \\ v_d + y_d \\ w_d \end{Bmatrix}_R = \begin{Bmatrix} u_d + x_O \\ v_d + y_d + y_O \\ w_d + z_O \end{Bmatrix}_R. \tag{12}$$

Employing the transport theorem expressing the relationship between the time derivative of a vector measured from a fixed frame of reference and that of the same vector but measured from a moving frame of reference, the derivation of the position vector $\mathbf{O^g O_d^l}$ yields the following formulation:

$$\frac{\mathrm{d}^{R^g}\mathbf{O^g O_d^l}}{\mathrm{d}t} = \frac{\mathrm{d}^{R}\mathbf{O^g O_d^l}}{\mathrm{d}t} + \boldsymbol{\omega}_R^{R^g} \wedge \mathbf{O^g O_d^l} = \mathbf{v}_{O_d^l}^{R^g}; \quad \text{then} \quad \mathbf{v}_{O_d^l}^{R^g} = \begin{Bmatrix} \dot{u}_d + \dot{x}_O + (w_d + z_O)\,\omega^y - (v_d + y_d + y_O)\,\omega^z \\ \dot{v}_d + \dot{y}_O - (w_d + z_O)\,\omega^x + (u_d + x_O)\,\omega^z \\ \dot{w}_d + \dot{z}_O + (v_d + y_d + y_O)\,\omega^x - (u_d + x_O)\,\omega^y \end{Bmatrix}_R. \tag{13}$$

Let $\dot{u}_{O_d^l}$, $\dot{v}_{O_d^l}$ and $\dot{w}_{O_d^l}$ represent the three components of the translational velocity vector $\mathbf{v}_{O_d^l}^{R^g}$ of the disk center. The components of the vector $\boldsymbol{\omega}_{R^l}^{R^g}$ are given by $\omega_d^{x^l}$, $\omega_d^{y^l}$ and $\omega_d^{z^l}$. Thus the following expression of the disk kinetic energy is obtained:

$$T_d = \frac{m_d}{2}\left(\dot{u}_{O_d^l}^2 + \dot{v}_{O_d^l}^2 + \dot{w}_{O_d^l}^2\right) + \frac{1}{2}\left(I_{m_d}^{mo}\,\omega_d^{x^l 2} + I_{m_d}^{y}\,\omega_d^{y^l 2} + I_{m_d}^{mo}\,\omega_d^{z^l 2}\right). \tag{14}$$

The assumptions found in Section 2 state that the rotor runs at a time-varying speed of rotation $\dot{\phi}(t)$. Thus the spinning angle φ and its time derivative $\dot{\varphi}$ are replaced by $\phi + \lambda$ and $\dot{\phi} + \dot{\lambda}$ respectively. The angles of rotation (θ,) and their time derivatives are very small. The trigonometric functions of these angles are consequently replaced by their Taylor series expansion limited at the order 2 and are expressed as $\sin\theta_d \simeq \theta_d$, $\cos\theta_d \simeq 1 - \frac{\theta_d^2}{2}$, $\sin\psi_d \simeq \ _d$ and $\cos\psi_d \simeq 1 - \frac{\psi_d^2}{2}$. On the other hand, the disk weight (effects of gravity) is taken into account and can be defined by

$$\mathbf{F}_d^{W_r} = \mathbf{R}_R^{R^g}\begin{Bmatrix} 0 \\ 0 \\ -m_d\,g \end{Bmatrix}_{R^g} = -m_d\,g\begin{Bmatrix} -\cos\beta\sin\gamma \\ \sin\beta \\ \cos\beta\cos\gamma \end{Bmatrix}_R. \tag{15}$$

The above equation confirms that even if the gravity force of the disk is a constant with respect to the Galilean frame R^g, this force becomes time-variable when it is projected in the frame connected to the support R. Such a change occurs only in the case of rotational motions of the support according to Eq. (15).

The disk is modeled by one-node finite element situated at the geometric center of the shaft cross-sectional area. The node of nodal interpolation corresponds to that n_i of the undeformed shaft finite element esh_i (where i is the shaft finite element number). It is associated with six degrees of freedom $u_{ed}^{n_i}$, $v_{ed}^{n_i}$, $w_{ed}^{n_i}$, $\theta_{ed}^{n_i}$, $\lambda_{ed}^{n_i}$ and $\psi_{ed}^{n_i}$, i.e., transverse and axial translations as well as rotations due to the bending and to the torsion. Thus the nodal displacement vector of the disk finite element expressed in the coordinate system fixed to the rigid support R is given by

$$\boldsymbol{\delta}_{ed}^n = \left[u_{ed}^{n_i}, v_{ed}^{n_i}, w_{ed}^{n_i}, \theta_{ed}^{n_i}, \lambda_{ed}^{n_i}, \psi_{ed}^{n_i}\right]_R^T. \tag{16}$$

After substituting Eq. (16) into Eq. (14), the application of Lagrange's equations to the obtained kinetic energy leads to the following differential equations:

$$\frac{\mathrm{d}}{\mathrm{d}t}\left(\frac{\partial T_{ed}}{\partial \dot{\boldsymbol{\delta}}_{ed}^n}\right) - \frac{\partial T_{ed}}{\partial \boldsymbol{\delta}_{ed}^n} = \mathbf{M}_{ed}\ddot{\boldsymbol{\delta}}_{ed}^n + \mathbf{C}_{ed}(t)\,\dot{\boldsymbol{\delta}}_{ed}^n + \mathbf{K}_{ed}(t)\,\boldsymbol{\delta}_{ed}^n - \mathbf{F}_{ed}^{\lambda}(t) - \mathbf{F}_{ed,su}(t), \tag{17}$$

with

$$\mathbf{M}_{ed} = \mathbf{M}_{ed}^{tr} + \mathbf{M}_{ed}^{ro}, \tag{18}$$

$$\mathbf{C}_{ed}(t) = \mathbf{C}_{ed}^{g}\,\dot{\phi} + \mathbf{C}_{ed,su}^{\omega^x}\,\omega^x + \mathbf{C}_{ed,su}^{\omega^y}\,\omega^y + \mathbf{C}_{ed,su}^{\omega^z}\,\omega^z, \tag{19}$$

$$\begin{aligned}\mathbf{K}_{ed}(t) = {} & \mathbf{K}_{ed}^{g}\,\ddot{\phi} + \mathbf{K}_{ed,su}^{\dot{\omega}^x}\,\dot{\omega}^x + \mathbf{K}_{ed,su}^{\dot{\omega}^y}\,\dot{\omega}^y + \mathbf{K}_{ed,su}^{\dot{\omega}^z}\,\dot{\omega}^z + \mathbf{K}_{ed,su}^{\dot{\phi}\,\omega^y}\,\dot{\phi}\,\omega^y + \mathbf{K}_{ed,su}^{\omega^{x2}}\,\omega^{x2} \\ & + \mathbf{K}_{ed,su}^{\omega^{y2}}\,\omega^{y2} + \mathbf{K}_{ed,su}^{\omega^{z2}}\,\omega^{z2} + \mathbf{K}_{ed,su}^{\omega^x\,\omega^y}\,\omega^x\,\omega^y + \mathbf{K}_{ed,su}^{\omega^x\,\omega^z}\,\omega^x\,\omega^z + \mathbf{K}_{ed,su}^{\omega^y\,\omega^z}\,\omega^y\,\omega^z,\end{aligned} \tag{20}$$

$$\begin{aligned}\mathbf{F}_{ed}^{\lambda}(t) &= -\mathbf{V}_{ed}^{\lambda}\,\ddot{\phi}; \\ \mathbf{F}_{ed,su}(t) &= -\mathbf{V}_{ed,su}^{u}\left(\ddot{x}_O + 2\,\dot{z}_O\,\omega^y - 2\,\dot{y}_O\,\omega^z + z_O\left(\dot{\omega}^y + \omega^x\,\omega^z\right) - y_O\left(\dot{\omega}^z - \omega^x\,\omega^y\right) - x_O\left(\omega^{y2} + \omega^{z2}\right)\right) \\ &\quad - \mathbf{V}_{ed,su}^{v}\left(\ddot{y}_O - 2\,\dot{z}_O\,\omega^x + 2\,\dot{x}_O\,\omega^z - z_O\left(\dot{\omega}^x - \omega^y\,\omega^z\right) + x_O\left(\dot{\omega}^z + \omega^x\,\omega^y\right) - y_O\left(\omega^{x2} + \omega^{z2}\right)\right) \\ &\quad - \mathbf{V}_{ed,su}^{w}\left(\ddot{z}_O + 2\,\dot{y}_O\,\omega^x - 2\,\dot{x}_O\,\omega^y + y_O\left(\dot{\omega}^x + \omega^y\,\omega^z\right) - x_O\left(\dot{\omega}^y - \omega^x\,\omega^z\right) - z_O\left(\omega^{x2} + \omega^{y2}\right)\right) \\ &\quad - \mathbf{V}_{ed,su}^{y\,w}\left(\dot{\omega}^x + \omega^y\,\omega^z\right) + \mathbf{V}_{ed,su}^{y\,u}\left(\dot{\omega}^z - \omega^x\,\omega^y\right) + \mathbf{V}_{ed,su}^{y\,v}\left(\omega^{x2} + \omega^{z2}\right) - \mathbf{V}_{ed,su}^{\theta}\left(\dot{\omega}^x + \omega^y\,\omega^z\right) \\ &\quad - \mathbf{V}_{ed,su}^{\lambda}\,\dot{\omega}^y - \mathbf{V}_{ed,su}^{\psi}\left(\dot{\omega}^z - \omega^x\,\omega^y\right) - \mathbf{V}_{ed,su}^{y\,\psi}\left(\dot{\phi}\,\omega^x + \omega^x\,\omega^y\right) + \mathbf{V}_{ed,su}^{y\,\theta}\left(\dot{\phi}\,\omega^z + \omega^y\,\omega^z\right).\end{aligned} \tag{21}$$

The elementary matrices and vectors of the disk finite element are presented in Appendix A. Finally, the virtual work for the disk weight is formulated and thus the nodal gravity force is obtained as follows:

$$\delta W_{ed} = \left(\mathbf{F}_{ed}^{W_r}\right)^T \delta\boldsymbol{\delta}_{ed}^n; \qquad \text{with} \qquad \mathbf{F}_{ed}^{W_r} = -m_d\,g\left[-\cos\beta\sin\gamma, \sin\beta, \cos\beta\cos\gamma, 0, 0, 0\right]^T. \tag{22}$$

4.2. Shaft

The shaft is assumed to be flexible according to the assumptions presented in Section 2. As a consequence, its kinetic and strain energies and the virtual work of its weight are computed. The kinetic energy of the symmetric shaft element can be determined by taking a shaft elementary volume which can be considered as a symmetric disk of very small thickness dy. Let $\dot{u}_{O^l}$, $\dot{v}_{O^l}$, $\dot{w}_{O^l}$ be the components of the translational velocity vector $\mathbf{v}_{O^l}^{R^g}$ and ω^{x^l}, ω^{y^l}, ω^{z^l} be the components of the instantaneous angular velocity vector $\boldsymbol{\omega}_{R^l}^{R^g}$. As a consequence, the expression for the kinetic energy T_{sh} of the shaft element, whose end-points have the abscissas y_1 and y_2 along the Oy axis, is written hereafter [11,16,17]

$$T_{sh} = \frac{\rho_{sh} S_{sh}}{2} \int_{y_1}^{y_2} \left(\dot{u}_{O^l}^2 + \dot{v}_{O^l}^2 + \dot{w}_{O^l}^2\right) \mathrm{d}y + \frac{\rho_{sh} I_{S_{sh}}^{mo}}{2} \left(\int_{y_1}^{y_2} {\omega^{x^l}}^2 \mathrm{d}y + 2 \int_{y_1}^{y_2} {\omega^{y^l}}^2 \mathrm{d}y + \int_{y_1}^{y_2} {\omega^{z^l}}^2 \mathrm{d}y \right), \tag{23}$$

where ρ_{sh}, S_{sh} and $l_{sh} = y_2 - y_1$ represent respectively the density, the cross-sectional area and the length of the shaft element. $I_{S_{sh}}^{mo} = I_{S_{sh}}^{x} = I_{S_{sh}}^{z}$ is the mean moment of inertia of the cross-sectional area. The rigid support motion with respect to the ground has no influence on the strain energy of the shaft because the latter is related only to the stresses and therefore to the bending, axial and torsional deformations of the shaft with respect to the rotor support R. In addition to the classical linear terms in the strain field due to the bending deformation, another aspect obtained by the bending is taken into account, i.e., the shear effects highlighted by Timoshenko. Thus the expression of the strain energy U_{sh} for the shaft element is of the following form:

$$\begin{aligned} U_{sh} = {} & \frac{E_{sh} I_{S_{sh}}^{mo}}{2} \int_{y_1}^{y_2} \left(\left(\frac{\partial \psi}{\partial y}\right)^2 + \left(\frac{\partial \theta}{\partial y}\right)^2 \right) \mathrm{d}y + \frac{G_{sh} \kappa_{sh}^{mo} S_{sh}}{2} \int_{y_1}^{y_2} \left(\left(\frac{\partial u}{\partial y} + \psi\right)^2 + \left(\frac{\partial w}{\partial y} - \theta\right)^2 \right) \mathrm{d}y \\ & + \frac{E_{sh} S_{sh}}{2} \int_{y_1}^{y_2} \left(\frac{\partial v}{\partial y}\right)^2 \mathrm{d}y + G_{sh} I_{S_{sh}}^{mo} \int_{y_1}^{y_2} \left(\frac{\partial \lambda}{\partial y}\right)^2 \mathrm{d}y, \end{aligned} \tag{24}$$

where E_{sh}, $G_{sh} = \frac{E_{sh}}{2(1+\nu_{sh})}$ and ν_{sh} are respectively Young's modulus, the shear modulus and Poisson's ratio of the isotropic homogeneous shaft material. $\kappa_{sh}^{mo} = \kappa_{sh}^{x} = \kappa_{sh}^{z}$ represents the mean shear correction factor of the cross-sectional area of the shaft. Moreover, the shaft weight can be obtained by considering a shaft elementary volume equivalent to a disk of very small thickness dy. It is described by

$$\mathbf{F}_{sh}^{W_r} = \int_{y_1}^{y_2} \mathbf{R}_R^{R^g} \begin{Bmatrix} 0 \\ 0 \\ -\rho_{sh} S_{sh}\, g \end{Bmatrix}_{R^g} \mathrm{d}y = -\rho_{sh} S_{sh}\, g \int_{y_1}^{y_2} \begin{Bmatrix} -\cos\beta \sin\gamma \\ \sin\beta \\ \cos\beta \cos\gamma \end{Bmatrix}_{R} \mathrm{d}y. \tag{25}$$

The shaft is modeled with n_{esh} two-node beam finite elements and thus possesses $n_{esh}+1$ nodes. Let us consider an undeformed shaft finite element esh_i which consists of two nodes n_i and n_{i+1} of coordinates $y_{sh}^{n_i}$ and $y_{sh}^{n_{i+1}}$ along the Oy axis. This finite element is of density ρ_{esh_i}, cross-sectional area S_{esh_i}, length l_{esh_i}, moment of inertia $I_{S_{esh_i}}^{mo}$, Young's modulus E_{esh_i}, Poisson's ratio ν_{esh_i} as well as shear correction factor $\kappa_{esh_i}^{mo}$ where $i\,(1 \leq i \leq n_{esh})$ is the shaft finite element number. Considering six degrees of freedom for each node, the nodal displacement vector of this finite element projected in the reference frame fixed to the rigid support R is given as

$$\boldsymbol{\delta}_{esh_i}^{n} = \left[u_{esh_i}^{n_i}, v_{esh_i}^{n_i}, w_{esh_i}^{n_i}, \theta_{esh_i}^{n_i}, \lambda_{esh_i}^{n_i}, \psi_{esh_i}^{n_i}, u_{esh_i}^{n_{i+1}}, v_{esh_i}^{n_{i+1}}, w_{esh_i}^{n_{i+1}}, \theta_{esh_i}^{n_{i+1}}, \lambda_{esh_{i+1}}^{n_{i+1}}, \psi_{esh_i}^{n_{i+1}}\right]_R^T. \tag{26}$$

The dynamic transverse displacements u_{esh_i}, w_{esh_i} and the axial displacement v_{esh_i} of any point C^{init} respectively along the Ox, Oz and Oy axes of the frame R as well as the rotations θ_{esh_i}, ψ_{esh_i}, λ_{esh_i} respectively around the Ox, Oz and Oy directions due to the bending and to the torsion are formulated as a function of the nodal displacement vector $\boldsymbol{\delta}_{esh_i}^{n}$ as follows:

$$\begin{aligned} u_{esh_i} &= \bar{\mathbf{F}}_{esh_i}^{u}(\bar{y})\, \boldsymbol{\delta}_{esh_i}^{n}; & w_{esh_i} &= \bar{\mathbf{F}}_{esh_i}^{w}(\bar{y})\, \boldsymbol{\delta}_{esh_i}^{n}; & v_{esh_i} &= \bar{\mathbf{F}}_{esh_i}^{v}(\bar{y})\, \boldsymbol{\delta}_{esh_i}^{n}; \\ \theta_{esh_i} &= \bar{\mathbf{F}}_{esh_i}^{\theta}(\bar{y})\, \boldsymbol{\delta}_{esh_i}^{n}; & \psi_{esh_i} &= \bar{\mathbf{F}}_{esh_i}^{\psi}(\bar{y})\, \boldsymbol{\delta}_{esh_i}^{n}; & \lambda_{esh_i} &= \bar{\mathbf{F}}_{esh_i}^{\lambda}(\bar{y})\, \boldsymbol{\delta}_{esh_i}^{n}, \end{aligned} \tag{27}$$

where $\bar{\mathbf{F}}_{esh_i}^{u}$, $\bar{\mathbf{F}}_{esh_i}^{w}$, $\bar{\mathbf{F}}_{esh_i}^{\theta}$ and $\bar{\mathbf{F}}_{esh_i}^{\psi}$ are the shape function vectors of a Timoshenko beam finite element regarding the flexural motions. They involve the shear effects, are described as a function of the dimensionless variable $\bar{y}$ ($\bar{y} = \frac{y}{l_{esh_i}}$) along the Oy axis of the frame R and represent third-degree and second-degree polynomial equations (see Chen and

Ku [34]). The shape function vectors $\bar{\mathbf{F}}^{v}_{esh_i}$ and $\bar{\mathbf{F}}^{\lambda}_{esh_i}$ for the axial and torsional motions are first-degree polynomial equations (i.e., the classical linear Lagrange shape function vectors).

After inserting Eq. (27) in Eqs. (23) and (24), the application of Lagrange's equations to the resulting kinetic and strain energies yields the differential equations of motion of the shaft finite element described by

$$\frac{\mathrm{d}}{\mathrm{d}t}\left(\frac{\partial T_{esh_i}}{\partial \dot{\boldsymbol{\delta}}^{n}_{esh_i}}\right) - \frac{\partial T_{esh_i}}{\partial \boldsymbol{\delta}^{n}_{esh_i}} + \frac{\partial U_{esh_i}}{\partial \boldsymbol{\delta}^{n}_{esh_i}} = \mathbf{M}_{esh_i}\ddot{\boldsymbol{\delta}}^{n}_{esh_i} + \mathbf{C}_{esh_i}(t)\,\dot{\boldsymbol{\delta}}^{n}_{esh_i} + \mathbf{K}_{esh_i}(t)\,\boldsymbol{\delta}^{n}_{esh_i} - \mathbf{F}^{\lambda}_{esh_i}(t) - \mathbf{F}_{esh_i,su}(t), \tag{28}$$

with

$$\mathbf{M}_{esh_i} = \mathbf{M}^{tr}_{esh_i} + \mathbf{M}^{ro}_{esh_i}, \tag{29}$$

$$\mathbf{C}_{esh_i}(t) = \mathbf{C}^{g}_{esh_i}\,\dot{\phi} + \mathbf{C}^{\omega^x}_{esh_i,su}\,\omega^x + \mathbf{C}^{\omega^y}_{esh_i,su}\,\omega^y + \mathbf{C}^{\omega^z}_{esh_i,su}\,\omega^z, \tag{30}$$

$$\begin{aligned}\mathbf{K}_{esh_i}(t) = {} & \mathbf{K}^{e}_{esh_i} + \mathbf{K}^{g}_{esh_i}\,\ddot{\phi} + \mathbf{K}^{\dot{\omega}^x}_{esh_i,su}\,\dot{\omega}^x + \mathbf{K}^{\dot{\omega}^y}_{esh_i,su}\,\dot{\omega}^y + \mathbf{K}^{\dot{\omega}^z}_{esh_i,su}\,\dot{\omega}^z + \mathbf{K}^{\dot{\phi}\,\omega^y}_{esh_i,su}\,\dot{\phi}\,\omega^y \\ & + \mathbf{K}^{\omega^{x2}}_{esh_i,su}\,\omega^{x2} + \mathbf{K}^{\omega^{y2}}_{esh_i,su}\,\omega^{y2} + \mathbf{K}^{\omega^{z2}}_{esh_i,su}\,\omega^{z2} + \mathbf{K}^{\omega^x\,\omega^y}_{esh_i,su}\,\omega^x\,\omega^y + \mathbf{K}^{\omega^x\,\omega^z}_{esh_i,su}\,\omega^x\,\omega^z \\ & + \mathbf{K}^{\omega^y\,\omega^z}_{esh_i,su}\,\omega^y\,\omega^z,\end{aligned} \tag{31}$$

$$\begin{aligned}\mathbf{F}^{\lambda}_{esh_i}(t) &= -\mathbf{V}^{\lambda}_{esh_i}\,\ddot{\phi}; \\ \mathbf{F}_{esh_i,su}(t) &= -\mathbf{V}^{u}_{esh_i,su}\left(\ddot{x}_O + 2\,\dot{z}_O\,\omega^y - 2\,\dot{y}_O\,\omega^z + z_O\,(\dot{\omega}^y + \omega^x\,\omega^z) - y_O\,(\dot{\omega}^z - \omega^x\,\omega^y) - x_O\left(\omega^{y2} + \omega^{z2}\right)\right) \\ &\quad - \mathbf{V}^{v}_{esh_i,su}\left(\ddot{y}_O - 2\,\dot{z}_O\,\omega^x + 2\,\dot{x}_O\,\omega^z - z_O\,(\dot{\omega}^x - \omega^y\,\omega^z) + x_O\,(\dot{\omega}^z + \omega^x\,\omega^y) - y_O\left(\omega^{x2} + \omega^{z2}\right)\right) \\ &\quad - \mathbf{V}^{w}_{esh_i,su}\left(\ddot{z}_O + 2\,\dot{y}_O\,\omega^x - 2\,\dot{x}_O\,\omega^y + y_O\,(\dot{\omega}^x + \omega^y\,\omega^z) - x_O\,(\dot{\omega}^y - \omega^x\,\omega^z) - z_O\left(\omega^{x2} + \omega^{y2}\right)\right) \\ &\quad - \mathbf{V}^{y\,w}_{esh_i,su}\,(\dot{\omega}^x + \omega^y\,\omega^z) + \mathbf{V}^{y\,u}_{esh_i,su}\,(\dot{\omega}^z - \omega^x\,\omega^y) + \mathbf{V}^{y\,v}_{esh_i,su}\left(\omega^{x2} + \omega^{z2}\right) - \mathbf{V}^{\theta}_{esh_i,su}\,(\dot{\omega}^x + \omega^y\,\omega^z) \\ &\quad - \mathbf{V}^{\lambda}_{esh_i,su}\,\dot{\omega}^y - \mathbf{V}^{\psi}_{esh_i,su}\,(\dot{\omega}^z - \omega^x\,\omega^y) - \mathbf{V}^{y\,\psi}_{esh_i,su}\left(\dot{\phi}\,\omega^x + \omega^x\,\omega^y\right) + \mathbf{V}^{y\,\theta}_{esh_i,su}\left(\dot{\phi}\,\omega^z + \omega^y\,\omega^z\right).\end{aligned} \tag{32}$$

As can be seen in Eqs. (28)–(32), the only difference with respect to the disk matrices is the stiffness matrix due to the shaft elasticity. This matrix comprises the effects related to the streching and torsional motions, to the linear bending deformation as well as to the shear deformation. Finally, the calculations of the elementary matrices and vectors for the shaft finite element are provided in Appendix A. Lastly, the virtual work for the gravity load due to the shaft finite element is constructed and thus the nodal gravity force is deduced as follows:

$$\delta W_{sh} = \int_{y_1}^{y_2}\left(\mathrm{d}\mathbf{F}^{W_r}_{sh}\right)^T\delta\boldsymbol{\delta}_{esh_i} \qquad \Rightarrow \qquad \delta W_{esh_i} = \left(\mathbf{F}^{W_r}_{esh_i}\right)^T\delta\boldsymbol{\delta}^{n}_{esh_i};$$

$$\text{with} \qquad \mathbf{F}^{W_r}_{esh_i} = -\rho_{esh_i}S_{esh_i}l_{esh_i}\,g\int_0^1\left(-\left(\bar{\mathbf{F}}^{u}_{esh_i}\right)^T\cos\beta\sin\gamma + \left(\bar{\mathbf{F}}^{v}_{esh_i}\right)^T\sin\beta + \left(\bar{\mathbf{F}}^{w}_{esh_i}\right)^T\cos\beta\cos\gamma\right)\mathrm{d}\bar{y}, \tag{33}$$

where the displacement vector $\boldsymbol{\delta}_{esh_i}$ includes u_{esh_i}, v_{esh_i}, w_{esh_i}, θ_{esh_i}, λ_{esh_i} and $\quad_{esh_i}$ respectively.

4.3. Mass unbalance

The mass unbalance is modeled by a lumped mass m_{mu} situated at a point P_{mu} with a distance r_{mu} from the geometric center of the cross-sectional area of the shaft. Its initial phase angle with the $O^l z^l$ axis of the local coordinate system R^l (which coincides with the Oz axis of the frame of reference R at rest) is η_{mu}. In the existing literature [3,11,15–17], the mass unbalance is assumed to remain in a plane perpendicular to the Oy axis. Therefore it is not affected by the rotations θ and ψ around the transverse directions but only by the transverse displacements u and w. In this work, a more rigorous case is selected and the previous assumption is not kept. When the shaft is deformed during the operation of the rotor, the angle of the mass unbalance with the $O^l z^l$ axis remains η_{mu} and its coordinates expressed in R^l are given by the vector $\left[x^l_{mu} = r_{mu}\sin\eta_{mu}, 0, z^l_{mu} = r_{mu}\cos\eta_{mu}\right]^T_{R^l}$. The mass unbalance kinetic energy T_{mu} is presented as follows:

$$T_{mu} = \frac{m_{mu}}{2} \left(\mathbf{v}^{R^g}_{P_{mu}} \right)^T \mathbf{v}^{R^g}_{P_{mu}}. \tag{34}$$

The translational velocity vector $\mathbf{v}^{R^g}_{P_{mu}}$ is found through the absolute position vector $\mathbf{O^g P_{mu}}$ of the mass unbalance. The latter is measured from the ground and can be written with respect to the coordinate systems R and R^l by the following expression:

$$\mathbf{O^g P_{mu}} = \mathbf{O^g O^l_{mu}} + \mathbf{O^l_{mu} P_{mu}} = \left\{ \begin{array}{c} u_{mu} + x_O \\ v_{mu} + y_{mu} + y_O \\ w_{mu} + z_O \end{array} \right\}_R + \left\{ \begin{array}{c} x^l_{mu} \\ 0 \\ z^l_{mu} \end{array} \right\}_{R^l}. \tag{35}$$

The time derivative of the absolute position vector $\mathbf{O^g P_{mu}}$ consists of the sum of the derivatives of the vectors $\mathbf{O^g O^l_{mu}}$ as well as $\mathbf{O^l_{mu} P_{mu}}$ and is given by

$$\frac{\mathrm{d}^{R^g} \mathbf{O^g P_{mu}}}{\mathrm{d}t} = \frac{\mathrm{d}^{R^g} \mathbf{O^g O^l_{mu}}}{\mathrm{d}t} + \frac{\mathrm{d}^{R^g} \mathbf{O^l_{mu} P_{mu}}}{\mathrm{d}t} = \mathbf{v}^{R^g}_{P_{mu}}. \tag{36}$$

Using the transport theorem explained previously in Section 4.1, the time derivative of the absolute position vector $\mathbf{O^g O^l_{mu}}$ of the shaft geometric center is described by

$$\frac{\mathrm{d}^{R^g} \mathbf{O^g O^l_{mu}}}{\mathrm{d}t} = \frac{\mathrm{d}^{R} \mathbf{O^g O^l_{mu}}}{\mathrm{d}t} + \boldsymbol{\omega}^{R^g}_R \wedge \mathbf{O^g O^l_{mu}} = \left\{ \begin{array}{c} \dot{u}_{mu} + \dot{x}_O + (w_{mu} + z_O)\,\omega^y - (v_{mu} + y_{mu} + y_O)\,\omega^z \\ \dot{v}_{mu} + \dot{y}_O - (w_{mu} + z_O)\,\omega^x + (u_{mu} + x_O)\,\omega^z \\ \dot{w}_{mu} + \dot{z}_O + (v_{mu} + y_{mu} + y_O)\,\omega^x - (u_{mu} + x_O)\,\omega^y \end{array} \right\}_R. \tag{37}$$

The time derivative of the vector $\mathbf{O^l_{mu} P_{mu}}$ measured from the local coordinate system R^l (i.e., $\frac{\mathrm{d}^{R^l} \mathbf{O^l_{mu} P_{mu}}}{\mathrm{d}t}$) is nil because the coordinates of the mass unbalance are constant with respect to R^l. Thus by means of the transport theorem, the time derivative of the vector $\mathbf{O^l_{mu} P_{mu}}$ measured from the Galilean frame R^g and expressed in the local frame R^l is obtained, then

$$\frac{\mathrm{d}^{R^g} \mathbf{O^l_{mu} P_{mu}}}{\mathrm{d}t} = \boldsymbol{\omega}^{R^g}_{R^l} \wedge \mathbf{O^l_{mu} P_{mu}} = \left\{ \begin{array}{c} z^l_{mu}\omega^y \\ -\left(z^l_{mu}\omega^x - x^l_{mu}\omega^z \right) \\ -x^l_{mu}\omega^y \end{array} \right\}_{R^l}. \tag{38}$$

Finally, the translational velocity vector $\mathbf{v}^{R^g}_{P_{mu}}$ projected in the frame R is calculated by introducing Eqs. (2), (37) and (38) into Eq. (36), i.e.,

$$\mathbf{v}^{R^g}_{P_{mu}} = \left\{ \begin{array}{c} \dot{u}_{mu} + \dot{x}_O + (w_{mu} + z_O)\,\omega^y - (v_{mu} + y_{mu} + y_O)\,\omega^z \\ \dot{v}_{mu} + \dot{y}_O - (w_{mu} + z_O)\,\omega^x + (u_{mu} + x_O)\,\omega^z \\ \dot{w}_{mu} + \dot{z}_O + (v_{mu} + y_{mu} + y_O)\,\omega^x - (u_{mu} + x_O)\,\omega^y \end{array} \right\}_R + \left(\mathbf{R}^R_{R^l} \right)^T \left\{ \begin{array}{c} z^l_{mu}\omega^y \\ -\left(z^l_{mu}\omega^x - x^l_{mu}\omega^z \right) \\ -x^l_{mu}\omega^y \end{array} \right\}_{R^l}. \tag{39}$$

The mass unbalance is modeled by one-node finite elements located at the geometric center of the cross-sectional area of the shaft. The node attached to that n_i of the undeformed shaft finite element esh_i includes six degrees of freedom $u^{n_i}_{emu}$, $v^{n_i}_{emu}$, $w^{n_i}_{emu}$, $\theta^{n_i}_{emu}$, $\lambda^{n_i}_{emu}$ and $\psi^{n_i}_{emu}$ associated with lateral and axial translations as well as with rotations due to the flexural and torsional motions. Thus the nodal displacement vector of the mass unbalance finite element expressed in the coordinate system fixed to the mobile rigid support R is defined by

$$\boldsymbol{\delta}^n_{emu} = \left[u^{n_i}_{emu}, v^{n_i}_{emu}, w^{n_i}_{emu}, \theta^{n_i}_{emu}, \lambda^{n_i}_{emu}, \psi^{n_i}_{emu} \right]^T_R. \tag{40}$$

After substituting Eq. (40) into Eq. (34), the application of Lagrange's equations to the obtained kinetic energy leads to the differential equations of motion of the mass unbalance finite element written in the following form:

$$\frac{\mathrm{d}}{\mathrm{d}t} \left(\frac{\partial T_{emu}}{\partial \dot{\boldsymbol{\delta}}^n_{emu}} \right) - \frac{\partial T_{emu}}{\partial \boldsymbol{\delta}^n_{emu}} = \mathbf{M}_{emu}(t)\, \ddot{\boldsymbol{\delta}}^n_{emu} + \mathbf{C}_{emu}(t)\, \dot{\boldsymbol{\delta}}^n_{emu} + \mathbf{K}_{emu}(t)\, \boldsymbol{\delta}^n_{emu} - \mathbf{F}_{emu}(t) - \mathbf{F}_{emu,su}(t), \tag{41}$$

with

$$\mathbf{M}_{emu}(t) = \mathbf{M}^{cs}_{emu}; \qquad \mathbf{C}_{emu}(t) = \mathbf{C}^{\dot{\phi}}_{emu}\, \dot{\phi} + \mathbf{C}_{emu,su}, \tag{42}$$

$$\mathbf{K}_{emu}(t) = \mathbf{K}^{\ddot{\phi}}_{emu}\,\ddot{\phi} + \mathbf{K}^{\dot{\phi}^2}_{emu}\,\dot{\phi}^2 + \mathbf{K}_{emu,su}, \tag{43}$$

$$\mathbf{F}_{emu}(t) = \mathbf{V}^{\ddot{\phi}}_{emu}\,\ddot{\phi} + \mathbf{V}^{\dot{\phi}^2}_{emu}\,\dot{\phi}^2; \qquad \mathbf{F}_{emu,su}(t) = f\left(\omega^x, \omega^y, \omega^z, x_O, y_O, z_O\right). \tag{44}$$

It should be clarified that these equations of motion show not only external force vectors (such as centripetal and centrifugal force vectors obtained classically by the application of Lagrange's equations to the kinetic energy of the mass unbalance) but also mass, damping and stiffness matrices. This is because the mass unbalance is not neglected despite its small value compared to the mass of the disk and the shaft. Furthermore, in the presence of sinusoidal motions of the support, the excitation due to the mass unbalance combined with the support motions has not only a frequency equal to the speed of rotation $\dot{\phi}$ of the rotor but also a support motion frequency and a combination of both frequencies. The original elementary matrices and vectors of the mass unbalance finite element are presented in Appendix A. They are expressed as a function of $x^* = x^l_{mu}\cos\phi + z^l_{mu}\sin\phi$ and $z^* = -x^l_{mu}\sin\phi + z^l_{mu}\cos\phi$ which represent the coordinates projected in the frame R if the mass unbalance is situated in a plane perpendicular to the Oy axis.

4.4. Hydrodynamic journal bearing

Fig. 5 shows a schematic diagram of a hydrodynamic journal bearing. The latter is usually composed of a fixed bronze bush containing a rotating shaft and of a lubricant separating these two components. Let r_{be}, l_{be}, $c_{be} = r_{be} - r_{sh}$ (where r_{sh} is the shaft radius) and μ_{be} be the radius, length, clearance and fluid film dynamic viscosity of the bearing respectively. The bearing center and the shaft geometric center are respectively the points C^{init} and O^l. For a given speed of rotation $\dot{\phi}$ of the rotor and a static load W_r created by the rotor weight, the shaft geometric center O^l in the bearing holds a static equilibrium position C^0_{be} described by the displacement vector $\boldsymbol{\delta}^0_{be} = \left[u^0_{be}, w^0_{be}\right]^T_R$ projected in the frame R or equivalently by the relative static eccentricity $\varepsilon^0_{be} = \frac{e^0_{be}}{c_{be}} = \frac{\|\boldsymbol{\delta}^0_{be}\|}{c_{be}}$ of the shaft center within the bearing and the attitude angle φ^0_{be} between the load direction and the line relating the centers C^{init} and O^l.

In the dynamic regime, the transverse displacement vector $\boldsymbol{\delta}_{be} = \left[u_{be}, w_{be}\right]^T_R$ of the shaft geometric center in the bearing is produced due to the variation of forces applied to the rotor (mass unbalance, fluid film forces and support excitations). Assuming an isothermal and laminar flow of an isoviscous incompressible fluid, the pressure distribution p_{be} in the hydrodynamic bearing is governed by the Reynolds equation which can be found in [33] and given by

$$\frac{\partial}{\partial s^{ci}_{be}}\left(h^3_{be}\frac{\partial p_{be}}{\partial s^{ci}_{be}}\right) + \frac{\partial}{\partial s^{ax}_{be}}\left(h^3_{be}\frac{\partial p_{be}}{\partial s^{ax}_{be}}\right) = 6\mu_{be}\left(r_{be}\left(\dot{\phi} - 2\dot{\varphi}_{be}\right)\frac{\partial h_{be}}{\partial s^{ci}_{be}} + 2\dot{e}_{be}\cos\left(\frac{s^{ci}_{be}}{r_{be}}\right)\right), \tag{45}$$

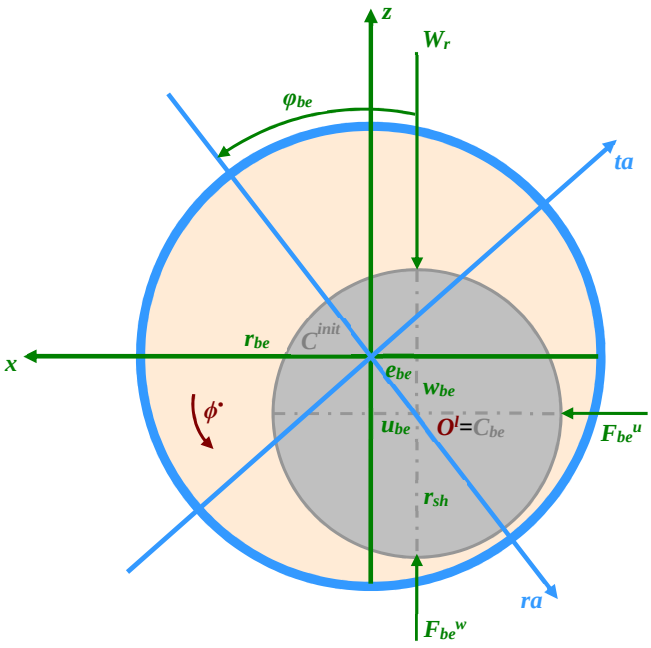

Fig. 5. Simple representation of a hydrodynamic journal bearing.

where h_{be}, s_{be}^{ci} and s_{be}^{ax} are respectively the oil film thickness, the circumferential and axial coordinates. In this study, the hydrodynamic finite-length bearing is considered. The difficulty to obtain a satisfactory solution for this bearing concerns not only the form of the Reynolds equation to be used but also the boundary conditions. Therefore this type of bearing has no analytical solution. The classical numerical technique considered as a reference method and called "finite difference method" [35] is exploited to solve the Reynolds equation and to compute the hydrodynamic fluid pressure distribution. This technique is a first-order 2D method. The mesh has a discretization with rectangular elements and a number of nodes equal to 200 and 15 successively in the circumferential and axial directions. The external hydrodynamic forces $\mathbf{F}_{be} = \left[F_{be}^{u}, F_{be}^{w}\right]_{R}^{T}$ acting on the shaft can be deduced from the integration of the fluid film pressure field over the bearing by employing the Gümbel boundary conditions which reject the negative pressure from the integral. In [33], the Gümbel conditions utilize the positive pressure involved in the classical interval $\theta_{be} \in [0;\, \pi \text{ rad}]$. In [36], these conditions are improved for hydrodynamic short bearings and the positive pressure appears all along the interval $\theta_{be} \in [\beta_{be};\, \beta_{be} + \pi \text{ rad}]$ (where $\beta_{be} > 0$) instead of the classical one. Here, the positive pressure may begin to appear at $\theta_{be} = 0$ but the interval length of π rad is not ensured. The fluid film forces $\mathbf{F}_{be}$ depend nonlinearly on the dynamic transverse displacement and velocity vectors $\boldsymbol{\delta}_{be}, \dot{\boldsymbol{\delta}}_{be}$.

In the present article, the transverse dynamic displacements of the shaft elastic line are supposed to be small in the vicinity of the static position. Therefore the linear analysis of bearings can be applied by building a first-order Taylor expansion of the fluid film forces as follows:

$$\mathbf{F}_{be}\left(\boldsymbol{\delta}_{be}, \dot{\boldsymbol{\delta}}_{be}\right) = \mathbf{F}_{be}\left(\boldsymbol{\delta}_{be}^{0}, \mathbf{0}\right) - \mathbf{c}_{be}\boldsymbol{\Delta}\dot{\boldsymbol{\delta}}_{be} - \mathbf{k}_{be}\boldsymbol{\Delta}\boldsymbol{\delta}_{be}, \tag{46}$$

with

$$\mathbf{c}_{be} = -\frac{\partial \mathbf{F}_{be}\left(\boldsymbol{\delta}_{be}^{0}, \mathbf{0}\right)}{\partial \dot{\boldsymbol{\delta}}_{be}}; \qquad \mathbf{k}_{be} = -\frac{\partial \mathbf{F}_{be}\left(\boldsymbol{\delta}_{be}^{0}, \mathbf{0}\right)}{\partial \boldsymbol{\delta}_{be}}; \qquad \boldsymbol{\Delta}\dot{\boldsymbol{\delta}}_{be} = \dot{\boldsymbol{\delta}}_{be}; \qquad \boldsymbol{\Delta}\boldsymbol{\delta}_{be} = \boldsymbol{\delta}_{be} - \boldsymbol{\delta}_{be}^{0}. \tag{47}$$

The static hydrodynamic force vector $\mathbf{F}_{be}\left(\boldsymbol{\delta}_{be}^{0}, \mathbf{0}\right)$ is related to the static displacement vector and must equilibrate the static load W_r imposed by the rotor weight. The damping and stiffness matrices $\mathbf{c}_{be}$, $\mathbf{k}_{be}$ of the linearized hydrodynamic bearing depend only on the static position $\boldsymbol{\delta}_{be}^{0}$. Since the bearing contributes to the rotor as external forces, the virtual work for the bearing finite element has to be established in order to apply Lagrange's equations

$$\delta W_{ebe} = \mathbf{F}_{ebe}^{T}\left(\boldsymbol{\delta}_{ebe}^{n}, \dot{\boldsymbol{\delta}}_{ebe}^{n}\right)\delta\boldsymbol{\delta}_{ebe}^{n}, \tag{48}$$

where $\boldsymbol{\delta}_{ebe}^{n}$ is the nodal displacement vector of the bearing finite element expressed in the coordinate system attached to the rigid support R and is similar to that of the disk.

If the short bearing theory is considered (i.e., $\frac{l_{be}}{d_{be}} \leq \frac{1}{8}$ where $d_{be} = 2r_{be}$), the circumferential pressure gradient can be neglected when compared with the axial pressure gradient. This assumption permits obtaining an analytical solution of the Reynolds equation which yields the fluid film pressure distribution and the nonlinear hydrodynamic forces (whose formulations can be found in [33]). The hydrodynamic short bearing can be analytically linearized in order to produce the constant damping and stiffness coefficients as shown in [33].

5. Governing equations and dynamic analysis

5.1. Equations of motion of the on-board rotor

The resulting elementary matrices and vectors for the disk, shaft, mass unbalance and hydrodynamic journal bearing finite elements are appropriately assembled. The boundary conditions do not exist because of the presence of hydrodynamic bearings. Thus the global matrices and vectors have dimensions $n_g \times n_g$ and $n_g \times 1$ respectively where the total number of degrees of freedom n_g is usually equal to $6\,(n_{esh} + 1)$. The governing linear second-order differential equations describing the dynamic behavior of the on-board rotor-bearing system running at a time-varying speed of rotation are written with respect to the non-inertial coordinate system fixed to the support R by the following:

$$\mathbf{M}_r\,(t)\,\ddot{\boldsymbol{\delta}}_r + \mathbf{C}_r\,(t)\,\dot{\boldsymbol{\delta}}_r + \mathbf{K}_r\,(t)\,\boldsymbol{\delta}_r = \mathbf{F}_r\,(t) + \mathbf{F}_{be}\left(\boldsymbol{\delta}_r^{0}, \mathbf{0}\right) + \mathbf{K}_{be}\boldsymbol{\delta}_r^{0}, \tag{49}$$

where $\mathbf{M}_r\,(t)$, $\mathbf{C}_r\,(t)$ and $\mathbf{K}_r\,(t)$ are the global mass, damping and stiffness matrices of the rotor with time-varying parametric terms due to the mass unbalance, to the support rotations, to the coupling between both phenomena and to the combination of mass unbalance and support translations. $\boldsymbol{\delta}_r$, $\dot{\boldsymbol{\delta}}_r$ and $\ddot{\boldsymbol{\delta}}_r$ represent the global displacement,

velocity and acceleration vectors conforming to the connectivity of the finite elements. $\mathbf{F}_r\,(t)$ is defined as the global linear external force vector containing the excitations due to the influence of the non-stationary speed of rotation of the rotor, the mass unbalance as well as to that of the rotational and translational motions of the support. When there are no support rotations, the hydrodynamic force vector $\mathbf{F}_{be}\left(\boldsymbol{\delta}_r^0, \mathbf{0}\right)$ is a function of the static solution vector $\boldsymbol{\delta}_r^0$ caused by the static equilibrium between the rotor weight vector $\mathbf{F}_{d,sh}^{W_r}$ and the hydrodynamic bearing reaction. In the case of rotational motions of the support, the rotor weight vector is no longer a constant with respect to the frame of reference R and must be projected in this frame. The components of this vector relevant to the translational degrees of freedom u, v and w comprise (after the projection) the amounts $-\cos\beta\sin\gamma$, $\sin\beta$ and $\cos\beta\cos\gamma$ respectively. This result is in agreement with that of the work of Chen et al. [27] regarding the bending degrees of freedom. The matrices $\mathbf{M}_r\,(t)$, $\mathbf{C}_r\,(t)$ and $\mathbf{K}_r\,(t)$ involved in Eq. (49) are expressed as follows:

$$\mathbf{M}_r\,(t) = \mathbf{M}_{d,sh}^{tr} + \mathbf{M}_{d,sh}^{ro} + \mathbf{M}_{mu}^{cs}, \tag{50}$$

$$\mathbf{C}_r\,(t) = \mathbf{C}_{be} + \mathbf{C}_{sh}^{sd} + \mathbf{C}_{d,sh}^{g}\,\dot{\phi} + \mathbf{C}_{mu}^{\dot{\phi}}\,\dot{\phi} + \mathbf{C}_{d,sh,su}^{\omega^x}\,\omega^x + \mathbf{C}_{d,sh,su}^{\omega^y}\,\omega^y + \mathbf{C}_{d,sh,su}^{\omega^z}\,\omega^z + \mathbf{C}_{mu,su}, \tag{51}$$

$$\begin{aligned}\mathbf{K}_r\,(t) = {} & \mathbf{K}_{be} + \mathbf{K}_{sh}^{e} + \mathbf{K}_{d,sh}^{g}\,\ddot{\phi} + \mathbf{K}_{mu}^{\ddot{\phi}}\,\ddot{\phi} + \mathbf{K}_{mu}^{\dot{\phi}^2}\,\dot{\phi}^2 + \mathbf{K}_{d,sh,su}^{\dot{\omega}^x}\,\dot{\omega}^x + \mathbf{K}_{d,sh,su}^{\dot{\omega}^y}\,\dot{\omega}^y + \mathbf{K}_{d,sh,su}^{\dot{\omega}^z}\,\dot{\omega}^z \\ & + \mathbf{K}_{d,sh,su}^{\dot{\phi}\,\omega^y}\,\dot{\phi}\,\omega^y + \mathbf{K}_{d,sh,su}^{\omega^{x2}}\,\omega^{x2} + \mathbf{K}_{d,sh,su}^{\omega^{y2}}\,\omega^{y2} + \mathbf{K}_{d,sh,su}^{\omega^{z2}}\,\omega^{z2} + \mathbf{K}_{d,sh,su}^{\omega^x\,\omega^y}\,\omega^x\,\omega^y \\ & + \mathbf{K}_{d,sh,su}^{\omega^x\,\omega^z}\,\omega^x\,\omega^z + \mathbf{K}_{d,sh,su}^{\omega^y\,\omega^z}\,\omega^y\,\omega^z + \mathbf{K}_{mu,su}.\end{aligned} \tag{52}$$

The subscripts "d", "sh", "mu", "be" and "su" are associated respectively with the disk, the shaft, the mass unbalance, the bearing as well as the support and express the contribution to the phenomena represented by the corresponding matrix. The superscript "tr" refers to the translational effects of the disk mass center and the shaft geometric center, "ro" to the rotatory inertia, "cs" to the time-varying trigonometric functions (cosine and sine) associated with the mass unbalance, "g" to the rotor gyroscopic effect, "e" to the shaft elasticity corresponding to the different deformations and "sd" to the structural damping. The latter is an additional damping related to the axial and torsional degrees of freedom because the hydrodynamic journal bearings produce a damping linked only with the flexural degrees of freedom. The force vector $\mathbf{F}_r\,(t)$ included in Eq. (49) is defined as follows:

$$\mathbf{F}_r\,(t) = \mathbf{F}_{d,sh}^{W_r} + \mathbf{F}_{d,sh}^{\lambda}\,(t) + \mathbf{F}_{mu}\,(t) + \mathbf{F}_{mu,su}\,(t) + \mathbf{F}_{d,sh,su}\,(t)\,, \tag{53}$$

with

$$\mathbf{F}_{d,sh}^{W_r} = \mathbf{V}_{d,sh}^{W_r}\,W_r; \qquad \mathbf{F}_{d,sh}^{\lambda}\,(t) = -\mathbf{V}_{d,sh}^{\lambda}\,\ddot{\phi}, \tag{54}$$

$$\mathbf{F}_{mu}\,(t) = \mathbf{V}_{mu}^{\ddot{\phi}}\,\ddot{\phi} + \mathbf{V}_{mu}^{\dot{\phi}^2}\,\dot{\phi}^2; \qquad \mathbf{F}_{mu,su}\,(t) = f\,(\omega^x, \omega^y, \omega^z, x_O, y_O, z_O)\,, \tag{55}$$

$$\begin{aligned}\mathbf{F}_{d,sh,su}\,(t) = {} & -\mathbf{V}_{d,sh,su}^{u}\left(\ddot{x}_O + 2\,\dot{z}_O\,\omega^y - 2\,\dot{y}_O\,\omega^z + z_O\,(\dot{\omega}^y + \omega^x\,\omega^z) - y_O\,(\dot{\omega}^z - \omega^x\,\omega^y) - x_O\left(\omega^{y2} + \omega^{z2}\right)\right) \\ & - \mathbf{V}_{d,sh,su}^{v}\left(\ddot{y}_O - 2\,\dot{z}_O\,\omega^x + 2\,\dot{x}_O\,\omega^z - z_O\,(\dot{\omega}^x - \omega^y\,\omega^z) + x_O\,(\dot{\omega}^z + \omega^x\,\omega^y) - y_O\left(\omega^{x2} + \omega^{z2}\right)\right) \\ & - \mathbf{V}_{d,sh,su}^{w}\left(\ddot{z}_O + 2\,\dot{y}_O\,\omega^x - 2\,\dot{x}_O\,\omega^y + y_O\,(\dot{\omega}^x + \omega^y\,\omega^z) - x_O\,(\dot{\omega}^y - \omega^x\,\omega^z) - z_O\left(\omega^{x2} + \omega^{y2}\right)\right) \\ & - \mathbf{V}_{d,sh,su}^{y\,w}\,(\dot{\omega}^x + \omega^y\,\omega^z) + \mathbf{V}_{d,sh,su}^{y\,u}\,(\dot{\omega}^z - \omega^x\,\omega^y) + \mathbf{V}_{d,sh,su}^{y\,v}\left(\omega^{x2} + \omega^{z2}\right) - \mathbf{V}_{d,sh,su}^{\theta}\,(\dot{\omega}^x + \omega^y\,\omega^z) \\ & - \mathbf{V}_{d,sh,su}^{\lambda}\,\dot{\omega}^y - \mathbf{V}_{d,sh,su}^{\psi}\,(\dot{\omega}^z - \omega^x\,\omega^y) - \mathbf{V}_{d,sh,su}^{y\,\psi}\left(\dot{\phi}\,\omega^x + \omega^x\,\omega^y\right) + \mathbf{V}_{d,sh,su}^{y\,\theta}\left(\dot{\phi}\,\omega^z + \omega^y\,\omega^z\right),\end{aligned} \tag{56}$$

where the load vectors $\mathbf{F}_{mu}$, $\mathbf{F}_{d,sh,su}$ and $\mathbf{F}_{mu,su}$ stand for the mass unbalance, the inertia force due to support motions and that due to coupling between both phenomena. The superscripts u, v, w, θ, λ and ψ signify the direction of the action force components linked with the support motions. Lastly, the superscripts "$\ddot{\phi}$" and "$\dot{\phi}^2$" denote the components of the mass unbalance forces expressed in terms of the time derivatives of the trigonometric functions $\cos\phi$ and $\sin\phi$.

5.2. Prediction of the stability

Employing the Floquet theory [6,7,37,38] leads to the evaluation of the dynamic behavior stability of the on-board rotor subject to periodic parametric excitations. In other words, by calculating the so-called "Floquet transition matrix" (or monodromy matrix) of the system during one period τ_{pe} of the parametric excitation and by determining its eigenvalues, the zones of instability can be identified. First, the utilization of the Floquet theory needs a differential system represented in the state-space form. Namely, the linear second-order differential equations (i.e., Eq. (49)) of the rotor should be transformed into a first-order system as follows:

$$\dot{\mathbf{X}}_r = \mathbf{A}_r \mathbf{X}_r + \mathbf{B}_r, \tag{57}$$

with

$$\mathbf{X}_r = \begin{Bmatrix} \boldsymbol{\delta}_r \\ \dot{\boldsymbol{\delta}}_r \end{Bmatrix}; \qquad \mathbf{A}_r = \begin{bmatrix} \mathbf{0} & \mathbf{I} \\ -\mathbf{M}_r^{-1}\mathbf{K}_r & -\mathbf{M}_r^{-1}\mathbf{C}_r \end{bmatrix}; \qquad \mathbf{B}_r = \begin{Bmatrix} \mathbf{0} \\ \mathbf{M}_r^{-1}\left(\mathbf{F}_r(t) + \mathbf{F}_{be}\left(\boldsymbol{\delta}_r^0, \mathbf{0}\right) + \mathbf{K}_{be}\boldsymbol{\delta}_r^0\right) \end{Bmatrix}. \tag{58}$$

The state-space vector $\mathbf{X}_r$ is of dimensions $2n_g \times 1$ where n_g is the total number of degrees of freedom of Eq. (49). Then, the monodromy matrix $\boldsymbol{\Psi}_r(t = \tau_{pe})$ is described by the following:

$$\frac{\partial \mathbf{X}_r(t = \tau_{pe})}{\partial \mathbf{X}_r(0)} = \boldsymbol{\Psi}_r(t = \tau_{pe}) = \begin{bmatrix} \boldsymbol{\Phi}_r(t = \tau_{pe}) \\ \dot{\boldsymbol{\Phi}}_r(t = \tau_{pe}) \end{bmatrix}; \qquad \text{with} \qquad \boldsymbol{\Phi}_r = \frac{\partial \boldsymbol{\delta}_r}{\partial \mathbf{X}_r(0)}. \tag{59}$$

Creating the matrices $\boldsymbol{\Phi}_r$ and $\dot{\boldsymbol{\Phi}}_r$ necessary to compute the monodromy matrix may be made by the differentiation of the equations of motion of the rotor with respect to initial condition vector $\mathbf{X}_r(0)$, then

$$\mathbf{M}_r(t)\,\ddot{\boldsymbol{\Phi}}_r + \mathbf{C}_r(t)\,\dot{\boldsymbol{\Phi}}_r + \mathbf{K}_r(t)\,\boldsymbol{\Phi}_r = \mathbf{0}. \tag{60}$$

The above equation represents a system of homogeneous linear differential equations, i.e., only the linear equations of motion with no external forces are exploited in the Floquet theory. In order to obtain the matrices $\boldsymbol{\Phi}_r(\tau_{pe})$, $\dot{\boldsymbol{\Phi}}_r(\tau_{pe})$ of dimensions $n_g \times 2n_g$ and thereby the monodromy matrix $\boldsymbol{\Psi}_r(t = \tau_{pe})$, a numerical time integration method is applied over one period τ_{pe} of the parametric excitation with the following initial conditions at time $t = 0$:

$$\boldsymbol{\Phi}_r(0) = \frac{\partial \boldsymbol{\delta}_r(0)}{\partial \mathbf{X}_r(0)} = \begin{bmatrix} \dfrac{\partial \boldsymbol{\delta}_r(0)}{\partial \boldsymbol{\delta}_r(0)} & \dfrac{\partial \boldsymbol{\delta}_r(0)}{\partial \dot{\boldsymbol{\delta}}_r(0)} \end{bmatrix} = \begin{bmatrix} \mathbf{I} & \mathbf{0} \end{bmatrix} \quad \text{and} \quad \dot{\boldsymbol{\Phi}}_r(0) = \frac{\partial \dot{\boldsymbol{\delta}}_r(0)}{\partial \mathbf{X}_r(0)} = \begin{bmatrix} \dfrac{\partial \dot{\boldsymbol{\delta}}_r(0)}{\partial \boldsymbol{\delta}_r(0)} & \dfrac{\partial \dot{\boldsymbol{\delta}}_r(0)}{\partial \dot{\boldsymbol{\delta}}_r(0)} \end{bmatrix} = \begin{bmatrix} \mathbf{0} & \mathbf{I} \end{bmatrix}. \tag{61}$$

As reported in [39], the monodromy matrix can be very efficiently computed using the linear version of the Newmark time-step integration algorithm. The calculation over one period is accurate in the case of a parametric excitation which consists of a single frequency. Nevertheless, this calculation is more complicated in the case of several parametric excitation frequencies especially when one of them cannot be a multiple of the others because it seems difficult to discover the periodicity of the overall excitation, i.e., it is difficult to find the greatest common factor of the excitation frequencies. As an illustration, a two-frequency parametric excitation can without a doubt be analyzed. Also, the principle must be extended to three or more frequencies. In the case of a signal composed of a linear combination of two frequencies f_1 and f_2, a periodicity exists certainly when the latters are commensurable, i.e., when the ratio of the smallest frequency to the other is a rational number $\frac{n_1}{n_2}$ where n_1 and n_2 are respectively the smallest possible integer numerator and denominator. The inverse of the greatest common factor of two integer frequencies provides the smallest period of the signal. For a more general case, the latter represents the ratio of the numerator n_1 to the smallest frequency and that of the denominator n_2 to the biggest frequency, i.e., $\tau_{pe} = \frac{n_1}{f_1} = \frac{n_2}{f_2}$. In order to exclude any complication in the construction of the stability charts, integer frequencies of the parametric excitations are used to adopt a constant basic period $\tau_{pe} = 1$ s. Even if this period is not always the smallest one, it can be easily executed for the Floquet theory and it accounts for the presence of any linear combinations of the two integer frequencies which appear, for instance, in the case of combined sinusoidal rotations of the support. Finally, the criterion stipulates that the static equilibrium point of the linear system is asymptotically stable if the greatest Floquet exponent (i.e., the natural logarithm of the greatest modulus of the monodromy matrix eigenvalues) is less than or equal to zero, while it is unstable if this exponent is greater than zero.

5.3. *Validation of the proposed on-board rotor model*

When the mass unbalance does not exist, the linear/nonlinear equations of motion of the on-board rotor demonstrate that only the rotational motions of the support have a parametric influence on them, while its translational motions have only an influence on the external force vectors (see, for example, [11,14–17]). In this section, the homogeneous linearized equations of motion are taken into consideration (see Eq. (49)) and the stability of the static equilibrium position for the on-board rotor is examined through the Floquet theory. The instability comes from the parametric excitation due to sinusoidal rotations of the rotor support around the Ox axis expressed by the angular velocity $\omega^x = \omega^{x,a} \cos \Omega^x t$ in rad/s (i.e., the corresponding angular displacement is $\beta = \beta^a \sin \Omega^x t = \frac{\omega^{x,a}}{\Omega^x} \sin \Omega^x t$ in rad). For a constant speed of rotation $\dot{\phi} = \Omega$, two factors affect the parametric excitations generated in a symmetric rotor: the amplitude $\omega^{x,a}$ of the support rotation and its frequency Ω^x. Therefore the stability analysis covers these two parameters and utilizes $\tau_{pe} = \frac{2\pi}{2\Omega^x} = \frac{\pi}{\Omega^x}$ (Ω^x in rad/s) as the period of the parametric excitation. This period corresponds to $\omega^{x2} = \frac{(\omega^{x,a})^2}{2} (1 + \cos 2\,\Omega^x t)$ when only the bending degrees of freedom are considered in the on-board rotor model, see Eqs. (52) and (A.4).

For validation purposes, a comparison with a stability chart of a symmetric on-board rotor (with one disk) obtained by Dakel et al. [17] and investigated in the presence of the linearized hydrodynamic short bearings is introduced in Fig. 6(a) and (b). The speed of rotation of the rotor is $\Omega = 1200$ rpm and the frequency of the support rotation is contained in the range of interest $\Omega^x \in [0;\ 2000\ \text{Hz}]$. In addition, the calculations are performed with $\Delta\Omega^x = 10$ Hz and $\Delta\left(\frac{\omega^{x,a}}{\Omega^x}\right) = 0.0167$ rad in Fig. 6(a), while with $\Delta\Omega^x = 1$ Hz and $\Delta\left(\frac{\omega^{x,a}}{\Omega^x}\right) = 0.05$ rad in Fig. 6(b). It is noted that the size of the instability zones increases for increasing values of the amplitude $\frac{\omega^{x,a}}{\Omega^x}$ of the support angular displacement and there is a wide region of instability because of the anisotropic components of the damping and stiffness matrices in the hydrodynamic journal bearings. Moreover, no deviation can be observable in Fig. 6(a) and (b) for the case of flexural degrees of freedom. In conclusion, the finite element on-board rotor model originally based on six degrees of freedom and developed in the current research is validated regarding the model developed in [17]. The proposed model can also be validated against some results of Han and Chu [20]. Fig. 7 depicts the stability charts of an on-board rotor built by Duchemin et al. [11] and adopted in [20]. The rotor runs at a speed of rotation $\Omega = 250$ rad/s and is subject to pitch sinusoidal rotations $\omega^x = -\omega^{x,a} \sin \Omega^x t$ of the support in the presence of two values of damping coefficient ($\xi^d = 0$ and 5×10^{-5}) defining a damping proportional to the stiffness matrix of the shaft. The results of Fig. 7 are mostly similar to those seen in [20]. The modest differences between the results may arise from the use of Timoshenko beam finite elements in this research, while the Euler beam theory is employed in [20].

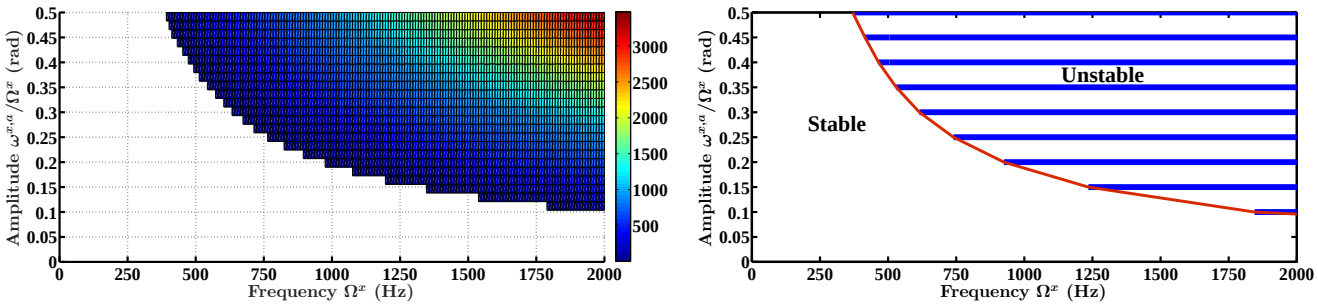

(a) (b)

Fig. 6. Comparison of stability charts obtained by: (a) the proposed on-board rotor model, and (b) Dakel et al. [17].

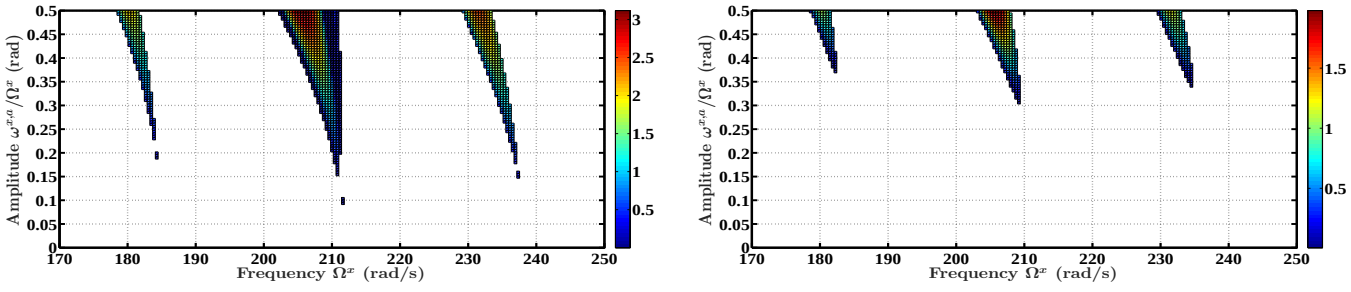

(a) (b)

Fig. 7. Stability charts obtained in the case of pitch rotations of the support and two values of damping coefficient: ξ^d = (a) 0, (b) 5×10^{-5} for the validation of the proposed on-board rotor model against some results of Han and Chu [20].

6. Numerical applications and interpretation of results

6.1. Presentation of an on-board rotor-bearing system with three disks

The investigated symmetric on-board rotor-hydrodynamic bearing system is presented in Fig. 8. It is composed of a symmetric slender flexible shaft and three identical symmetric rigid disks as well as two identical finite-length bearings. The flexible shaft of constant circular cross-sectional area is modeled with 12 two-node Timoshenko beam finite elements. The six degrees of freedom of each node are $(u, v, w, \theta, \lambda, \psi)$ where (u, w) are the two lateral translations due to bending along the Ox and Oz axes respectively, (θ, ψ) are the corresponding rotations around the Ox and Oz directions, v is the axial translation along the Oy axis and λ is the torsional angle around the Oy axis. Thus the total number of degrees of freedom is $n_g = 78$. The rigid disks 1, 2 and 3 are located at nodes 6, 8, 10 and the mass unbalance is placed on the disks of nodes 6 and 10. The hydrodynamic finite-length bearings #1 and #2 are located at nodes 4 and 12 respectively. The material characteristics and geometric properties of the rotor and the bearings are listed in Tables 1 and 2. The origin O of the frame of reference connected to the rotor rigid support R coincides with the shaft end-point positioned at the left-hand side, while the origin O^g of the Galilean frame of reference R^g (i.e., the center of rotation of the support) coincides with the center of the bearing #1.

Since the hydrodynamic journal bearings provide a damping matrix concerning only the bending degrees of freedom, an additional damping linked with the axial and torsional degrees of freedom is employed through the structural damping matrix (Rayleigh damping) defined by $\mathbf{C}_{sh}^{sd} = c^v \mathbf{K}_{sh}^v + c^\lambda \mathbf{K}_{sh}^\lambda$ where $c^v = 1 \times 10^{-5}$, $c^\lambda = 1 \times 10^{-4}$ are constant coefficients, $\mathbf{K}_{sh}^v$ and $\mathbf{K}_{sh}^\lambda$ are respectively the parts of the stiffness matrix $\mathbf{K}_{sh}^e$ due to the shaft elasticity corresponding to the degrees of freedom v and λ. This additional matrix does not modify the original dynamic behavior of the rotor and prevents any round-off error which can occur in the dynamic analysis if the axial and torsional degrees of freedom are not damped. Furthermore, a coupling placed at node 2 is taken into consideration to simulate the connection between the motor and the shaft. Its properties are given in Table 3.

The investigated rotor runs at a constant speed of rotation $\dot{\phi} = \Omega$ for the majority of results presented in what follows and is subject to sinusoidal rotational motions (simple or combined rotations) of the rigid support or to mass unbalance excitation combined with sinusoidal translational motions of the support. The combined excitations are considered as multi-frequency parametric excitations. For a given speed of rotation, the coordinates of the static equilibrium position C_{be}^0 of the shaft geometric center in the fluid film bearings created by the rotor weight are calculated and the corresponding damping and stiffness matrices $\mathbf{c}_{be}$, $\mathbf{k}_{be}$ are determined by applying the finite difference method (i.e., numerical procedure), which is considered as a reference one, to solve the Reynolds equation because there are no reliable analytical formulations for the hydrodynamic finite-length bearings.

Owing to the complexity of the motion of an on-board rotor-bearing system, the first step of its dynamic analysis is to evaluate the stability of the static equilibrium position for a given set of parameters. Thus the obtained results are mainly represented by stability charts. The latters provide information about the greatest Floquet exponent computed with the so-called "monodromy matrix" as a function of the parametric excitation frequencies. The system under study is stable and there is no dot in the stability chart if the greatest Floquet exponent is negative, while

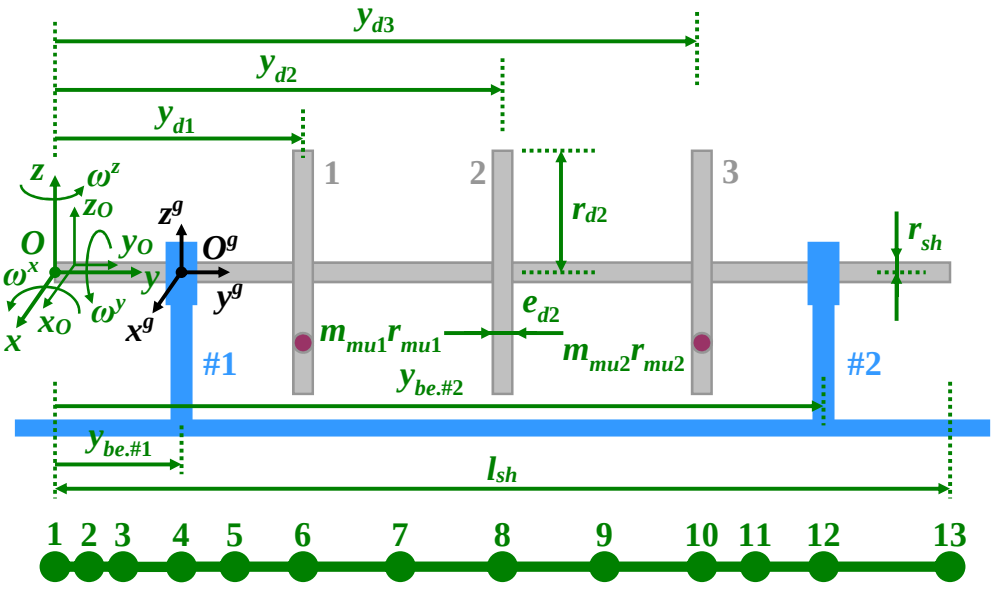

Fig. 8. Symmetric on-board flexible rotor system with hydrodynamic finite-length bearings.

Material density of the disks	$\rho_{d1} = \rho_{d2} = \rho_{d3} = 7778$ kg/m^3
Radius of the disks	$r_{d1} = r_{d2} = r_{d3} = 0.063$ m
Thickness of the disks	$e_{d1} = e_{d2} = e_{d3} = 0.0156$ m
Location of the disks	$y_{d1} = 0.209$ m, $y_{d2} = 0.432$ m, $y_{d3} = 0.655$ m
Material density of the shaft	$\rho_{sh} = 7778$ kg/m^3
Radius of the shaft	$r_{sh} = 6.35 \times 10^{-3}$ m
Length of the shaft	$l_{sh} = 0.851$ m
Young's modulus of the shaft	$E_{sh} = 2.1 \times 10^{11}$ N/m^2
Poisson's ratio of the shaft	$\nu = 0.3$
Shear correction factor of the shaft	$\kappa^x_{sh} = \kappa^z_{sh} = 0.9252$ [40]

Table 1. Essential characteristics of the symmetric flexible rotor.

Radius of the bearings	$r_{be.\#1} = r_{be.\#2} = 6.3925 \times 10^{-3}$ m
Length of the bearings	$l_{be.\#1} = l_{be.\#2} = 0.0224$ m
Locations of the bearings	$y_{be.\#1} = 0.07$ m, $y_{be.\#2} = 0.796$ m
Radial clearance of the bearings	$c_{be.\#1} = c_{be.\#2} = 4.25 \times 10^{-5}$ m
Oil film dynamic viscosity	$\mu_{be.\#1} = \mu_{be.\#2} = 0.01$ Pa s

Table 2. Essential properties of the hydrodynamic finite-length bearings.

Damping coefficients	Values	Stiffness coefficients	Values
c^{uu}_{co}	2.91 N s/m	k^{uu}_{co}	30832 N/m
c^{vv}_{co}	17.02 N s/m	k^{vv}_{co}	11147 N/m
c^{ww}_{co}	2.91 N s/m	k^{ww}_{co}	30832 N/m
$c^{\theta\theta}_{co}$	5.7×10^{-4} N m s/rad	$k^{\theta\theta}_{co}$	2.36 N m/rad
$c^{\lambda\lambda}_{co}$	1×10^{3} N m s/rad	$k^{\lambda\lambda}_{co}$	84.9 N m/rad
$c^{\psi\psi}_{co}$	5.7×10^{-4} N m s/rad	$k^{\psi\psi}_{co}$	2.36 N m/rad

Table 3. Measured characteristics of the coupling between the motor and the rotor.

it is unstable if this exponent has a positive value. In this case, a dot indicating the value of the Floquet exponent (i.e., the instability intensity) is placed in the stability chart. The parametric excitation frequencies are chosen to be included in the range of interest [0; 200 Hz] with a frequency increment of 1 Hz. In the presence of multi-frequency parametric excitations, the period τ_{pe} for the Newmark integration scheme is chosen to be equal to 1 s (for the reason mentionned in Section 5.2) and the time step is set to be $\Delta t = 1 \times 10^{-4}$ s which represents a sufficiently tiny value in order to account for the linear combinations existing in such a case, while τ_{pe} is equal to the inverse of the excitation frequency and $\Delta t = \frac{\tau_{pe}}{50}$ s in the presence of single-frequency parametric excitations. It is reminded that the stability analysis does not require any external forces in the equations of motion.

6.2. Natural frequencies of the rotor-hydrodynamic bearing for a fixed support

The natural frequencies f_r of the rotor without support motions depend on the speed of rotation Ω and can be deduced from a preliminary modal analysis (linear complex eigenvalue analysis). They are represented by the Campbell diagram plotted in Fig. 9. The latter illustrates the critical speeds of rotation obtained by the intersection of the straight line $f = \frac{\Omega}{60}$ (Ω in rpm), which characterizes the mass unbalance frequency, with the natural frequencies f_r of the rotor. The first ten modes are reported in Table 4 for a speed of rotation $\Omega = 1200$ rpm which is employed for the majority of next figures. Mode 1 is an axial mode shape (the shaft remains rigid) with a very low frequency due to the flexibility along the Oy axis provided by the coupling between the motor and the shaft. Modes 2, 5 and 8 are the first three backward whirl (BW) bending modes. Modes 3, 6 and 9 are the first three forward whirl (FW) bending modes. Mode 4 is a torsion mode composed of mixed suspension and deformed motions since the stiffness provided by the coupling is of the same order of magnitude as the structural torsional stiffness of the shaft. Modes 7 and 10 are the second and third torsion modes without rigid body component. This spectral content is very useful in order to interpret finely the results of the dynamic stability analysis. Lastly, it should be mentioned that owing to the presence of hydrodynamic bearings, the rotor can become unstable when it runs at a speed of rotation greater than $\Omega = 1940$ rpm, i.e., the behavior stability of the on-board rotor is to be examined for speeds of rotation smaller than

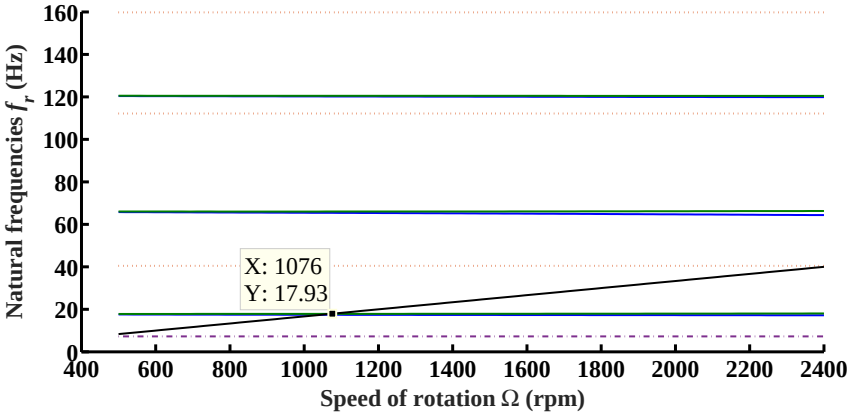

Fig. 9. Campbell diagram for the first ten natural frequencies of the rotor-hydrodynamic bearing system in the case of a fixed support (dashed-dotted, solid and dotted lines denote axial, bending and torsion modes respectively).

Mode	Category	Natural frequency f_r (Hz)
1	Axial f_r^{a1}	7.27
2	Flexural f_r^{Bb1}	17.39
3	Flexural f_r^{Fb1}	17.87
4	Torsional f_r^{t1}	40.45
5	Flexural f_r^{Bb2}	65.33
6	Flexural f_r^{Fb2}	66.04
7	Torsional f_r^{t2}	112.19
8	Flexural f_r^{Bb3}	120.17
9	Flexural f_r^{Fb3}	120.51
10	Torsional f_r^{t3}	159.78

Table 4. First ten modes and natural frequencies of the rotor-bearing system running at a speed of rotation $\Omega = 1200$ rpm for a fixed support (B and F stand for backward and forward whirl modes).

this value in order to evaluate the instability produced purely by support excitations.

6.3. Instability due to simple sinusoidal rotation of the support

6.3.1. Influence of the types of degrees of freedom considered in the on-board rotor model

In the presence of a simple sinusoidal rotation of the rigid support around the $O^g x$ axis (pitch rotation) given by the angular velocity $\omega^x = -\omega^{x,a} \sin \Omega^x t$ in rad/s (i.e., the corresponding angular displacement is $\beta = \beta^a \cos \Omega^x t = \frac{\omega^{x,a}}{\Omega^x} \cos \Omega^x t$ in rad), a single-frequency parametric excitation is created. This type of excitation can lead to dynamic instability as stated previously. The two variables for the stabilty analysis are the amplitude $\omega^{x,a}$ and the frequency ^{x} of the parametric excitation. Fig. 10 introduces a comparison between four stability charts of the on-board rotor running at a constant speed of rotation $\Omega = 1200$ rpm and modeled by taking into account four different sets of degrees of freedom. The instability frequency f_{ins} (in Hz) to be used in what follows for seeking the unstable modes is described by $f_{ins} = \Omega^x \simeq \frac{f_r^i \pm f_r^j}{k}$ (already reported by Hsu [8]) where Ω^x (in Hz) is the support rotation frequency, f_r^i as well as f_r^j (in Hz) are the i-th and j-th natural frequencies of the rotor and the positive integer k is the order of the instability. Three narrow tongues of instability corresponding to 17.09 Hz, 63.32 Hz and 119.6 Hz are observed in Fig. 10(a). This is actually the instabilities of the first three bending modes f_r^{b1}, f_r^{b2} and f_r^{b3} (instability of order $k = 2$ because the instability frequency corresponds to $f_{ins} \simeq \frac{2 f_r^{bi}}{2}$) due to the presence of ω^{x2} in the w and ψ terms of the stiffness matrix $\mathbf{K}_{d,sh,su}^{\omega^{x2}}$ involved in Eq. (52) (for instance, see Eq. (A.4)). The damping matrix $\mathbf{C}_{d,sh,su}^{\omega^x}$ due to the support rotation has no influence because its components are nil since only the flexural degrees of freedom are considered. The anisotropic terms of the damping and stiffness matrices $\mathbf{C}_{be}$, $\mathbf{K}_{be}$ of the linearized hydrodynamic journal bearings lead to the large region of instability seen in Fig. 10(a). In Fig. 10(b), the flexural and torsional degrees of freedom are taken into consideration and the instability is the same as found in Fig. 10(a), i.e., the wide zone of instability and the lines of instability at 17.09 Hz, 63.32 Hz and 119.6 Hz do not change mostly. In addition, two new primary instabilities ($k = 1$) at 57.29 Hz and 129.6 Hz appear. They are due to the couplings between

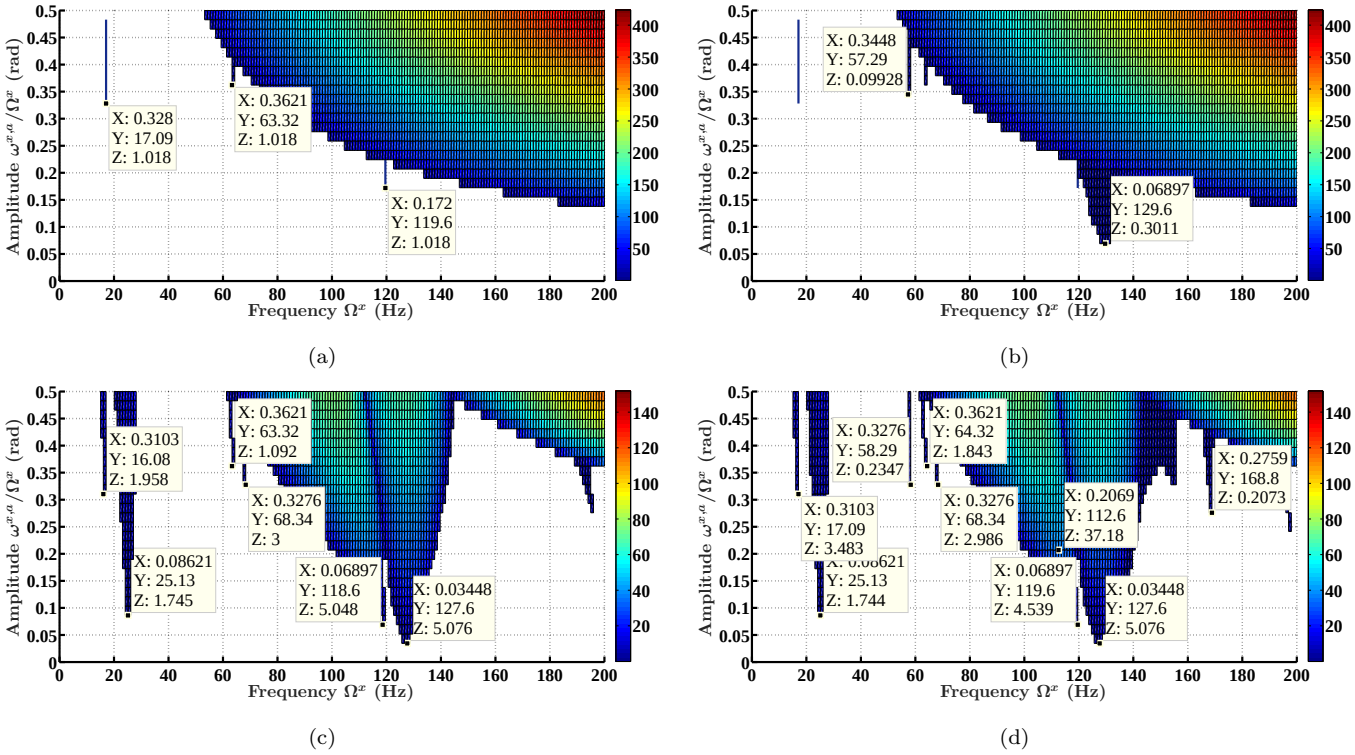

Fig. 10. Stability charts of the on-board rotor running at $\Omega = 1200$ rpm, excited by pitch rotations of the support and modeled with: (a) flexural degrees of freedom, (b) flexural and torsional degrees of freedom, (c) flexural and axial degrees of freedom, (d) flexural, axial and torsional degrees of freedom.

flexural and torsional degrees of freedom (i.e., $f_{ins} = 57.29\,\text{Hz} \simeq f_r^{b1} + f_r^{t1}$ and $f_{ins} = 129.6\,\text{Hz} \simeq f_r^{b1} + f_r^{t2}$) which come from the presence of $\dot{\omega}^x$ in the stiffness matrix $\mathbf{K}_r$ of the rotor (see Eq. (A.4)). Fig. 10(c) shows that taking into account the axial degrees of freedom modifies significantly the stability chart when compared to that presented in Fig. 10(a). The large region of instability is divided into smaller regions. This is explained by the contribution of the coupling between the motor and the shaft to the dynamic behavior of the on-board rotor-bearing system. The tongues corresponding to 16.08 Hz, 63.32 Hz and 118.6 Hz are due to the first three bending modes (see Table 4) and the order of the instability is $k = 2$. They are much wider and higher than those in Fig. 10(a) because of the new presence of $\dot{\omega}^x$ (in the stiffness matrix $\mathbf{K}_r$) which is related to the coupling between flexural and axial degrees of freedom and which provides parametric excitation amplitudes greater than those of ω^{x2} (see Eq. (A.4)) since v also responds, i.e., since the first axial mode is also excited. Furthermore, some new tongues of the instability zones appear. The tongue at 68.34 Hz is relevant to the instability of order $k = 2$ expressed by the above formulation and demonstrates the interaction between the first and third bending modes. On the other hand, the combination of the axial and bending modes is mostly recognized by means of the tongues at 25.13 Hz and 127.6 Hz, i.e., $f_{ins} = 25.13\,\text{Hz} \simeq f_r^{a1} + f_r^{b1}$ and $f_{ins} = 127.6\,\text{Hz} \simeq f_r^{a1} + f_r^{b3}$), see Table 4. When the six degrees of freedom expressing the flexural, axial and torsional motions are taken into consideration, all the tongues found in Fig. 10(b) and (c) are reproduced in Fig. 10(d), i.e., the tongues at the frequencies 17.09 Hz, 25.13 Hz, 58.29 Hz, 64.32 Hz, 68.34 Hz, 119.6 Hz and 127.6 Hz. In other words, the wide zone of instability seen in Fig. 10(a) is divided into narrower zones as mentioned previously and the stability chart has a wealth of different types of instability including the interaction either between the bending and axial modes or between the bending and torsion ones. A new narrow tongue of instability can be identified at the frequency 168.8 Hz which permits detecting the combination of the first axial mode and the third torsion one (i.e., $f_{ins} = 168.8\,\text{Hz} \simeq f_r^{a1} + f_r^{t3}$ and $k = 1$) although there is no direct coupling between the axial and torsional degrees of freedom in the parametric matrices (see Eqs. (A.3) and (A.4)).

6.3.2. Influence of the support rotation axis

Fig. 11 points out the stability charts when the rotor is excited by simple sinusoidal rotations of the support: the roll rotation around the $O^g y$ axis is given by the angular velocity $\omega^y = -\omega^{y,a} \sin \Omega^y t$ in rad/s (the corresponding angular displacement $\gamma = \gamma^a \cos \Omega^y t = \frac{\omega^{y,a}}{\Omega^y} \cos \Omega^y t$ in rad), while the yaw rotation around the $O^g z$ axis is expressed as $\omega^z = -\omega^{z,a} \sin \Omega^z t$ in rad/s (i.e., $\alpha = \alpha^a \cos \Omega^z t = \frac{\omega^{z,a}}{\Omega^z} \cos \Omega^z t$ in rad). In Fig. 11(a), the roll rotation creates instabilities only for large frequencies and amplitudes. The tongues of the instability zones correspond to 131.7 Hz and 137.7 Hz. They come from the couplings between the bending degrees of freedom (u, w) and (θ, ψ) in the stiffness

matrices related to $\dot{\omega}^y$ (see Eq. (A.4)). In Fig. 11(b), the yaw rotation provides regions of instability very similar to those obtained by the pitch rotation of the support and presented in Fig. 10(d). This is because the dynamic behavior of the rotor system is almost symmetric even with the resulting asymmetry of the behaviors of the hydrodynamic bearings and the coupling. Moreover, the little differences between Figs. 10(d) and 11(b) relevant to the tongues of the instability zones concern the type of whirl bending modes which can be easier to excite for support rotations around a certain axis but not around the other.

6.3.3. Influence of the solving method used for the hydrodynamic bearings

Fig. 12(a) presents the stability chart of the rotor excited by sinusoidal rotations of the support around the pitch axis and mounted on hydrodynamic bearings dealing with the finite difference method (i.e., Figs. 10(d) and 12(a) are the same), while in Fig. 12(b), the rotor is mounted on hydrodynamic bearings treated as short ones. Namely, an analytical study is performed in Fig. 12(b) to calculate the damping and stiffness matrices of the bearings (whose expressions can be found in [33]). The results in this figure are rather similar to those displayed in Fig. 12(a) except for some additional instabilities associated with the analytical analysis at 179.9 Hz and 184.9 Hz which can be seen in Fig. 11(b). This similarity is due to the fact that even if the error concerning the position of the shaft geometric center in the bearings (expressed by the eccentricity and the attitude angle) is relatively high when the analytical bearing model is considered, the damping and stiffness coefficients still have the same order of magnitude as computed by the finite difference method. Thus even with an error of 50% or more, the natural frequencies of the rotor, whose rigid support is fixed, are almost the same because the bearings always represent nodes of vibration and the transverse deflections of the shaft are slightly modified. This justifies the use of the analytical bearing model for the stability study.

6.3.4. Influence of the speed of rotation of the rotor

Fig. 13(a)–(d) depicts the stability charts of the on-board rotor running successively at speeds of rotation $\Omega =$ 500 rpm, 1000 rpm, 1500 rpm and 1900 rpm in the presence of pitch rotations of the support. This operating speed range permits getting sufficient restoring forces of the bearings and staying under the threshold of instability due to

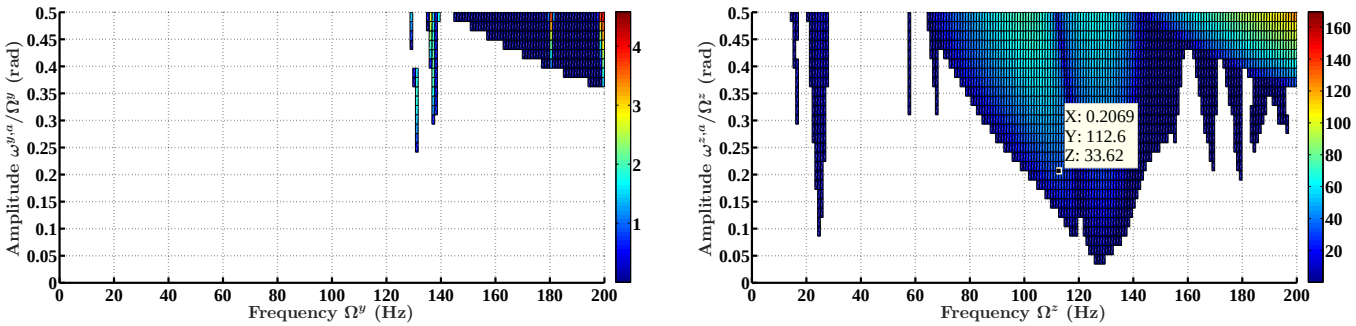

(a) (b)

Fig. 11. Stability charts of the rotor for support rotations around: (a) the roll axis, or (b) the yaw axis.

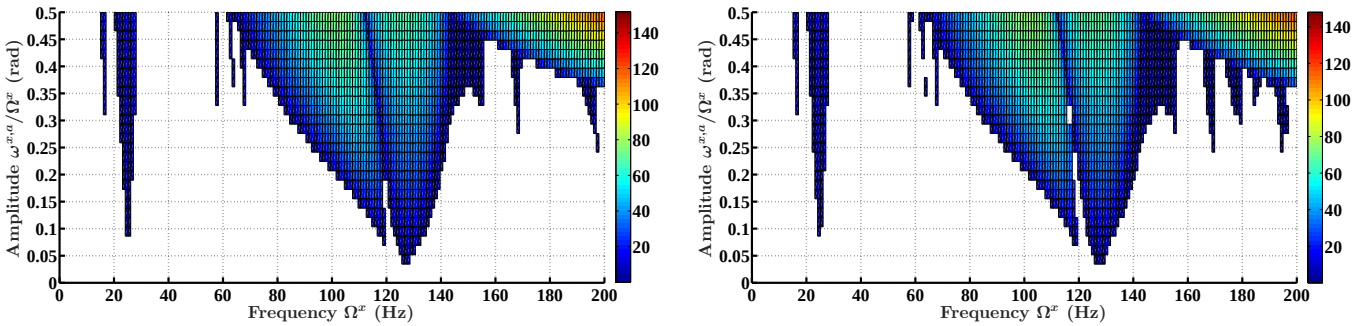

(a) (b)

Fig. 12. Stability charts of the rotor mounted on hydrodynamic journal bearings treated by (a) numerical and (b) analytical methods for support rotations around the pitch axis.

the fluid film bearings. It should be clarified that when the speed of rotation increases, the resulting zones of instability become greater because of the increasing contribution of the hydrodynamic bearings which lead to an unstable rotor for $\Omega = 1940$ rpm and a fixed support. Looking at the three stability charts highlighted in Figs. 10(d) as well as 13(a) and (d), a particular point corresponding to the amplitude $\frac{\omega^{x,a}}{\Omega^x} = 0.3276$ rad and to the frequency $\Omega^x = 194$ Hz of the support rotation is found to be unstable at $\Omega = 1200$ rpm but stable at $\Omega = 500$ rpm and 1900 rpm. This point will be used in the following simulation concerning the transient dynamic analysis.

6.3.5. Interest of the transient regime

Now, it seems legitimate to know what happens in the transient regime if the rotor runs at a time-varying speed of rotation $\dot{\phi}(t)$. In this paper, the law of the speed of rotation is assumed to be a linear function of time and varies from 500 rpm to 1900 rpm. In addition, the transient time integration of the linearized equations of motion with no external forces except for the rotor weight is performed. Fig. 14(a) exhibits the associated time history response of the rotor-bearing system at node 13 computed with the Newmark integration scheme for non-zero initial conditions. According to Fig. 14(b), the displacement tends to increase at the instant $t = 10$ s (corresponding to $\dot{\phi} = 1200$ rpm) and the rotor can become unstable. Then the displacement tends to decrease at $t = 16$ s (corresponding to $\dot{\phi} = 1725$ rpm) and the rotor can be stable, see Fig. 14(a). By means of the previous observation, it is concluded

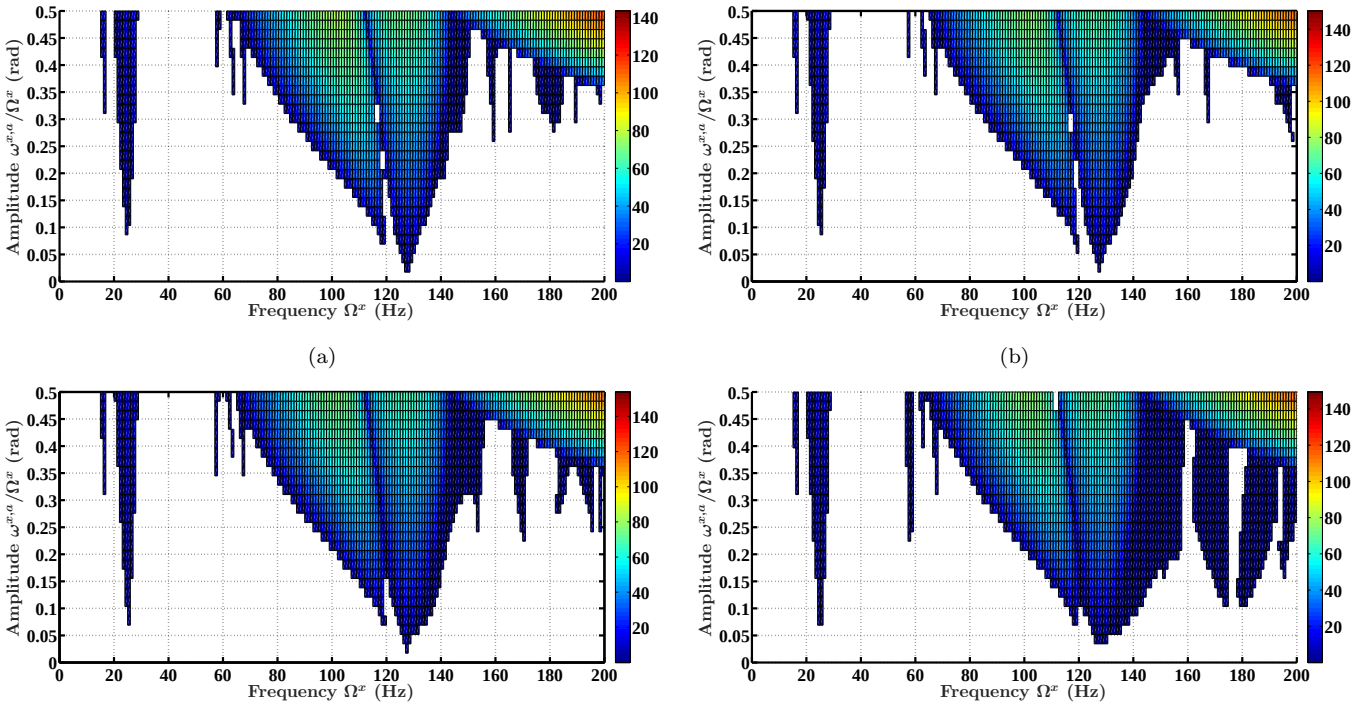

Fig. 13. Stability charts of the rotor subject to support rotations around the pitch axis and running at four values of speed of rotation: $\Omega =$ (a) 500 rpm, (b) 1000 rpm, (c) 1500 rpm, (d) 1900 rpm.

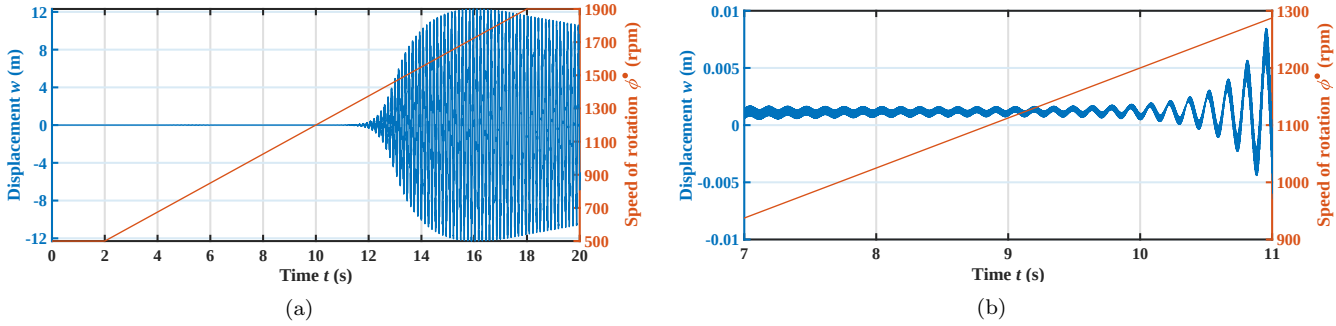

Fig. 14. (a) Transient response of the rotor running at a time-varying speed of rotation and excited by a pitch sinusoidal rotation of the support: $\omega^x = -\omega^{x,a} \sin \Omega^x t$ with $\Omega^x = 194$ Hz. (b) Zoom on the transient response for the time interval $t \in [7; 11$ s$]$.

that the transient dynamic analysis of the on-board rotor for a non-stationary speed of rotation and given frequency and amplitude of the support motion permits one to predict the behavior stability without employing the Floquet theory for each speed of rotation of the rotor contained in the interval $\dot{\phi} = \Omega \in [500;\ 1900\ \text{rpm}]$ because this procedure may necessitate a huge computational time when compared to the transient analysis. However, a new calculation of the damping and stiffness matrices of the hydrodynamic bearings is required for each speed of rotation of the rotor whatever the considered strategy because these matrices depend on the static equilibrium position of the shaft center within the bearings which is a function of the speed of rotation.

6.4. Instability due to two combined sinusoidal rotations of the support

When the rotor is subject to multi-frequency excitations such as combined sinusoidal rotations of the support around two different directions, the parametric excitations become more important than the single-frequency ones and can make the stability charts more complicated by increasing the instability zones. Since the parametric excitations are periodic, the dynamic stability is predicted by employing the Floquet theory. In order to make the latter applicable to this type of excitations, integer frequencies can be used to keep a common period τ_{pe} of 1 s which will be used for the Newmark time integration algorithm. In other words, this period may not be the smallest but it always will be common for any linear combination of integer frequencies of the parametric excitations. Nevertheless, the associated computational time can be huge, this motivates the use of a modal reduction technique as developed in [41]. Eqs. (49)–(52) demonstrate that the position of the center of rotation of the support has no influence on the stable and unstable regions. The stability charts of the on-board rotor excited by two combined rotations of the support around the pitch and yaw axes are shown in Fig. 15. The support rotations are given by the angular displacements $\beta = \beta^a \cos\Omega^x t$ and $\alpha = \alpha^a \cos\Omega^z t$ with $\beta^a = \alpha^a = 0.05$ rad, 0.1 rad, 0.2 rad. In this case, the frequencies Ω^x and Ω^z are used as the two parameters for the stability analysis. For increasing values of the support rotation amplitudes, it is demonstrated that the influence of the multi-frequency excitations on the instability regions no longer remains perfectly horizontal or vertical especially at the intersections of the regions, which tend to become larger than expected. Furthermore, the highest intensities of the instability at $\beta^a = \alpha^a = 0.2$ rad in Figs. 10(d) and 11(b) are equal to 37.18 and 33.62 for $\Omega^x = \Omega^z = 112.6$ Hz, while the highest intensity in Fig. 15(c) is 41.46 for almost the same amplitudes and frequencies. Since the greatest modulus $e^{41.46}$ of the monodromy matrix eigenvalues is much greater than the sum $e^{37.18} + e^{33.62}$ corresponding to two single-frequency parametric excitations (two simple rotations), it can be deduced that if the multi-frequency parametric excitations are applied, the associated instability is more significant. This highlights the importance of consideration of combined support motions. On the other hand, several diagonal zones of instability characterized by linear functions between Ω^x and Ω^z (such as $\Omega^x = -\Omega^z + b$, $\Omega^x = \Omega^z + b$, $\Omega^x = 2\Omega^z + b$ or $\Omega^x = \frac{1}{2}\Omega^z + b$ where b is the vertical intercept) are observed, see Fig. 15(c). These diagonal instabilities reflect well the multi-frequency character of the parametric excitations. From all these results, it is well understood that a multi-frequency stability chart cannot be obtained by superimposing simply single-frequency ones obtained separately for each type of support rotations. Lastly, a zoom is needed for more details and information about the diagonal instabilities.

Fig. 16 presents a zoom on a diagonal instability in Fig. 15(c) described by the linear function $\Omega^x = -\Omega^z + b$ for the ranges of interest $\Omega^x \in [0;\ 30\ \text{Hz}]$ and $\Omega^z \in [0;\ 30\ \text{Hz}]$. At first sight, this diagonal instability seems to start from the instability due to the coupling between the first axial and bending modes at the frequency $25.13\ \text{Hz} \simeq f_r^{a1} + f_r^{b1}$ Hz as stated in Section 6.3 and seen in Fig. 10(d). Depending on the stiffness matrix $\mathbf{K}_r$ of the rotor involved in

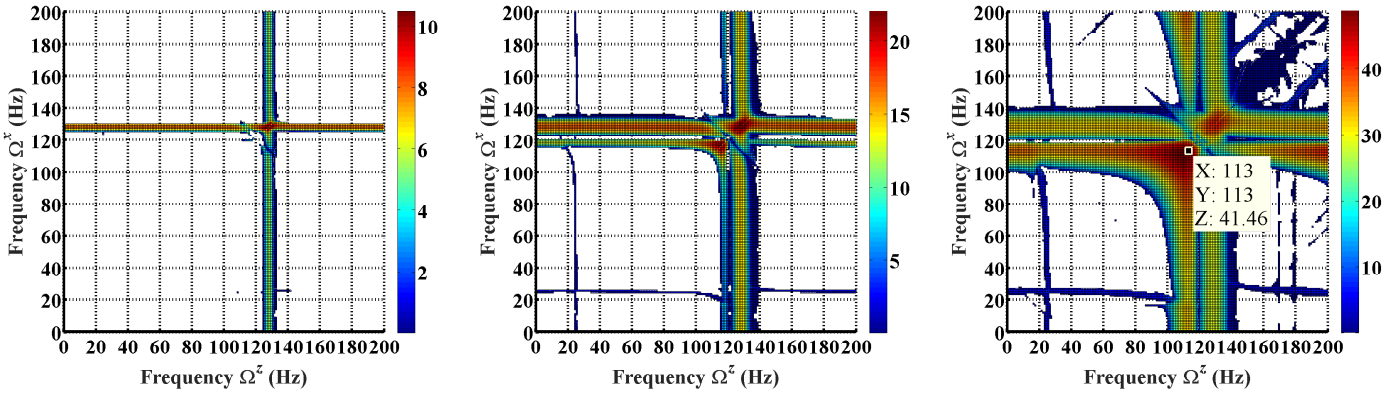

Fig. 15. Stability charts of the rotor excited by combined sinusoidal rotations of the support around the pitch and yaw axes: $\beta = \beta^a \cos\Omega^x t$ and $\alpha = \alpha^a \cos\Omega^z t$ with $\beta^a = \alpha^a =$ (a) 0.05 rad, (b) 0.1 rad, (c) 0.2 rad.

Eq. (52) (for example, see Eq. (A.4)), the understanding of the origin of different instabilities can be achieved. The $\omega^x\,\omega^z$ terms are very small to be responsible for these instabilities as seen with the quadratic term ω^{x2} which gives the results in Fig. 10(a). The main horizontal or vertical zones of instability are generated by the $\dot{\omega}^x$ and $\dot{\omega}^z$ terms as in the case of single-frequency excitations, see Figs. 10(d) and 11(b). With regard to the diagonal instability, it comes actually from the $\dot{\omega}^y$ term which couples the degrees of freedom u and w. Indeed, the angular velocity ω^y of the support is expressed as $\omega^y = \dot{\alpha}\sin\beta$ (see Eq. (6)). As a consequence, there are instability frequencies f_{ins} (in Hz) defined by the relationship $f_{ins} = |\Omega^z \pm (2q+1)\,\Omega^x| \simeq \frac{f_r^i \pm f_r^j}{k}$ where f_r^i as well as f_r^j (in Hz) are the i-th and j-th natural frequencies of the rotor, the positive integer k is the order of the instability, q is a non-negative integer, Ω^z comes from $\dot{\alpha}$ and $(2q+1)\,\Omega^x$ comes from $\sin\beta$. For instance, in the case where $q = 0$, an instability corresponding to the first bending mode f_r^{b1} can be obtained by the sum of the frequencies Ω^x and Ω^z of the support rotations, i.e., $f_{ins} = |15.2 + 20.2| = 35.4$ Hz $\simeq 2f_r^{b1}$ (the order of the instability $k = 1$). Thus the diagonal instability concerns only the first bending mode and can be found for all the frequencies produced by the sum $\Omega^x + \Omega^z$ such that the instability frequencies $f_{ins} \simeq \frac{2f_r^{b1}}{1}$ are obtained. Namely, this diagonal instability is not the extension of the instability due to the coupling between the first axial and bending modes at 25.13 Hz, this explains why the intersection between the diagonal instability and the vertical instability at 25.13 Hz is composed of several stripes. The other diagonal instabilities of Fig. 15(c), such as $\Omega^x = \Omega^z + b$, $\Omega^x = 2\Omega^z + b$ or $\Omega^x = \frac{1}{2}\Omega^z + b$, can also be explained in a similar way.

Fig. 17 highlights the stability charts of the on-board rotor obtained for combined sinusoidal rotational motions of the support around the pitch and roll axes, i.e., the angular displacements are $\beta = \beta^a \cos\Omega^x t$ and $\gamma = \gamma^a \cos\Omega^y t$ with $\beta^a = \gamma^a = 0.05$ rad, 0.1 rad, 0.2 rad. Unlike the results presented in Fig. 15, the influence of multi-frequency excitations is very low this time because the instability zones corresponding to the roll rotations of the support are much smaller than those due to the rotations around the pitch axis (as can be observed in Section 6.3) even with an amplitude of 0.2 rad for each rotation.

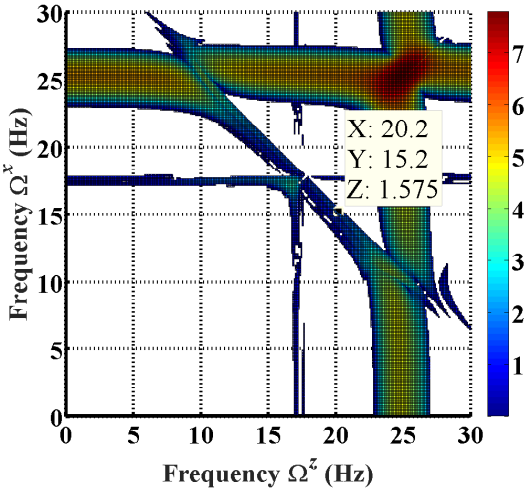

Fig. 16. Zoom on the stability chart in Fig. 15(c) for the ranges of interest $\Omega^x \in [0;\ 30\text{ Hz}]$ and $\Omega^z \in [0;\ 30\text{ Hz}]$.

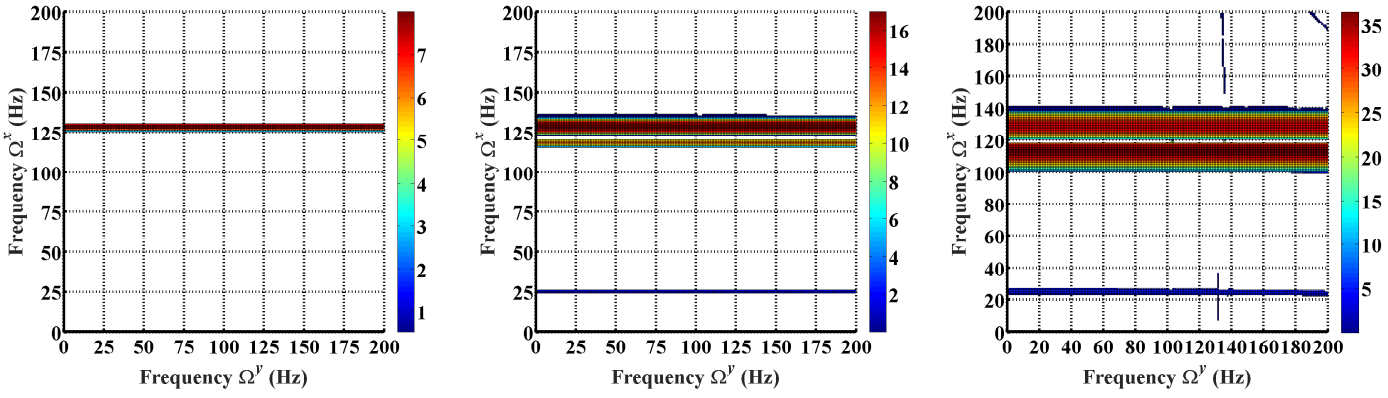

(a) (b) (c)

Fig. 17. Stability charts of the rotor excited by combined sinusoidal rotations of the support around the pitch and roll axes: $\beta = \beta^a \cos\Omega^x t$ and $\gamma = \gamma^a \cos\Omega^y t$ with $\beta^a = \gamma^a =$ (a) 0.05 rad, (b) 0.1 rad, (c) 0.2 rad.

6.5. *Instability due to mass unbalance combined with sinusoidal translations of the support*

In the presence of the mass unbalance excitation, the parametric influence on the equations of motion of the on-board rotor-hydrodynamic bearing system is created not only by the rotational motions of the rigid support (as can be seen in [11,14–17]) but also by its translational motions (see Eqs. (49), (52), (A.14)–(A.16)). This parametric influence is considered as a source of internal excitation and can lead to dynamic instability of the rotor. If the translational motions of the support are sinusoidal, the parametric influence is represented by periodic time-varying terms in the equations of motion. This type of equations can be once again treated by the Floquet theory in order to evaluate the dynamic stability of the rotor. The stiffness matrix of the rotor generated by the rotating mass unbalance combined with the support translations can show couplings between the flexural and torsional degrees of freedom. Thus it is expected that during the dynamic stability analysis, tongues due to pure bending and torsion (in the case of the support translations either along Ox or Oz) as well as to coupling between both phenomena (only in the case of the support translations along the Oy axis) can be encountered.

6.5.1. *Influence of the mass unbalance value*

Fig. 18 illustrates the stability charts of the on-board rotor running at a constant speed of rotation $\Omega = 1200$ rpm (= 20 Hz = mass unbalance frequency) and subject to mass unbalance excitations combined with sinusoidal translations of the rigid support defined by $z_O = Z_O \cos \Omega_{tr}^z t$ in m. The two variables involved in the parametric excitation generated in the rotor and used for the stabilty analysis are based on the amplitude Z_O and the frequency Ω_{tr}^z. In Fig. 18(a), the mass unbalance has a value $m_{mu1} r_{mu1} = m_{mu2} r_{mu2} = 3150$ g mm, while in Fig. 18(b), its value is $m_{mu1} r_{mu1} = m_{mu2} r_{mu2} = 6300$ g mm. Its phases are chosen to be $\eta_{mu1} = \eta_{mu2} = 0°$. Qualitatively, it can be observed that the instability zones become much more important for the mass unbalance of 6300 g mm located on the external disks 1 and 3 (as expected). As can be deduced quantitatively from Fig. 18, the narrow regions of instability permit writing the relationship $f_{ins} = |\Omega \pm \Omega_{su}| \simeq \frac{f_r^i \pm f_r^j}{k}$ where f_{ins} (in Hz) is the instability frequency, Ω (in Hz) is the mass unbalance frequency, Ω_{su} (in Hz) is the support motion frequency, f_r^i as well as f_r^j (in Hz) are the i-th and j-th natural frequencies of the rotor and the positive integer k is the order of the instability. Namely, this relationship proves the interaction between the frequencies of the mass unbalance excitation and the support motions. For instance, the stability chart displayed in Fig. 18(b) shows four tongues corresponding to the frequencies 57 Hz, 97 Hz, 175 Hz and 194 Hz. The support motion frequency $\Omega_{tr}^z = 57$ Hz can be relevant either to the first bending mode or to the first torsion mode because the instability frequency $f_{ins} = |\Omega - \Omega_{tr}^z| = |20 - 57| = 37$ Hz $\simeq 2 f_r^{b1} \simeq f_r^{t1}$ (see Table 4), i.e., the orders of the instability are $k = 1$ and 2 respectively. This frequency can also excite either

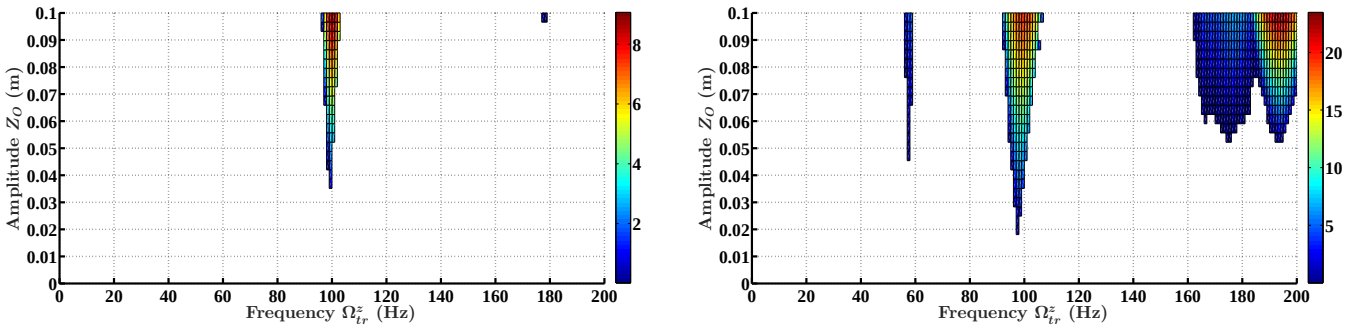

(a) (b)

Fig. 18. Stability charts of the rotor excited by sinusoidal translations of the support combined with a mass unbalance excitation: $m_{mu1} r_{mu1} = m_{mu2} r_{mu2} =$ (a) 3150 g mm, (b) 6300 g mm.

Instability frequency f_{ins} (Hz)	Unstable modes
37	$2f_r^{b1}$ or f_r^{t1}
77	$2f_r^{t1}$ or $f_r^{b1} + f_r^{b2}$
117	f_r^{t2} or f_r^{b3}

Table 5. Unstable modes of the rotor subject to sinusoidal translations of the support combined with a mass unbalance excitation $m_{mu1} r_{mu1} = m_{mu2} r_{mu2} = 6300$ g mm.

the second torsion mode or the first and second bending modes since $f_{ins} = |20 + 57| = 77$ Hz $\simeq 2f_r^{t1} \simeq f_r^{b1} + f_r^{b2}$, i.e., a primary instability ($k = 1$). On the other hand, an instability of order $k = 2$ due either to the second torsion mode or to the third bending mode can be found at the support motion frequency $\Omega_{tr}^z = 97$ Hz because the instability frequency $f_{ins} = |\Omega - \Omega_{tr}^z| = |20 + 97| = 117$ Hz $\simeq f_r^{t2} \simeq f_r^{b3}$. The frequency $\Omega_{tr}^z = 97$ Hz can be associated with the instability of frequency $f_{ins} = |20 - 97| = 77$ Hz already discussed above. Table 5 presents a summary of the previous observations. Lastly, in order to determine precisely the unstable modes, the transient dynamic motion of the rotor should be obtained by solving the equations of motion with an integration algorithm and a modal participation analysis should be performed.

6.5.2. Influence of the mass unbalance phases

Now, the effects of the mass unbalance phases on the instability zones are investigated and some explanations are to be given about these effects when two sets of phases ($\eta_{mu1} = \eta_{mu2} = 0°$ and $\eta_{mu1} = 0°$, $\eta_{mu2} = 180°$) are considered. The results provided in Figs. 19–21 concern the stability charts of the on-board rotor excited by the mass unbalnce ($m_{mu1}r_{mu1} = m_{mu2}r_{mu2} = 6300$ g mm) combined with sinusoidal translational motions of the support along the Ox, Oy and Oz axes respectively. The speed of rotation of the rotor is $\Omega = 1200$ rpm ($= 20$ Hz $=$ mass unbalance frequency). The support translations are defined by $x_O = X_O \cos \Omega_{tr}^x t$ in m (see Fig. 19), $y_O = -y_{be.\#1} + Y_O \cos \Omega_{tr}^y t$ in m (see Fig. 20) and $z_O = Z_O \cos \Omega_{tr}^z t$ in m (see Fig. 21). In the case of support translations along Oy, there is a constant term $-y_{be.\#1}$ which comes from the fact that the origin O^g of the Galilean frame of reference R^g is positioned at the center of the bearing #1 but not at the origin O of the frame linked with the support R which is situated at the shaft end-point in the left-hand side, see Fig. 8. The stiffness matrix of the rotor system produced by the mass unbalance excitation combined with rotations and/or translations of the support confirms that only the second-order time derivatives of the coordinates x_O, y_O and z_O are found if rotational excitations of the support are not taken into consideration. In other words, the constant terms of the support coordinates x_O, y_O and z_O have no influence on the stability charts and the determination of the position of the origin O^g of the Galilean frame R^g is not necessary only in the case of translational motions of the support combined with the mass unbalance. Qualitatively, it should be noticed that the mass unbalance phases play a paramount role in the dynamic analysis by affecting significantly the instability intensity and the sizes of the unstable zones. The latters increase or decrease with the phase as highlighted

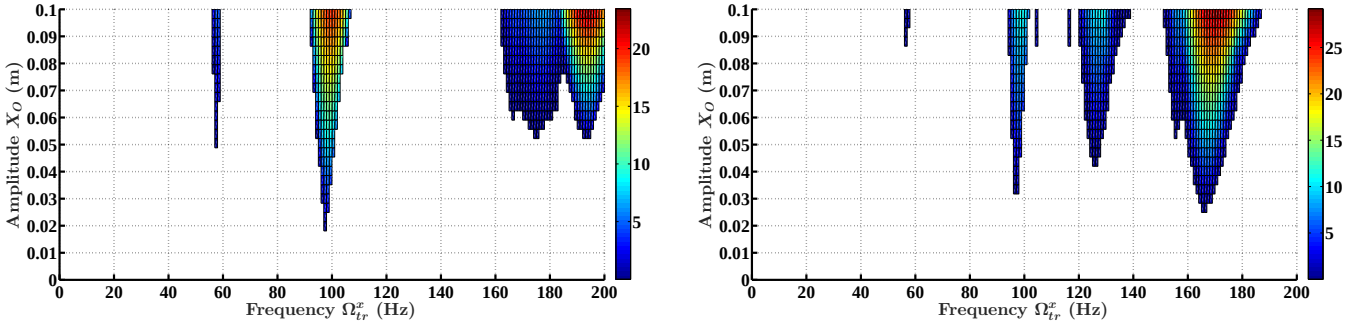

(a) (b)

Fig. 19. Stability charts of the rotor excited by sinusoidal translations of the support along the pitch axis and by a mass unbalance ($m_{mu1}r_{mu1} = m_{mu2}r_{mu2} = 6300$ g mm) of phases: (a) $\eta_{mu1} = \eta_{mu2} = 0°$, (b) $\eta_{mu1} = 0°$, $\eta_{mu2} = 180°$.

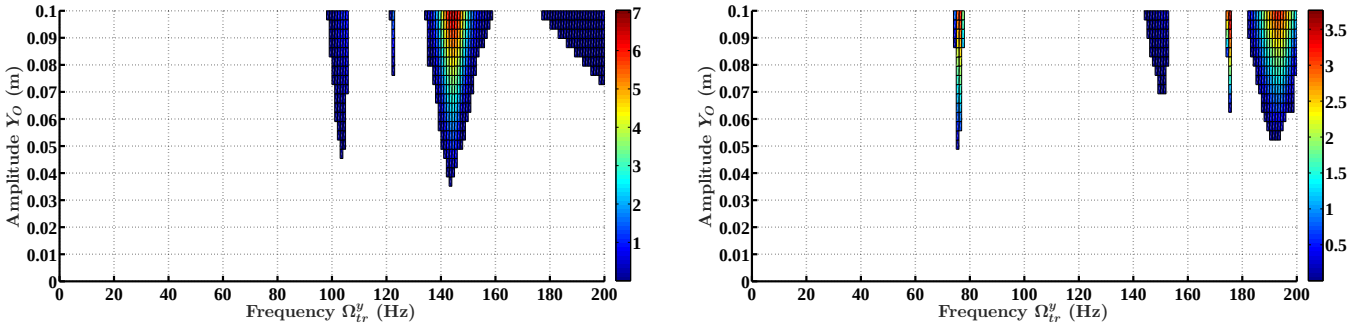

(a) (b)

Fig. 20. Stability charts of the rotor excited by sinusoidal translations of the support along the roll axis and by a mass unbalance ($m_{mu1}r_{mu1} = m_{mu2}r_{mu2} = 6300$ g mm) of phases: (a) $\eta_{mu1} = \eta_{mu2} = 0°$, (b) $\eta_{mu1} = 0°$, $\eta_{mu2} = 180°$.

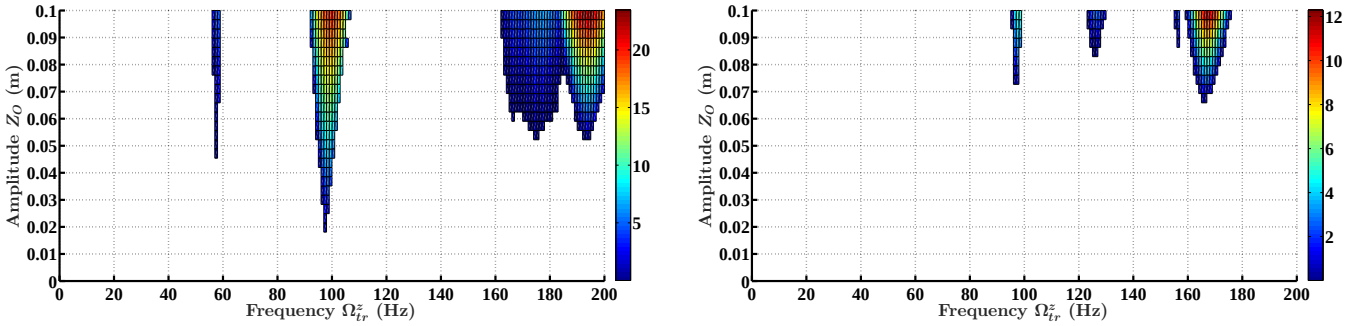

(a) (b)

Fig. 21. Stability charts of the rotor excited by sinusoidal translations of the support along the yaw axis and by a mass unbalance ($m_{mu1}r_{mu1} = m_{mu2}r_{mu2} = 6300$ g mm) of phases: (a) $\eta_{mu1} = \eta_{mu2} = 0°$, (b) $\eta_{mu1} = 0°$, $\eta_{mu2} = 180°$.

by Han and Chu [20]. For example, the instability tongues at 57 Hz and 97 Hz in Fig. 19(a) corresponding to equal phases are still present in Fig. 19(b) corresponding to opposite phases but much narrower and smaller. Quantitatively, the frequencies at the tongues of the instability regions can satisfy the relationship $f_{ins} = |\Omega \pm \Omega_{su}| \simeq \frac{f_r^i \pm f_r^j}{k}$ already stated above which reflects certainly the multi-frequency feature of the mass unbalance excitation combined with a sinusoidal translation of the support. For instance, the stability chart exhibited in Fig. 20(b) points out four narrow zones of instability associated with the frequencies 76 Hz, 150 Hz, 175 Hz and 192 Hz. The support motion frequency $\Omega^y_{tr} = 76$ Hz can be attached to the coupling between the first bending mode and the first torsion mode because the instability frequency $f_{ins} = |\Omega - \Omega^y_{tr}| = |20 - 76| = 56$ Hz $\simeq f_r^{b1} + f_r^{t1}$ (see Table 4), i.e., this result corresponds to a primary instability ($k = 1$).

7. Conclusions

A new finite element model is proposed in the current paper in order to assess the role of simple and combined sinusoidal rotational motions of the support as well as that of a mass unbalance excitation combined with sinusoidal translations of the support in the behavior stability of an on-board rotor-linearized hydrodynamic journal bearing system. This model is based on the Timoshenko beam theory and on six degrees of freedom (transverse and axial translations as well as rotations due to the bending and to the torsion). It involves the effects corresponding to the time-varying speed of rotation, the rotatory inertia, to the gyroscopic inertia and to the shaft shear deformation due to the bending as well as six kinds of deterministic movements (rotations and translations) of the rotor support. In addition, the hydrodynamic finite-length bearings are considered and the finite difference method is employed to solve the Reynolds equation and thereby to determine the damping and stiffness matrices. The equations of vibratory motion of the on-board rotor display that in the presence of the mass unbalance excitation, the parametric influence on them is generated not only by the rotational motions of the support but also by its translational motions. This parametric influence is considered as a source of internal excitation and can lead to a dynamic instability phenomenon of the rotor. It is represented by periodic time-varying terms in the equations of motion during sinusoidal motions of the rigid support. The rotor is examined through the application of the Floquet theory to its homogeneous equations of motion in order to evaluate its dynamic stability.

In the case of simple sinusoidal rotations of the support, the rotor instability is induced by single-frequency parametric excitations. The consideration of six degrees of freedom for the finite element model modifies significantly the stability charts when compared to those obtained with a model based only on the flexural ones. Namely, narrower regions of instability appear instead of a very wide zone and the instability tongues are produced not only by the pure bending modes but also by the interaction either between the bending and axial modes or between the bending and torsion ones. These outcomes can be explained by the low axial stiffness provided by the coupling (between the motor and the shaft), which permits a high participation of axial motions, and by the low frequencies of the torsion modes, which arise from the high rotatory inertia relevant to the disks. The pitch and yaw rotations (i.e., around a transverse axis) lead to instability zones more complex than those due to the roll rotation (i.e., around the longitudinal axis). The analytical bearing model can yield relatively accurate results for the stability charts because the damping and stiffness coefficients still have the same order of magnitude and are moderately modified when compared with those due to the finite difference method. The transient dynamic analysis of the on-board rotor for a non-stationary speed of rotation and given frequency and amplitude of the support rotation permits predicting the behavior stability without using the Floquet theory for each speed of rotation of the rotor contained in a certain interval.

In the cases of combined sinusoidal rotations of the support as well as a mass unbalance excitation combined with

sinusoidal translations of the support, the instability regions of the rotor are created by multi-frequency parametric excitations which are found to be more important than the single-frequency ones and which can make the stability charts more complicated by increasing the instability zones. For the combined rotational motions of the support around the pitch and yaw axes, the stability charts do not show perfectly horizontal or vertical instability zones especially at the intersections of the zones, which tend to become larger than expected. On the other hand, several diagonal instabilities characterized by linear functions between the frequencies of the support rotations are observed. Depending on these results, it is well understood that a multi-frequency stability chart cannot be obtained by superimposing simply single frequency ones obtained separately for each type of support rotations. For the mass unbalance correlated with support translations, it is demonstrated that during the dynamic stability analysis, instability tongues due to pure bending and torsion (in the case of the support translations along a transverse axis) as well as to coupling between both phenomena (only in the case of the support translations along the longitudinal axis) are encountered. Qualitatively, the instabilities become much more important for increasing values of the mass unbalance and its phases play a main role in the dynamic analysis by affecting significantly the instability intensity and the size of the instability zones. In practice, it can be difficult to meet large values of mass unbalance which have produced the stability charts in this work.

Acknowledgements

The authors gratefully acknowledge the financial support of the French National Research Agency (ANR) in the framework of the LaBCoM-PME AdViTAM, ANR-16-LCV1-0006, a joint laboratory of LaMCoS and AVNIR Engineering.

Appendix A

The elementary matrices and vectors for the disk finite element are described in Eqs. (A.1)–(A.5) as follows:

$$\mathbf{M}_{ed}^{tr} = \begin{bmatrix} m_d & 0 & 0 & 0 & 0 & 0 \\ 0 & m_d & 0 & 0 & 0 & 0 \\ 0 & 0 & m_d & 0 & 0 & 0 \\ 0 & 0 & 0 & 0 & 0 & 0 \\ 0 & 0 & 0 & 0 & 0 & 0 \\ 0 & 0 & 0 & 0 & 0 & 0 \end{bmatrix}; \qquad \mathbf{M}_{ed}^{ro} = \begin{bmatrix} 0 & 0 & 0 & 0 & 0 & 0 \\ 0 & 0 & 0 & 0 & 0 & 0 \\ 0 & 0 & 0 & 0 & 0 & 0 \\ 0 & 0 & 0 & I_{m_d}^{mo} & 0 & 0 \\ 0 & 0 & 0 & 0 & I_{m_d}^{y} & 0 \\ 0 & 0 & 0 & 0 & 0 & I_{m_d}^{mo} \end{bmatrix}, \tag{A.1}$$

$$\mathbf{C}_{ed}^{g} = \begin{bmatrix} 0 & 0 & 0 & 0 & 0 & 0 \\ 0 & 0 & 0 & 0 & 0 & 0 \\ 0 & 0 & 0 & 0 & 0 & 0 \\ 0 & 0 & 0 & 0 & 0 & -I_{m_d}^{y} \\ 0 & 0 & 0 & 0 & 0 & 0 \\ 0 & 0 & 0 & I_{m_d}^{y} & 0 & 0 \end{bmatrix}; \qquad \mathbf{K}_{ed}^{g} = \begin{bmatrix} 0 & 0 & 0 & 0 & 0 & 0 \\ 0 & 0 & 0 & 0 & 0 & 0 \\ 0 & 0 & 0 & 0 & 0 & 0 \\ 0 & 0 & 0 & 0 & 0 & 0 \\ 0 & 0 & 0 & 0 & 0 & 0 \\ 0 & 0 & 0 & I_{m_d}^{y} & 0 & 0 \end{bmatrix}, \tag{A.2}$$

$$\mathbf{C}_{ed,su}^{\omega^x} = \begin{bmatrix} 0 & 0 & 0 & 0 & 0 & 0 \\ 0 & 0 & -2m_d & 0 & 0 & 0 \\ 0 & 2m_d & 0 & 0 & 0 & 0 \\ 0 & 0 & 0 & 0 & 0 & 0 \\ 0 & 0 & 0 & 0 & 0 & -I_{m_d}^{y} \\ 0 & 0 & 0 & 0 & I_{m_d}^{y} & 0 \end{bmatrix}; \quad \mathbf{C}_{ed,su}^{\omega^y} = \begin{bmatrix} 0 & 0 & 2m_d & 0 & 0 & 0 \\ 0 & 0 & 0 & 0 & 0 & 0 \\ -2m_d & 0 & 0 & 0 & 0 & 0 \\ 0 & 0 & 0 & 0 & 0 & -\left(I_{m_d}^{y} - 2I_{m_d}^{mo}\right) \\ 0 & 0 & 0 & 0 & 0 & 0 \\ 0 & 0 & 0 & I_{m_d}^{y} - 2I_{m_d}^{mo} & 0 & 0 \end{bmatrix};$$

$$\mathbf{C}_{ed,su}^{\omega^z} = \begin{bmatrix} 0 & -2m_d & 0 & 0 & 0 & 0 \\ 2m_d & 0 & 0 & 0 & 0 & 0 \\ 0 & 0 & 0 & 0 & 0 & 0 \\ 0 & 0 & 0 & 0 & -I_{m_d}^{y} & 0 \\ 0 & 0 & 0 & I_{m_d}^{y} & 0 & 0 \\ 0 & 0 & 0 & 0 & 0 & 0 \end{bmatrix}, \tag{A.3}$$

$$\mathbf{K}^{\dot{\omega}^x}_{ed,su} = \begin{bmatrix} 0 & 0 & 0 & 0 & 0 & 0 \\ 0 & 0 & -m_d & 0 & 0 & 0 \\ 0 & m_d & 0 & 0 & 0 & 0 \\ 0 & 0 & 0 & 0 & 0 & 0 \\ 0 & 0 & 0 & 0 & 0 & -I^y_{m_d} \\ 0 & 0 & 0 & 0 & 0 & 0 \end{bmatrix}; \qquad \mathbf{K}^{\dot{\omega}^y}_{ed,su} = \begin{bmatrix} 0 & 0 & m_d & 0 & 0 & 0 \\ 0 & 0 & 0 & 0 & 0 & 0 \\ -m_d & 0 & 0 & 0 & 0 & 0 \\ 0 & 0 & 0 & 0 & 0 & I^{mo}_{m_d} \\ 0 & 0 & 0 & 0 & 0 & 0 \\ 0 & 0 & 0 & I^y_{m_d} - I^{mo}_{m_d} & 0 & 0 \end{bmatrix};$$

$$\mathbf{K}^{\dot{\omega}^z}_{ed,su} = \begin{bmatrix} 0 & -m_d & 0 & 0 & 0 & 0 \\ m_d & 0 & 0 & 0 & 0 & 0 \\ 0 & 0 & 0 & 0 & 0 & 0 \\ 0 & 0 & 0 & 0 & 0 & 0 \\ 0 & 0 & 0 & I^y_{m_d} & 0 & 0 \\ 0 & 0 & 0 & 0 & 0 & 0 \end{bmatrix}; \qquad \mathbf{K}^{\dot{\phi}\,\omega^y}_{ed,su} = \begin{bmatrix} 0 & 0 & 0 & 0 & 0 & 0 \\ 0 & 0 & 0 & 0 & 0 & 0 \\ 0 & 0 & 0 & 0 & 0 & 0 \\ 0 & 0 & 0 & I^y_{m_d} & 0 & 0 \\ 0 & 0 & 0 & 0 & 0 & 0 \\ 0 & 0 & 0 & 0 & 0 & I^y_{m_d} \end{bmatrix};$$

$$\mathbf{K}^{\omega^{x2}}_{ed,su} = \begin{bmatrix} 0 & 0 & 0 & 0 & 0 & 0 \\ 0 & -m_d & 0 & 0 & 0 & 0 \\ 0 & 0 & -m_d & 0 & 0 & 0 \\ 0 & 0 & 0 & 0 & 0 & 0 \\ 0 & 0 & 0 & 0 & 0 & 0 \\ 0 & 0 & 0 & 0 & 0 & -\left(I^y_{m_d} - I^{mo}_{m_d}\right) \end{bmatrix}; \qquad \mathbf{K}^{\omega^{y2}}_{ed,su} = \begin{bmatrix} -m_d & 0 & 0 & 0 & 0 & 0 \\ 0 & 0 & 0 & 0 & 0 & 0 \\ 0 & 0 & -m_d & 0 & 0 & 0 \\ 0 & 0 & 0 & I^y_{m_d} - I^{mo}_{m_d} & 0 & 0 \\ 0 & 0 & 0 & 0 & 0 & 0 \\ 0 & 0 & 0 & 0 & 0 & I^y_{m_d} - I^{mo}_{m_d} \end{bmatrix};$$

$$\mathbf{K}^{\omega^{z2}}_{ed,su} = \begin{bmatrix} -m_d & 0 & 0 & 0 & 0 & 0 \\ 0 & -m_d & 0 & 0 & 0 & 0 \\ 0 & 0 & 0 & 0 & 0 & 0 \\ 0 & 0 & 0 & -\left(I^y_{m_d} - I^{mo}_{m_d}\right) & 0 & 0 \\ 0 & 0 & 0 & 0 & 0 & 0 \\ 0 & 0 & 0 & 0 & 0 & 0 \end{bmatrix}; \qquad \mathbf{K}^{\omega^x\,\omega^y}_{ed,su} = \begin{bmatrix} 0 & m_d & 0 & 0 & 0 & 0 \\ m_d & 0 & 0 & 0 & 0 & 0 \\ 0 & 0 & 0 & 0 & 0 & 0 \\ 0 & 0 & 0 & 0 & 0 & 0 \\ 0 & 0 & 0 & 0 & 0 & 0 \\ 0 & 0 & 0 & 0 & 0 & 0 \end{bmatrix};$$

$$\mathbf{K}^{\omega^x\,\omega^z}_{ed,su} = \begin{bmatrix} 0 & 0 & m_d & 0 & 0 & 0 \\ 0 & 0 & 0 & 0 & 0 & 0 \\ m_d & 0 & 0 & 0 & 0 & 0 \\ 0 & 0 & 0 & 0 & 0 & I^y_{m_d} - I^{mo}_{m_d} \\ 0 & 0 & 0 & 0 & 0 & 0 \\ 0 & 0 & 0 & I^y_{m_d} - I^{mo}_{m_d} & 0 & 0 \end{bmatrix}; \qquad \mathbf{K}^{\omega^y\,\omega^z}_{ed,su} = \begin{bmatrix} 0 & 0 & 0 & 0 & 0 & 0 \\ 0 & 0 & m_d & 0 & 0 & 0 \\ 0 & m_d & 0 & 0 & 0 & 0 \\ 0 & 0 & 0 & 0 & 0 & 0 \\ 0 & 0 & 0 & 0 & 0 & 0 \\ 0 & 0 & 0 & 0 & 0 & 0 \end{bmatrix}, \tag{A.4}$$

$$\mathbf{V}^{\lambda}_{ed} = \begin{bmatrix} 0 & 0 & 0 & 0 & I^y_{m_d} & 0 \end{bmatrix}^T; \qquad \mathbf{V}^{u}_{ed,su} = \begin{bmatrix} m_d & 0 & 0 & 0 & 0 & 0 \end{bmatrix}^T;$$
$$\mathbf{V}^{v}_{ed,su} = \begin{bmatrix} 0 & m_d & 0 & 0 & 0 & 0 \end{bmatrix}^T; \qquad \mathbf{V}^{w}_{ed,su} = \begin{bmatrix} 0 & 0 & m_d & 0 & 0 & 0 \end{bmatrix}^T;$$
$$\mathbf{V}^{y\,w}_{ed,su} = y_d \begin{bmatrix} 0 & 0 & m_d & 0 & 0 & 0 \end{bmatrix}^T; \qquad \mathbf{V}^{y\,u}_{ed,su} = y_d \begin{bmatrix} m_d & 0 & 0 & 0 & 0 & 0 \end{bmatrix}^T;$$
$$\mathbf{V}^{y\,v}_{ed,su} = y_d \begin{bmatrix} 0 & m_d & 0 & 0 & 0 & 0 \end{bmatrix}^T; \qquad \mathbf{V}^{\theta}_{ed,su} = \begin{bmatrix} 0 & 0 & 0 & I^{mo}_{m_d} & 0 & 0 \end{bmatrix}^T;$$
$$\mathbf{V}^{\lambda}_{ed,su} = \begin{bmatrix} 0 & 0 & 0 & 0 & I^y_{m_d} & 0 \end{bmatrix}^T; \qquad \mathbf{V}^{\psi}_{ed,su} = \begin{bmatrix} 0 & 0 & 0 & 0 & 0 & I^{mo}_{m_d} \end{bmatrix}^T;$$
$$\mathbf{V}^{y\,\psi}_{ed,su} = \begin{bmatrix} 0 & 0 & 0 & 0 & 0 & I^y_{m_d} \end{bmatrix}^T; \qquad \mathbf{V}^{y\,\theta}_{ed,su} = \begin{bmatrix} 0 & 0 & 0 & I^y_{m_d} & 0 & 0 \end{bmatrix}^T. \tag{A.5}$$

All the expressions calculating the elementary matrices and vectors for the shaft finite element are given in Eqs. (A.6)–(A.11) as follows:

$$\mathbf{M}^{tr}_{esh_i} = \rho_{esh_i} S_{esh_i} l_{esh_i} \int_0^1 \left(\left(\bar{\mathbf{F}}^{u}_{esh_i}\right)^T \bar{\mathbf{F}}^{u}_{esh_i} + \left(\bar{\mathbf{F}}^{v}_{esh_i}\right)^T \bar{\mathbf{F}}^{v}_{esh_i} + \left(\bar{\mathbf{F}}^{w}_{esh_i}\right)^T \bar{\mathbf{F}}^{w}_{esh_i} \right) \mathrm{d}\bar{y};$$
$$\mathbf{M}^{ro}_{esh_i} = \rho_{esh_i} I^{mo}_{S_{esh_i}} l_{esh_i} \int_0^1 \left(\left(\bar{\mathbf{F}}^{\theta}_{esh_i}\right)^T \bar{\mathbf{F}}^{\theta}_{esh_i} + 2\left(\bar{\mathbf{F}}^{\lambda}_{esh_i}\right)^T \bar{\mathbf{F}}^{\lambda}_{esh_i} + \left(\bar{\mathbf{F}}^{\psi}_{esh_i}\right)^T \bar{\mathbf{F}}^{\psi}_{esh_i} \right) \mathrm{d}\bar{y}, \tag{A.6}$$

$$\mathbf{C}^{g}_{esh_i} = 2\rho_{esh_i} I^{mo}_{S_{esh_i}} l_{esh_i} \int_0^1 \left(\left(\bar{\mathbf{F}}^{\psi}_{esh_i}\right)^T \bar{\mathbf{F}}^{\theta}_{esh_i} - \left(\bar{\mathbf{F}}^{\theta}_{esh_i}\right)^T \bar{\mathbf{F}}^{\psi}_{esh_i} \right) \mathrm{d}\bar{y};$$
$$\mathbf{K}^{g}_{esh_i} = 2\rho_{esh_i} I^{mo}_{S_{esh_i}} l_{esh_i} \int_0^1 \left(\bar{\mathbf{F}}^{\psi}_{esh_i}\right)^T \bar{\mathbf{F}}^{\theta}_{esh_i} \mathrm{d}\bar{y}, \tag{A.7}$$

$$
\begin{aligned}
\mathbf{K}^{e}_{esh_i} = {} & E_{esh_i} I^{mo}_{S_{esh_i}} l_{esh_i} \int_0^1 \left(\left(\frac{\partial \bar{\mathbf{F}}^{\theta}_{esh_i}}{\partial y} \right)^T \frac{\partial \bar{\mathbf{F}}^{\theta}_{esh_i}}{\partial y} + \quad \frac{\partial \bar{\mathbf{F}}_{esh_i}}{\partial y} \right)^T \frac{\partial \bar{\mathbf{F}}_{esh_i}}{\partial y} \right) \mathrm{d}\bar{y} \\
& + G_{esh_i} \kappa^{mo}_{esh_i} S_{esh_i} l_{esh_i} \int_0^1 \left(\left(\frac{\partial \bar{\mathbf{F}}^{u}_{esh_i}}{\partial y} + \bar{\mathbf{F}}_{esh_i} \right)^T \quad \frac{\partial \bar{\mathbf{F}}^{u}_{esh_i}}{\partial y} + \bar{\mathbf{F}}_{esh_i} \right) \right) \mathrm{d}\bar{y} \\
& + G_{esh_i} \kappa^{mo}_{esh_i} S_{esh_i} l_{esh_i} \int_0^1 \left(\left(\frac{\partial \bar{\mathbf{F}}^{w}_{esh_i}}{\partial y} - \bar{\mathbf{F}}^{\theta}_{esh_i} \right)^T \quad \frac{\partial \bar{\mathbf{F}}^{w}_{esh_i}}{\partial y} - \bar{\mathbf{F}}^{\theta}_{esh_i} \right) \right) \mathrm{d}\bar{y} \\
& + E_{esh_i} S_{esh_i} l_{esh_i} \int_0^1 \quad \frac{\partial \bar{\mathbf{F}}^{v}_{esh_i}}{\partial y} \Bigg)^T \frac{\partial \bar{\mathbf{F}}^{v}_{esh_i}}{\partial y} \, \mathrm{d}\bar{y} + 2 G_{esh_i} I^{mo}_{S_{esh_i}} l_{esh_i} \int_0^1 \quad \frac{\partial \bar{\mathbf{F}}^{\lambda}_{esh_i}}{\partial y} \Bigg)^T \frac{\partial \bar{\mathbf{F}}^{\lambda}_{esh_i}}{\partial y} \, \mathrm{d}\bar{y},
\end{aligned}
\tag{A.8}
$$

$$
\begin{aligned}
\mathbf{C}^{\omega^x}_{esh_i,su} &= 2\rho_{esh_i} S_{esh_i} l_{esh_i} \int_0^1 \left(\left(\bar{\mathbf{F}}^{w}_{esh_i} \right)^T \bar{\mathbf{F}}^{v}_{esh_i} - \left(\bar{\mathbf{F}}^{v}_{esh_i} \right)^T \bar{\mathbf{F}}^{w}_{esh_i} \right) \mathrm{d}\bar{y} \\
&\quad + 2\rho_{esh_i} I^{mo}_{S_{esh_i}} l_{esh_i} \int_0^1 \left(\left(\bar{\mathbf{F}}_{esh_i} \right)^T \bar{\mathbf{F}}^{\lambda}_{esh_i} - \left(\bar{\mathbf{F}}^{\lambda}_{esh_i} \right)^T \bar{\mathbf{F}}_{esh_i} \right) \mathrm{d}\bar{y}; \\
\mathbf{C}^{\omega^y}_{esh_i,su} &= 2\rho_{esh_i} S_{esh_i} l_{esh_i} \int_0^1 \left(\left(\bar{\mathbf{F}}^{u}_{esh_i} \right)^T \bar{\mathbf{F}}^{w}_{esh_i} - \left(\bar{\mathbf{F}}^{w}_{esh_i} \right)^T \bar{\mathbf{F}}^{u}_{esh_i} \right) \mathrm{d}\bar{y}; \\
\mathbf{C}^{\omega^z}_{esh_i,su} &= 2\rho_{esh_i} S_{esh_i} l_{esh_i} \int_0^1 \left(\left(\bar{\mathbf{F}}^{v}_{esh_i} \right)^T \bar{\mathbf{F}}^{u}_{esh_i} - \left(\bar{\mathbf{F}}^{u}_{esh_i} \right)^T \bar{\mathbf{F}}^{v}_{esh_i} \right) \mathrm{d}\bar{y} \\
&\quad + 2\rho_{esh_i} I^{mo}_{S_{esh_i}} l_{esh_i} \int_0^1 \left(\left(\bar{\mathbf{F}}^{\lambda}_{esh_i} \right)^T \bar{\mathbf{F}}^{\theta}_{esh_i} - \left(\bar{\mathbf{F}}^{\theta}_{esh_i} \right)^T \bar{\mathbf{F}}^{\lambda}_{esh_i} \right) \mathrm{d}\bar{y},
\end{aligned}
\tag{A.9}
$$

$$
\begin{aligned}
\mathbf{K}^{\dot{\omega}^x}_{esh_i,su} &= \rho_{esh_i} S_{esh_i} l_{esh_i} \int_0^1 \left(\left(\bar{\mathbf{F}}^{w}_{esh_i} \right)^T \bar{\mathbf{F}}^{v}_{esh_i} - \left(\bar{\mathbf{F}}^{v}_{esh_i} \right)^T \bar{\mathbf{F}}^{w}_{esh_i} \right) \mathrm{d}\bar{y} \\
&\quad - 2\rho_{esh_i} I^{mo}_{S_{esh_i}} l_{esh_i} \int_0^1 \left(\bar{\mathbf{F}}^{\lambda}_{esh_i} \right)^T \bar{\mathbf{F}}_{esh_i} \mathrm{d}\bar{y}; \\
\mathbf{K}^{\dot{\omega}^y}_{esh_i,su} &= \rho_{esh_i} S_{esh_i} l_{esh_i} \int_0^1 \left(\left(\bar{\mathbf{F}}^{u}_{esh_i} \right)^T \bar{\mathbf{F}}^{w}_{esh_i} - \left(\bar{\mathbf{F}}^{w}_{esh_i} \right)^T \bar{\mathbf{F}}^{u}_{esh_i} \right) \mathrm{d}\bar{y} \\
&\quad + \rho_{esh_i} I^{mo}_{S_{esh_i}} l_{esh_i} \int_0^1 \left(\left(\bar{\mathbf{F}}^{\theta}_{esh_i} \right)^T \bar{\mathbf{F}}_{esh_i} + \left(\bar{\mathbf{F}}_{esh_i} \right)^T \bar{\mathbf{F}}^{\theta}_{esh_i} \right) \mathrm{d}\bar{y}; \\
\mathbf{K}^{\dot{\omega}^z}_{esh_i,su} &= \rho_{esh_i} S_{esh_i} l_{esh_i} \int_0^1 \left(\left(\bar{\mathbf{F}}^{v}_{esh_i} \right)^T \bar{\mathbf{F}}^{u}_{esh_i} - \left(\bar{\mathbf{F}}^{u}_{esh_i} \right)^T \bar{\mathbf{F}}^{v}_{esh_i} \right) \mathrm{d}\bar{y} \\
&\quad + 2\rho_{esh_i} I^{mo}_{S_{esh_i}} l_{esh_i} \int_0^1 \left(\bar{\mathbf{F}}^{\lambda}_{esh_i} \right)^T \bar{\mathbf{F}}^{\theta}_{esh_i} \mathrm{d}\bar{y}; \\
\mathbf{K}^{\dot{\phi}\,\omega^y}_{esh_i,su} &= 2\rho_{esh_i} I^{mo}_{S_{esh_i}} l_{esh_i} \int_0^1 \left(\left(\bar{\mathbf{F}}^{\theta}_{esh_i} \right)^T \bar{\mathbf{F}}^{\theta}_{esh_i} + \left(\bar{\mathbf{F}}_{esh_i} \right)^T \bar{\mathbf{F}}_{esh_i} \right) \mathrm{d}\bar{y}; \\
\mathbf{K}^{\omega^{x2}}_{esh_i,su} &= -\rho_{esh_i} S_{esh_i} l_{esh_i} \int_0^1 \left(\left(\bar{\mathbf{F}}^{v}_{esh_i} \right)^T \bar{\mathbf{F}}^{v}_{esh_i} + \left(\bar{\mathbf{F}}^{w}_{esh_i} \right)^T \bar{\mathbf{F}}^{w}_{esh_i} \right) \mathrm{d}\bar{y} \\
&\quad - \rho_{esh_i} I^{mo}_{S_{esh_i}} l_{esh_i} \int_0^1 \left(\bar{\mathbf{F}}_{esh_i} \right)^T \bar{\mathbf{F}}_{esh_i} \mathrm{d}\bar{y}; \\
\mathbf{K}^{\omega^{y2}}_{esh_i,su} &= -\rho_{esh_i} S_{esh_i} l_{esh_i} \int_0^1 \left(\left(\bar{\mathbf{F}}^{u}_{esh_i} \right)^T \bar{\mathbf{F}}^{u}_{esh_i} + \left(\bar{\mathbf{F}}^{w}_{esh_i} \right)^T \bar{\mathbf{F}}^{w}_{esh_i} \right) \mathrm{d}\bar{y} \\
&\quad + \rho_{esh_i} I^{mo}_{S_{esh_i}} l_{esh_i} \int_0^1 \left(\left(\bar{\mathbf{F}}^{\theta}_{esh_i} \right)^T \bar{\mathbf{F}}^{\theta}_{esh_i} + \left(\bar{\mathbf{F}}_{esh_i} \right)^T \bar{\mathbf{F}}_{esh_i} \right) \mathrm{d}\bar{y}; \\
\mathbf{K}^{\omega^{z2}}_{esh_i,su} &= -\rho_{esh_i} S_{esh_i} l_{esh_i} \int_0^1 \left(\left(\bar{\mathbf{F}}^{u}_{esh_i} \right)^T \bar{\mathbf{F}}^{u}_{esh_i} + \left(\bar{\mathbf{F}}^{v}_{esh_i} \right)^T \bar{\mathbf{F}}^{v}_{esh_i} \right) \mathrm{d}\bar{y} \\
&\quad - \rho_{esh_i} I^{mo}_{S_{esh_i}} l_{esh_i} \int_0^1 \left(\bar{\mathbf{F}}^{\theta}_{esh_i} \right)^T \bar{\mathbf{F}}^{\theta}_{esh_i} \mathrm{d}\bar{y};
\end{aligned}
$$

$$\mathbf{K}^{\omega^x\,\omega^y}_{esh_i,su} = \rho_{esh_i} S_{esh_i} l_{esh_i} \int_0^1 \left(\left(\bar{\mathbf{F}}^u_{esh_i}\right)^T \bar{\mathbf{F}}^v_{esh_i} + \left(\bar{\mathbf{F}}^v_{esh_i}\right)^T \bar{\mathbf{F}}^u_{esh_i} \right) \mathrm{d}\bar{y};$$

$$\mathbf{K}^{\omega^x\,\omega^z}_{esh_i,su} = \rho_{esh_i} S_{esh_i} l_{esh_i} \int_0^1 \left(\left(\bar{\mathbf{F}}^u_{esh_i}\right)^T \bar{\mathbf{F}}^w_{esh_i} + \left(\bar{\mathbf{F}}^w_{esh_i}\right)^T \bar{\mathbf{F}}^u_{esh_i} \right) \mathrm{d}\bar{y}$$
$$+ \rho_{esh_i} I^{mo}_{S_{esh_i}} l_{esh_i} \int_0^1 \left(\left(\bar{\mathbf{F}}^\theta_{esh_i}\right)^T \bar{\mathbf{F}}_{esh_i} + \left(\bar{\mathbf{F}}_{esh_i}\right)^T \bar{\mathbf{F}}^\theta_{esh_i} \right) \mathrm{d}\bar{y};$$

$$\mathbf{K}^{\omega^y\,\omega^z}_{esh_i,su} = \rho_{esh_i} S_{esh_i} l_{esh_i} \int_0^1 \left(\left(\bar{\mathbf{F}}^v_{esh_i}\right)^T \bar{\mathbf{F}}^w_{esh_i} + \left(\bar{\mathbf{F}}^w_{esh_i}\right)^T \bar{\mathbf{F}}^v_{esh_i} \right) \mathrm{d}\bar{y}, \tag{A.10}$$

$$\mathbf{V}^\lambda_{esh_i} = 2\rho_{esh_i} I^{mo}_{S_{esh_i}} l_{esh_i} \int_0^1 \left(\bar{\mathbf{F}}^\lambda_{esh_i}\right)^T \mathrm{d}\bar{y}; \qquad \mathbf{V}^u_{esh_i,su} = \rho_{esh_i} S_{esh_i} l_{esh_i} \int_0^1 \left(\bar{\mathbf{F}}^u_{esh_i}\right)^T \mathrm{d}\bar{y};$$

$$\mathbf{V}^v_{esh_i,su} = \rho_{esh_i} S_{esh_i} l_{esh_i} \int_0^1 \left(\bar{\mathbf{F}}^v_{esh_i}\right)^T \mathrm{d}\bar{y}; \qquad \mathbf{V}^w_{esh_i,su} = \rho_{esh_i} S_{esh_i} l_{esh_i} \int_0^1 \left(\bar{\mathbf{F}}^w_{esh_i}\right)^T \mathrm{d}\bar{y};$$

$$\mathbf{V}^{yw}_{esh_i,su} = \rho_{esh_i} S_{esh_i} l^2_{esh_i} \int_0^1 \left(\bar{\mathbf{F}}^w_{esh_i}\right)^T \bar{y}\mathrm{d}\bar{y}; \qquad \mathbf{V}^{yu}_{esh_i,su} = \rho_{esh_i} S_{esh_i} l^2_{esh_i} \int_0^1 \left(\bar{\mathbf{F}}^u_{esh_i}\right)^T \bar{y}\mathrm{d}\bar{y};$$

$$\mathbf{V}^{yv}_{esh_i,su} = \rho_{esh_i} S_{esh_i} l^2_{esh_i} \int_0^1 \left(\bar{\mathbf{F}}^v_{esh_i}\right)^T \bar{y}\mathrm{d}\bar{y}; \qquad \mathbf{V}^\theta_{esh_i,su} = \rho_{esh_i} I^{mo}_{S_{esh_i}} l_{esh_i} \int_0^1 \left(\bar{\mathbf{F}}^\theta_{esh_i}\right)^T \mathrm{d}\bar{y};$$

$$\mathbf{V}^\lambda_{esh_i,su} = 2\rho_{esh_i} I^{mo}_{S_{esh_i}} l_{esh_i} \int_0^1 \left(\bar{\mathbf{F}}^\lambda_{esh_i}\right)^T \mathrm{d}\bar{y}; \qquad \mathbf{V}^\psi_{esh_i,su} = \rho_{esh_i} I^{mo}_{S_{esh_i}} l_{esh_i} \int_0^1 \left(\bar{\mathbf{F}}_{esh_i}\right)^T \mathrm{d}\bar{y};$$

$$\mathbf{V}^{y\psi}_{esh_i,su} = 2\rho_{esh_i} I^{mo}_{S_{esh_i}} l_{esh_i} \int_0^1 \left(\bar{\mathbf{F}}_{esh_i}\right)^T \mathrm{d}\bar{y}; \qquad \mathbf{V}^{y\theta}_{esh_i,su} = 2\rho_{esh_i} I^{mo}_{S_{esh_i}} l_{esh_i} \int_0^1 \left(\bar{\mathbf{F}}^\theta_{esh_i}\right)^T \mathrm{d}\bar{y}. \tag{A.11}$$

The original elementary matrices and vectors for the mass unbalance finite element are detailed hereafter

$$\mathbf{M}^{cs}_{emu} = m_{mu} \begin{bmatrix} 1 & 0 & 0 & 0 & z^* & 0 \\ 0 & 1 & 0 & -z^* & 0 & x^* \\ 0 & 0 & 1 & 0 & -x^* & 0 \\ 0 & -z^* & 0 & z^{*2} & 0 & -x^* z^* \\ z^* & 0 & -x^* & 0 & r^2_{mu} & 0 \\ 0 & x^* & 0 & -x^* z^* & 0 & x^{*2} \end{bmatrix}, \tag{A.12}$$

$$\mathbf{C}^{\dot{\phi}}_{emu} = 2m_{mu} \begin{bmatrix} 0 & 0 & 0 & 0 & -x^* & 0 \\ 0 & 0 & 0 & x^* & 0 & z^* \\ 0 & 0 & 0 & 0 & -z^* & 0 \\ 0 & 0 & 0 & -x^* z^* & 0 & -z^{*2} \\ 0 & 0 & 0 & 0 & 0 & 0 \\ 0 & 0 & 0 & x^{*2} & 0 & x^* z^* \end{bmatrix};$$

$$\mathbf{C}_{emu,su} = 2m_{mu} \begin{bmatrix} 0 & -\omega^z & \omega^y & z^*\omega^z & -x^*\omega^y & -x^*\omega^z \\ \omega^z & 0 & -\omega^x & 0 & x^*\omega^x + z^*\omega^z & 0 \\ -\omega^y & \omega^x & 0 & -z^*\omega^x & -z^*\omega^y & x^*\omega^x \\ -z^*\omega^z & 0 & z^*\omega^x & 0 & -z^*\left(x^*\omega^x + z^*\omega^z\right) & 0 \\ x^*\omega^y & -\left(x^*\omega^x + z^*\omega^z\right) & z^*\omega^y & z^*\left(x^*\omega^x + z^*\omega^z\right) & 0 & -x^*\left(x^*\omega^x + z^*\omega^z\right) \\ x^*\omega^z & 0 & -x^*\omega^x & 0 & x^*\left(x^*\omega^x + z^*\omega^z\right) & 0 \end{bmatrix}, \tag{A.13}$$

$$\mathbf{K}^{\ddot{\phi}}_{emu} = m_{mu} \begin{bmatrix} 0 & 0 & 0 & 0 & -x^* & 0 \\ 0 & 0 & 0 & x^* & 0 & z^* \\ 0 & 0 & 0 & 0 & -z^* & 0 \\ 0 & 0 & 0 & 0 & 0 & 0 \\ 0 & 0 & 0 & 0 & 0 & 0 \\ 0 & 0 & 0 & r^2_{mu} & 0 & 0 \end{bmatrix}; \qquad \mathbf{K}^{\dot{\phi}^2}_{emu} = m_{mu} \begin{bmatrix} 0 & 0 & 0 & 0 & -z^* & 0 \\ 0 & 0 & 0 & z^* & 0 & -x^* \\ 0 & 0 & 0 & 0 & x^* & 0 \\ 0 & 0 & 0 & 0 & 0 & 0 \\ 0 & 0 & 0 & 0 & 0 & 0 \\ 0 & 0 & 0 & 0 & 0 & 0 \end{bmatrix};$$

$$\mathbf{K}_{emu,su} = m_{mu} \begin{bmatrix} -K^{uu} & K^{uv} & K^{uw} & K^{u\theta} & K^{u\lambda} & K^u \\ K^{vu} & -K^{vv} & K^{vw} & z^*K^{vv} & K^{v\lambda} & -x^*K^{vv} \\ K^{wu} & K^{wv} & -K^{ww} & K^{w\theta} & K^{w\lambda} & K^w \\ -z^*K^{vu} & z^*K^{vv} & -z^*K^{vw} & z^*K^{\theta\theta} & K^{\theta\lambda} & z^*K^{\psi\psi} \\ -\left(x^*K^{wu} + z^*K^{uu}\right) & -x^*K^{wv} + z^*K^{uv} & x^*K^{wu} + z^*K^{uu} & K^{\lambda\theta} & K^{\lambda\lambda} & K^{\lambda\psi} \\ x^*K^{vu} & -x^*K^{vv} & x^*K^{vw} & z^*K & K^{\psi\lambda} & -x^*K^{\psi\psi} \end{bmatrix}, \tag{A.14}$$

with

$$
\begin{aligned}
K^{uu} &= \omega^{y2} + \omega^{z2}; & K^{uv} &= -\dot{\omega}^z + \omega^x\omega^y;\\
K^{uw} &= \dot{\omega}^y + \omega^x\omega^z; & K^{u\theta} &= -2x^*\dot{\phi}\,\omega^z - z^*K_{uv};\\
K^{u\lambda} &= -x^*K_{uw} - z^*\left(K_{uu} + 2\dot{\phi}\,\omega^y\right); & K^{u\psi} &= -2z^*\dot{\phi}\,\omega^z + x^*K_{uv};\\
K^{vu} &= \dot{\omega}^z + \omega^x\omega^y; & K^{vv} &= \omega^{x2} + \omega^{z2};\\
K^{vw} &= -\dot{\omega}^x + \omega^y\omega^z; & K^{v\lambda} &= z^*K_{vu} - x^*K_{vw} + 2\dot{\phi}\left(z^*\omega^x - x^*\omega^z\right);\\
K^{wu} &= -\dot{\omega}^y + \omega^x\omega^z; & K^{wv} &= \dot{\omega}^x + \omega^y\omega^z;\\
K^{ww} &= \omega^{x2} + \omega^{y2}; & K^{w\theta} &= 2x^*\dot{\phi}\,\omega^x - z^*K_{wv};\\
K^{w\lambda} &= z^*K_{wu} + x^*\dot{\phi}\left(K_{ww} + 2\omega^y\right); & K^{w\psi} &= 2z^*\dot{\phi}\,\omega^x + x^*K_{wv},
\end{aligned}
\tag{A.15}
$$

$$
\begin{aligned}
K_{\theta\theta} &= \ddot{z}_O - \left(x^* + x_O\right)K_{wu} - \left(y_{mu} + y_O\right)K_{wv} + z_OK_{ww} + z^*\left(\omega^{y2} - \omega^{z2}\right) + 2\left(\dot{x}_O\omega^y - \dot{y}_O\omega^x\right) + 2z^*\dot{\phi}\omega^y;\\
K_{\theta\lambda} &= x^*\ddot{y}_O + 2x^*\left(\dot{x}_O\omega^z - \dot{z}_O\omega^x\right) + x^*\left(x_O\dot{\omega}^z - z_O\dot{\omega}^x\right) + \left(x^{*2} - z^{*2}\right)\left(\dot{\omega}^z - 2\dot{\phi}\omega^x\right)\\
&\quad - 2x^*z^*\left(\dot{\omega}^x - 2\dot{\phi}\omega^z\right) - x^*\left(y_{mu} + y_O\right)\left(\omega^{x2} + \omega^{z2}\right) + \left(x^*\left(x^* + x_O\right) - z^{*2}\right)\omega^x\omega^y\\
&\quad + x^*\left(2z^* + z_O\right)\omega^y\omega^z;\\
K_{\lambda\theta} &= x^*\ddot{y}_O + 2x^*\left(\dot{x}_O\omega^z - \dot{z}_O\omega^x\right) + x^*\left(x_O\dot{\omega}^z - z_O\dot{\omega}^x\right) - r_{mu}^2\dot{\omega}^z - x^*\left(y_{mu} + y_O\right)\left(\omega^{x2} + \omega^{z2}\right)\\
&\quad + \left(x^*\left(x^* + x_O\right) - z^{*2}\right)\omega^x\omega^y + x^*\left(2z^* + z_O\right)\omega^y\omega^z;\\
K_{\lambda\lambda} &= -\left(x^*\ddot{x}_O + z^*\ddot{z}_O\right) + 2\left(z^*\dot{x}_O - x^*\dot{z}_O\right)\omega^y + 2\dot{y}_O\left(x^*\omega^z - z^*\omega^x\right) + \left(y_{mu} + y_O\right)\left(x^*\dot{\omega}^z - z^*\dot{\omega}^x\right)\\
&\quad + \left(z^*x_O - x^*z_O\right)\dot{\omega}^y + x^*x_O\omega^{z2} + z^*z_O\omega^{x2} - \left(y_{mu} + y_O\right)\left(x^*\omega^x + z^*\omega^z\right)\omega^y + \left(x^*x_O + z^*z_O\right)\omega^{y2}\\
&\quad - \left(z^*x_O + x^*\left(z_O + 4z^*\right)\right)\omega^x\omega^z + \left(z^{*2} - x^{*2}\right)\left(\omega^x - \omega^z\right);\\
K_{\lambda\psi} &= z^*\ddot{y}_O + 2z^*\left(\dot{x}_O\omega^z - \dot{z}_O\omega^x\right) + z^*\left(x_O\dot{\omega}^z - z_O\dot{\omega}^x\right) - r_{mu}^2\dot{\omega}^x - z^*\left(y_{mu} + y_O\right)\left(\omega^{x2} + \omega^{z2}\right)\\
&\quad + \left(z^*\left(z^* + z_O\right) - x^{*2}\right)\omega^y\omega^z + z^*\left(2x^* + x_O\right)\omega^x\omega^y;\\
K_{\psi\lambda} &= z^*\ddot{y}_O + 2z^*\left(\dot{x}_O\omega^z - \dot{z}_O\omega^x\right) + z^*\left(x_O\dot{\omega}^z - z_O\dot{\omega}^x\right) + \left(x^{*2} - z^{*2}\right)\left(\dot{\omega}^x - 2\dot{\phi}\omega^z\right)\\
&\quad + 2x^*z^*\left(\dot{\omega}^z + 2\dot{\phi}\omega^x\right) - z^*\left(y_{mu} + y_O\right)\left(\omega^{x2} + \omega^{z2}\right) + \left(z^*\left(z^* + z_O\right) - x^{*2}\right)\omega^y\omega^z\\
&\quad + z^*\left(2x^* + x_O\right)\omega^x\omega^y;\\
K_{\psi\psi} &= \ddot{x}_O + \left(z^* + z_O\right)K_{uw} + \left(y_{mu} + y_O\right)K_{uv} - x_OK_{uu} + x^*\left(\omega^{x2} - \omega^{y2}\right) + 2\left(\dot{z}_O\omega^y - \dot{y}_O\omega^z\right) - 2x^*\dot{\phi}\omega^y,
\end{aligned}
\tag{A.16}
$$

$$
\begin{aligned}
\mathbf{V}_{emu}^{\ddot{\phi}} &= -m_{mu}\left\{z^* \quad 0 \quad -x^* \quad 0 \quad r_{mu}^2 \quad 0\right\}^T;\\
\mathbf{V}_{emu}^{\dot{\phi}^2} &= m_{mu}\left\{x^* \quad 0 \quad z^* \quad 0 \quad 0 \quad 0\right\}^T;\\
\mathbf{F}_{emu,su}\left(t\right) &= -m_{mu}\left\{F^u \quad F^v \quad F^w \quad F^\theta \quad F^\lambda \quad F^\psi\right\}^T,
\end{aligned}
\tag{A.17}
$$

with

$$
\begin{aligned}
F^u &= \ddot{x}_O + 2\left(\dot{z}_O\omega^y - \dot{y}_O\omega^z\right) - \left(x^* + x_O\right)\left(\omega^{y2} + \omega^{z2}\right) - \left(y_{mu} + y_O\right)\left(\dot{\omega}^z - \omega^x\omega^y\right)\\
&\quad + \left(z^* + z_O\right)\left(\dot{\omega}^y + \omega^x\omega^z\right) - 2x^*\dot{\phi}\omega^y;\\
F^v &= \ddot{y}_O + 2\left(\dot{x}_O\omega^z - \dot{z}_O\omega^x\right) + \left(x^* + x_O\right)\left(\dot{\omega}^z + \omega^x\omega^y\right) - \left(y_{mu} + y_O\right)\left(\omega^{x2} + \omega^{z2}\right)\\
&\quad - \left(z^* + z_O\right)\left(\dot{\omega}^x - \omega^y\omega^z\right) + 2\dot{\phi}\left(x^*\omega^x + z^*\omega^z\right);\\
F^w &= \ddot{z}_O + 2\left(\dot{y}_O\omega^x - \dot{x}_O\omega^y\right) - \left(x^* + x_O\right)\left(\dot{\omega}^y - \omega^x\omega^z\right) + \left(y_{mu} + y_O\right)\left(\dot{\omega}^x + \omega^y\omega^z\right)\\
&\quad - \left(z^* + z_O\right)\left(\omega^{x2} + \omega^{y2}\right) - 2z^*\dot{\phi}\omega^y;\\
F^\theta &= -z^*F^v;\\
F^\lambda &= z^*\ddot{x}_O - x^*\ddot{z}_O + 2\left(\left(x^*\dot{x}_O + z^*\dot{z}_O\right)\omega^y - \dot{y}_O\left(x^*\omega^x + z^*\omega^z\right)\right) + \omega^{y2}\left(x^*z_O - z^*x_O\right)\\
&\quad + \left(x^* + x_O\right)\left(x^*\left(\dot{\omega}^y - \omega^x\omega^z\right) - z^*\omega^{z2}\right) + \left(z^* + z_O\right)\left(z^*\left(\dot{\omega}^y + \omega^x\omega^z\right) + x^*\omega^{x2}\right)\\
&\quad - \left(y_{mu} + y_O\right)\left(x^*\left(\dot{\omega}^x + \omega^y\omega^z\right) + z^*\left(\dot{\omega}^z - \omega^x\omega^y\right)\right);\\
F^\psi &= x^*F^v.
\end{aligned}
\tag{A.18}
$$

References

[1] Y. Kang, T.-W. Lin, Y.-J. Chang, Y.-P. Chang, C.-C. Wang, Optimal balancing of flexible rotors by minimizing the condition number of influence coefficients, Mechanism and Machine Theory 43 (7) (2008) 891–908.

[2] N. Levecque, J. Mahfoud, D. Violette, G. Ferraris, R. Dufour, Vibration reduction of a single cylinder reciprocating compressor based on multi-stage balancing, Mechanism and Machine Theory 46 (1) (2011) 1–9.

[3] M. Lalanne, G. Ferraris, Rotordynamics Prediction in Engineering, Wiley, Chichester, 1998.

[4] G. Genta, Dynamics of Rotating Systems, Springer, New York, 2005.

[5] H. D. Nelson, J. M. McVaugh, The dynamics of rotor-bearing systems using finite elements, ASME Journal of Engineering for Industry 98 (2) (1976) 593–600.

[6] R. Dufour, A. Berlioz, Parametric instability of a beam due to axial excitations and to boundary conditions, ASME Journal of Vibration and Acoustics 120 (2) (1998) 461–467.

[7] P. P. Friedmann, Numerical methods for the treatment of periodic systems with applications to structural dynamics and helicopter rotor dynamics, Computers & Structures 35 (4) (1990) 329–347.

[8] C. S. Hsu, On the parametric excitation of a dynamic system having multiple degrees of freedom, ASME Journal of Applied Mechanics 30 (3) (1963) 367–372.

[9] F. Lin, G. Meng, Study on the dynamics of a rotor in a maneuvering aircraft, ASME Journal of Vibration and Acoustics 125 (3) (2003) 324–327.

[10] A. S. Lee, B. O. Kim, Y.-C. Kim, A finite element transient response analysis method of a rotor-bearing system to base shock excitations using the state-space newmark scheme and comparisons with experiments, Journal of Sound and Vibration 297 (3-5) (2006) 595–615.

[11] M. Duchemin, A. Berlioz, G. Ferraris, Dynamic behavior and stability of a rotor under base excitation, ASME Journal of Vibration and Acoustics 128 (5) (2006) 576–585.

[12] N. Driot, C. H. Lamarque, A. Berlioz, Theoretical and experimental analysis of a base-excited rotor, ASME Journal of Computational and Nonlinear Dynamics 1 (3) (2006) 257–263.

[13] F. M. A. El-Saeidy, F. Sticher, Dynamics of a rigid rotor linear/nonlinear bearings system subject to rotating unbalance and base excitations, Journal of Vibration and Control 16 (3) (2010) 403–438.

[14] A. S. Das, J. K. Dutt, K. Ray, Active vibration control of flexible rotors on maneuvering vehicles, American Institute of Aeronautics and Astronautics Journal 48 (2) (2010) 340–353.

[15] A. S. Das, J. K. Dutt, K. Ray, Active vibration control of unbalanced flexible rotor-shaft systems parametrically excited due to base motion, Applied Mathematical Modelling 34 (9) (2010) 2353–2369.

[16] M. Dakel, S. Baguet, R. Dufour, Steady-state dynamic behavior of an on-board rotor under combined base motions, Journal of Vibration and Control 20 (15) (2014) 2254–2287.

[17] M. Dakel, S. Baguet, R. Dufour, Nonlinear dynamics of a support-excited flexible rotor with hydrodynamic journal bearings, Journal of Sound and Vibration 333 (10) (2014) 2774–2799.

[18] Q. Han, F. Chu, Dynamic response of cracked rotor-bearing system under time-dependent base movements, Journal of Sound and Vibration 332 (25) (2013) 6847–6870.

[19] Q. Han, F. Chu, Dynamic behaviors of a geared rotor system under time-periodic base angular motions, Mechanism and Machine Theory 78 (2014) 1–14.

[20] Q. Han, F. Chu, Parametric instability of flexible rotor-bearing system under time-periodic base angular motions, Applied Mathematical Modelling 39 (15) (2015) 4511–4522.

[21] M. S. Sousa Jr, V. T. S. Del Claro, A. A. Cavalini Jr, V. Steffen Jr, Numerical investigation on the dynamic behavior of an onboard rotor system by using the FEM approach, Journal of the Brazilian Society of Mechanical Sciences and Engineering 39 (7) (2017) 2447–2458.

[22] M. S. Sousa Jr, V. T. S. Del Claro, A. A. Cavalini Jr, V. Steffen Jr, Experimental validation of an onboard rotor FE model, in: Proceedings of the 24th ABCM International Congress of Mechanical Engineering, Curitiba, Paraná, Brazil, 3-8 December 2017.

[23] R. Wang, X. Guo, Y. Wang, Nonlinear analysis of rotor system supported by oil lubricated bearings subjected to base movements, Proceedings of the Institution of Mechanical Engineers, Part C: Journal of Mechanical Engineering Science 230 (4) (2016) 543–558.

[24] M. R. Reddy, J. Srinivas, Vibration analysis of a support excited rotor system with hydrodynamic journal bearings, Procedia Engineering 144 (2016) 825 – 832.

[25] P. M. Przybylowicz, Z. Starczewski, P. Korczak-Komorowski, Sensitivity of regions of irregular and chaotic vibrations of an asymmetric rotor supported on journal bearings to structural parameters, Acta Mechanica 227 (11) (2016) 3101–3112.

[26] Z. Liu, Z. Liu, Y. Li, G. Zhang, Dynamics response of an on-board rotor supported on modified oil-film force considering base motion, Proceedings of the Institution of Mechanical Engineers, Part C: Journal of Mechanical Engineering Science 232 (2) (2018) 245–259.

[27] L. Chen, J. Wang, Q. Han, F. Chu, Nonlinear dynamic modeling of a simple flexible rotor system subjected to time-variable base motions, Journal of Sound and Vibration 404 (2017) 58–83.

[28] H. Phadatare, B. Choudhary, B. Pratiher, Evaluation of nonlinear responses and bifurcation of a rotor-bearing system mounted on moving platform, Nonlinear Dynamics 90 (1) (2017) 493–511.

[29] J. Latalski, J. Warminski, Dynamics of rotating thin-walled cantilever composite beam excited by translational motion, Procedia Engineering 144 (2016) 1039–1046.

[30] R. Bouziani, N. Ouelaa, Simulation of the dynamic behavior of a rotor subject to base motion under variable rotational speed, Mechanics & Industry 18 (3) (2017) 308–1–308–15.

[31] Y. Yi, Z. Qiu, Q. Han, The effect of time-periodic base angular motions upon dynamic response of asymmetric rotor systems, Advances in Mechanical Engineering 10 (3) (2018) 1–12.

[32] T. Soni, J. K. Dutt, A. S. Das, Parametric stability analysis of active magnetic bearing-supported rotor system with a novel control law subject to periodic base motion, IEEE Transactions on Industrial Electronics (2019) http://dx.doi.org/10.1109/TIE.2019.2898604. (in press).

[33] J. Frêne, D. Nicolas, B. Degueurce, D. Berthe, M. Godet, Hydrodynamic Lubrication Bearings and Thrust Bearings, Elsevier Science, Amsterdam, 1997.

[34] L.-W. Chen, D.-M. Ku, Dynamic stability of a cantilever shaft-disk system, ASME Journal of Vibration and Acoustics 114 (3) (1992) 326–329.

[35] J. W. Thomas, Numerical Partial Differential Equations, Springer, New York, 1999.

[36] P. Flores, J. C. Pimenta Claro, J. Ambrósio, Journal bearings subjected to dynamic loads: the analytical mobility method, in: Proceedings of the III Congresso Ibérico de Tribologia, Guimarães, Portugal, 16-17 June 2005.

[37] P. P. Friedmann, C. E. Hammond, T.-H. Woo, Efficient numerical treatment of periodic systems with application to stability problems, International Journal for Numerical Methods in Engineering 11 (7) (1977) 1117–1136.

[38] A. Berlioz, R. Dufour, S. C. Sinha, Bifurcation in a nonlinear autoparametric system using experimental and numerical investigations, Nonlinear Dynamics 23 (2) (2000) 175–187.

[39] L. Peletan, S. Baguet, M. Torkhani, G. Jacquet-Richardet, A comparison of stability computational methods for periodic solution of nonlinear problems with application to rotordynamics, Nonlinear Dynamics 72 (3) (2013) 671–682.

[40] J. R. Hutchinson, Shear coefficients for Timoshenko beam theory, ASME Journal of Applied Mechanics 68 (1) (2001) 87–92.

[41] Y. Briend, M. Dakel, E. Chatelet, M.-A. Andrianoely, R. Dufour, S. Baudin, Extended modal reduction for on-board rotor with multifrequency parametric excitation, ASME Journal of Vibration and Acoustics 141 (6) (2019) 061009–1–061009–12.